PUB 93 - 120 T

A SEARCH FOR SUPERSYMMETRY USING ACOPLANAR CHARGED PAIRS AT ALEPH

by

JOSEPH F. BOUDREAU

A thesis submitted in partial fulfillment of the requirements for the degree of

Doctor of Philosophy

(Physics)

at the

UNIVERSITY OF WISCONSIN-MADISON

1990

A SEARCH FOR SUPERSYMMETRY USING ACOPLANAR CHARGED PAIRS AT ALEPH

Joseph F. Boudreau

Under the supervision of Professor Sau Lan Wu
at the University of Wisconsin-Madison

ABSTRACT

Using the ALEPH detector, we have looked for charged, supersymmetric, non-strongly interacting particles, in particular, the selectron, smuon, stau, and chargino. Such particles would be pair produced in e^+e^- collisions primarily through the exchange of the Z^0 boson in the s-channel. The decay products of the supersymmetric final states would contain pairs of acoplanar charged particles, with missing energy carried off by weakly interacting massive photinos. In a 2.45 pb^{-1} sample of data collected near the Z^0 peak in ALEPH during 1989-1990, we observe only 8 events when 11.7 are expected from Standard Model backgrounds alone. Standard techniques allow us to interpret this as a 95% confidence level limit on the masses of selectron, smuon, stau, and chargino. These limits extend to nearly half of the mass of the Z^0.

Acknowledgements

It is with great pleasure that I acknowledge the people whose help has permitted me to complete the present research.

I wish to thank my parents, whose support I have enjoyed for many years. They have given me lots of encouragement along the way to this degree. In addition I would like to thank my brothers and sisters: Vinny, Maura, Kristin, Suzy, Gord, and Lou, who have each been a constant source of humour and joy.

My advisor, Sau Lan Wu, has provided me a great opportunity to do research on ALEPH, and has given me valuable guidance towards using it in the most constructive way. The atmosphere she has created at CERN is very stimulating, not only because of the very diverse, hard-working and knowledgeable group she has built, but also because her own accessibility as an advisor is truly remarkable.

Both Jack Steinberger and Jaques Lefrancois have been fine leaders of the ALEPH collaboration; I am indebted to them for the exceptional atmosphere that prevails within the collaboration. Jean-Francois Grivaz has taught me a lot about the theoretical and experimental aspects of supersymmetry. I thank the people of the TPC group, especially Giorgio Stefanini, Jurgen May, Jenny Thomas, Joerg Richstein, and Dick Jared for teaching me what I know about hardware and electronics.

Many post-docs in the Wisconsin group at CERN have taught me a lot, too. It has been a pleasure to work with John Conway on the our SUSY investigations both before the LEP turn-on and after. Haimo Zobernig, with whom I have shared an office since arriving at CERN, has been generous with his time whenever I needed enlightenment on any of a hundred topics. I thank Bruce LeClaire for our late-night discussions on everything from physics to computers, and all the other post-docs who have taken a role in my education here: Robert Johnson, Mike Mermikedes, David Strom, John Harton and Vivek Sharma. In addition, I would like to thank the students of the Wisconsin group not only because I have learned from them too, but also because they have made my stay at CERN very fun and pleasurable.

I thank Patricia Van Gene and Olga Mermikedes for the enormous amount they have done to make sure the Wisconsin group keeps going, and also for their friendliness, which has kept the morale of the group very high.

I am indebted to Steve Ritz, Makoto Takashima, Howard Stone, David Stickland and Patricia McBride for valuable conversations over the past few years.

I wish to thank those in the Department of Energy who have supported the Wisconsin group at CERN.

Finally, I wish to thank Pask, whose promise of dinner chez Giardet together and an engraved Swiss army knife has been a powerful motivation to finish this work.

Contents

Chapter 1

Supersymmetric Extensions to the Standard Model

A theory known as the Standard Model[1,2,3], based on the principal of local gauge invariance under the group $\mathbf{SU(3)} \times \mathbf{SU(2)} \times \mathbf{U(1)}$ and on the spontaneous breakdown of this invariance via the Higgs mechanism, is able to explain a remarkable of variety of observed phenomenon. It integrates in a single framework the observed spectrum of hadrons, the observed spectrum of charged and neutral leptons, and the strong, electromagnetic and weak interactions of all of these particles. It has survived a recent set of precision tests at the Stanford Linear Collider(SLAC)[4,5,6,7] and at the Large Electron Positron collider (LEP)[8,9,10,11], [12,13,14,15] [16,17,18,19] [20,21], and to date no experimental phenomena has been observed which is inconsistent with the Standard Model. The top quark and the Higgs boson, required to exist by the Standard Model, have not yet been observed but neither have they been ruled out at all masses[22,23,24,25,26,27],[28,29,30].

This thesis describes a search for particles from supersymmetry, which is a theory beyond the Standard Model. In the first chapter, we will discuss the key ingredients of the Standard Model, and the some its features that have lead theorists to search for physical models beyond the Standard Model, supersymmetry in particular. Then we will briefly describe supersymmetric theories before describing in detail the particles for which we search and their experimental signatures.

1.1 Fermions in the Standard Model

The known fermions can be organized into charged leptons, their partner neutrinos, up-like quarks with charge 2/3 and down-like quarks with charge -1/3. Left- and right- handed helicities exist for all states except for the massless neutrinos, which have only left-handed helicity states. The Standard Model accounts for this spectrum in the following way. Each particle must lie in some representation of the gauge group. The left handed leptons lie in the 1/2 representation of $\mathbf{SU(2)}$ which is to say they form a weak isospin doublet:

$$\begin{pmatrix} \nu_L \\ e_L \end{pmatrix}.$$

At the same time they lie in the trivial representation of $\mathbf{SU(3)}$, i.e., they are color neutral. The right handed charged leptons like e_R are weak isopsin singlets as well as color singlets, and right-handed neutrinos are assumed not to exist. The left-handed quarks are also doublets under $\mathbf{SU(2)}$, e. g.,

$$\begin{pmatrix} u_L \\ d_L \end{pmatrix}$$

while u_R and d_R are singlets. However the quarks transform under the fundamental representation of $\mathbf{SU(3)}$, so each quark comes in three "colors": red, green, and blue. The color degree of freedom plus the caveat that only color singlet states can exist (current theoretical investigation may show that this property, confinement, follows from QCD itself[31]) allows one to construct all the known hadrons. For example the Δ^{++} needs the color degree of freedom to antisymmetrize the wave functions of the three up quarks. The evidence for three colors of quark comes from many places. The rise in R above the charm threshhold and the τ leptonic branching ratios are explained if there are three colors [32].

Quarks and leptons also have a conserved quantum number Y from the $\mathbf{U(1)}$ symmetry called weak hypercharge, which determines the charge of the state through the relation

$$Q = I_3 + \frac{1}{2}Y.$$

The values of the hypercharge are not predicted at all by the Standard Model but must be put in by hand in order to get the electric charges to come out correctly.

The quarks and leptons may be organized into generations, where the quantum numbers of the leptons and quarks are identical from one generation to the next, with only the mass differing. The evidence from LEP and SLC strongly suggests that the number of these generations is three; these are:

$$\begin{pmatrix} \nu_e \\ e \\ u \\ d \end{pmatrix}, \begin{pmatrix} \nu_\mu \\ \mu \\ c \\ s \end{pmatrix}, \begin{pmatrix} \nu_\tau \\ \tau \\ t \\ b \end{pmatrix}.$$

Table 1.1 summarizes the quantum numbers of the fermionic sector of the standard model. We have only to add that the left- and right- handed states

State	T	T_3	Y	Q
ν_L	1/2	1/2	-1	0
e_L	1/2	-1/2	-1	-1
e_R	0	0	-2	-1
u_L	1/2	1/2	1/3	2/3
d_L	1/2	-1/2	1/3	-1/3
u_R	0	0	4/3	2/3
d_R	0	0	-2/3	-1/3

Table 1.1: Quantum numbers of the fundamental fermions.

do *not* have the same quantum numbers and this difference, though no more deeply understood than the assignment of quantum numbers is generally, lies at the origin of parity violation in the weak interactions.

1.2 Gauge Bosons, Spontaneous Symmetry Breaking, and the Higgs Boson

The principal of local gauge invariance requires that a spin-1 boson appear for every degree of freedom in the gauge group. Thus we get one spin-1 field B from the single-parameter group $\mathbf{U(1)}$, three spin-1 fields $\{W^+, W^-, W^0\}$ from the three-parameter group $\mathbf{SU(2)}$, and eight spin-1 gluons from the eight-parameter group $\mathbf{SU(3)}$. Moreover the interactions between these gauge field and their coupling to matter are fixed, up to dimensionless coupling constants whose value can only be determined by experiment[33,34].

The characteristics of the strong interactions are largely determined by the non-abelian nature of $\mathbf{SU(3)}$ [35,36] and the masslessness of the gluons. The latter can not only have interactions with the fermion fields as in abelian gauge theories, but also may interact with each other, as in figure 1.1. This leads to

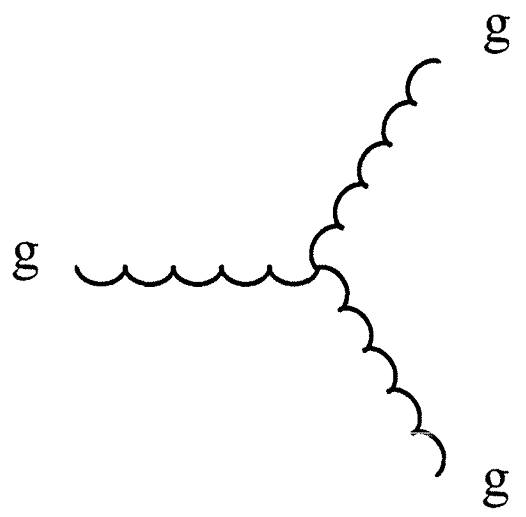

Figure 1.1: The three-gluon vertex, due to the non-abelian character of QCD.

a kind of reverse-charge screening that causes the quarks effective color charge, a running coupling, to increase with distance (rather than decrease as in the electromagnetic interactions, for example); it is possible that this leads to quark confinement. The running coupling may also explain the form of the $q\bar{q}$ potential in heavy quark systems such as the B meson, and spin-dependent mass splittings in hadrons[32]. However at higher energies and shorter distances the quarks behave essentially as if they were free and perturbative calculations may be done in this regime, a phenomenon known as asymptotic freedom[37]. The phenomenon of gluon radiation in e^+e^- collisions, first seen at PETRA[38], is an example of a perturbative QCD process.

From now on we will concentrate on the electroweak sector of the theory, which is complicated by the presence of the Higgs field, a complex scalar isospin doublet

$$\Phi = \begin{pmatrix} \phi^+ \\ \phi^0 \end{pmatrix}$$

with hypercharge $Y = 1$ and a self-coupling of $\mu^2|\Phi|^2 + \lambda|\Phi|^4$ where $\mu^2 < 0$.

The gauge-invariant Lagrangian of the theory, including the gauge fields, the Higgs fields, and the first-generation leptons, is

$$\begin{aligned}
\mathcal{L} &= -\frac{1}{4}\mathbf{W}^{\mu\nu}\cdot\mathbf{W}_{\mu\nu} - \frac{1}{4}B^{\mu\nu}\cdot B^{\mu\nu} \\
&+ \bar{e}_R i\gamma^\mu\left(\partial_\mu + \frac{ig\prime}{2}B_\mu\right)e_R \\
&+ (\bar{\nu}_L, \bar{e}_L)\, i\gamma^\mu\left(\partial_\mu + \frac{ig\prime}{2}B_\mu Y + \frac{ig}{2}\tau\cdot\mathbf{W}_\mu\right)\begin{pmatrix} \nu_L \\ e_L \end{pmatrix} \\
&+ \left\{\left(\partial_\mu + \frac{ig\prime}{2}B_\mu Y + \frac{ig}{2}\tau\cdot\mathbf{W}_\mu\right)\Phi\right\}^\dagger\left\{\left(\partial_\mu + \frac{ig\prime}{2}B_\mu Y + \frac{ig}{2}\tau\cdot\mathbf{W}_\mu\right)\Phi\right\} \\
&- \left(\mu^2|\Phi|^2 + \lambda|\Phi|^4\right)
\end{aligned}$$

Now the Higgs potential $\mu^2|\Phi|^2 + \lambda|\Phi|^4$ has a minimum at a nonzero value of the Higgs field which can be expressed, after a suitable choice of gauge, as

$$\Phi = \begin{pmatrix} 0 \\ \frac{v}{\sqrt{2}} \end{pmatrix},$$

where $v = \sqrt{-\mu^2/\lambda}$. The Lagrangian may be written in terms of small excursions from the vacuum state. We can choose the gauge in order that the Higgs field can be written as

$$\Phi = \begin{pmatrix} 0 \\ \frac{v+\eta}{\sqrt{2}} \end{pmatrix}$$

Then the scalar part of the Lagrangian contains the terms:

$$\mathcal{L}_{scalar} = \frac{1}{2}\partial^\mu\eta\partial_\mu\eta - \mu^2\eta^2 - \frac{v^2}{8}\left\{g^2\left|W^1_\mu - iW^2_\mu\right|^2 + \left(g\prime B_\mu - gW^3_\mu\right)^2\right\} \quad (1.1)$$

The quadratic form in the gauge fields can be diagonalized to yield exact mass eigenvalues and eigenstates; the result is that the W^+ and W^- fields remain unmixed but acquire a mass of $gv/2$, and the W^0 and B fields mix to form one eigenstate, $A_\mu = (gB_\mu + g\prime W^3_\mu)/(g^2 + g\prime^2)$, with zero mass, and an orthogonal linear combination $Z_\mu = (-g\prime B_\mu + gW^3_\mu)/(g^2 + g\prime^2)$ with mass of $(g^2 + g\prime^2)v/2$.

The heavy vector bosons, $W^\pm$ and Z^0, are the force carriers of the weak interaction and all of the weak interaction phenomena derive from their interaction with matter. Just a few examples of such phenomena are: nuclear beta decay, muon decay, charged current neutrino-quark scattering, neutral current neutrino-quark scattering, and electroweak interference. Both the W and Z bosons were discovered at CERN in 1983.

Of the four degrees of freedom in the Higgs field, three seem to have disappeared through the proper choice of gauge (actually they have turned into additional transverse degrees of freedom for massive vector bosons), and the fourth is that of a scalar particle, the Higgs, whose mass according to equation 1.1 is given by $M_H^2 = -2\mu^2 > 0$ and is unrelated to other measured quantities in the theory. Its long-awaited discovery would put the Standard Model on even stronger footing.

The Higgs boson gives mass to the leptons by coupling to them through the renormalizable gauge-invariant terms such as

$$G_e \left\{ \bar{e}_R \Phi^\dagger \cdot \begin{pmatrix} \nu_L \\ e_L \end{pmatrix} + (\bar{\nu}_L, \bar{e}_L) \cdot \Phi e_R \right\}$$

When the Higgs field acquires a vacuum expectation value the fermion fields acquire a mass, $G_e v/\sqrt{2}$. The masslessness of the neutrinos is then explained naturally by the absence of right-handed neutrino fields from which to construct the above terms. For the quarks the same mechanism induces terms bilinear in the quark fields:

$$-\tilde{G}\left\{\left(\bar{L}_j\bar{\Phi}\right)u_{iR}+\bar{u}_{iR}\left(\bar{\Phi}^{\dagger}L_j\right)\right\}+-G\left\{\left(\bar{L}_j\Phi\right)d_{iR}+\bar{d}_{iR}\left(\Phi^{\dagger}L_j\right)\right\}$$

with $i=1,3$ and

$$L=\begin{pmatrix} u_{iL} \\ d_{iL} \end{pmatrix}$$

The matrix of bilinear terms when diagonalized gives both the quark mixings (the Kobayashi-Maskawa matrix) and the quark masses. This is how the standard model explains mixing phenomena such as kaon mixing, $B\bar{B}$ mixing, and CP violation.

This brief summary of the standard model makes clear both the attractive features of the model, and some of the undesirable ones. It is a relatively simple framework for unifying a both weak, strong, and electromagnetic interactions. However it abounds in parameters which must be provided as input, including the masses of six quarks and three leptons, four independent Kobayashi-Maskawa matrix elements, the Weinberg angle, and two gauge coupling constants. The reason for three "standard" generations is not understood. Neither are the quantum numbers assigned to the known quarks and leptons, especially the hypercharge, in connection with which it must be mentioned that this assignment causes the triangle anomalies to cancel. It is not known whether the neutrinos have right-handed states; or if they do, then why their masses are so small.

A widely-held belief is that the Standard Model is the low-energy limit of a more fundamental theory based on a larger symmetry group than $\mathbf{SU(3)} \times \mathbf{SU(2)} \times \mathbf{U(1)}$ [39]. The symmetry of this larger group is hidden at low energies because it has been broken in some way, usually by a spontaneous symmetry breaking similar to the Higgs mechanism. Such grand unified theories (GUTS) have an energy scale associated with them, which are typically of the order of 10^{15} GeV (the "unification energy") or 10^{19} GeV (the Plank mass, where quantum effects become important in gravitation).

But the Standard Model has problems when integrated into such a theory. The first problem, called the naturalness problem, may be summed up as follows: a Higgs from a Grand Unified Theory has a mass which is a running constant of the theory. To obtain the mass at LEP, CLIC, or SSC energies, we must renormalize the GUT and evaluate the running mass at the electroweak scale. A near cancellation between two different terms, each order of 10^{15}GeV, must occur in order to keep the observed Higgs mass at less than 1 TeV[40,41,42,43], which is necessary to keep the standard model perturbative, as it seems to be. A second problem is known as the hierarchy problem. A GUT containing $\mathbf{SU(3)} \times \mathbf{SU(2)} \times \mathbf{U(1)}$ has at least two energy scales. One, μ_2, corresponds roughly to the mass of the Standard Model Higgs, and the other, μ_1, to the unification energy or the mass of one or more heavy Higgses. The Higgs potential, which contains self interactions and interactions between the various scalar fields, requires unnatural tuning of the parameters in order that a minimum in the potential can exist such that $\mu_1 \gg \mu_2$ [44,45,46,47]. Once the tuning has taken place, one must again re-tune at every order of perturbation theory so that radiative corrections do not disturb the hierarchy[44].

One can invent other ways of breaking the electroweak symmetry besides a single Higgs doublet. The Higgs sector may be enlarged to two or more Higgs doublets, giving this time charged as well as neutral Higgs bosons[48]. Another approach is to allow compositeness to generate mass of bosons and fermions.[49]. Yet another is to use a new force, ("technicolor")[50], to hold together composite objects. These latter two approaches are a means of circumventing problems introduced by fundamental scalars such as the Higgs boson.

A class of models shows promise in resolving problems related to the radiative corrections of the Higgs mass, by using a higher symmetry to protect the Higgs mass against radiative corrections such as we have discussed. These models are known as supersymmetric models.

1.3 Models with Supersymmetry

Supersymmetry developed from efforts in the 1960's to incorporate the spacetime symmetries of the Poincare group together with internal symmetries in a larger group[51]. After a series of failures in this direction a no-go theorem of Coleman and Mandula proved that such a unification was impossible when the algebra of the larger symmetry was a Lie algebra, i.e., an algebra whose defining relations consisted of antisymmetric Lie products such as commutators[52]. However it was soon discovered by Haag, Lopuszanski, and Sohnius that if the algebra defining the symmetry was a graded Lie Algebra, possessing both symmetric and antisymmetric products, then unification of spacetime and internal symmetries could occur[53]. Furthermore the representation would contain states of both integer and half-integer spin. By this time a renormalizable toy field theory possessing such a symmetry had already been put forward by Wess and Zumino[54].

A supersymmetry is a also symmetry of the Lagrangian under an operation which carries fermionic states into bosonic states. The standard model is not supersymmetric as it stands, but any theory can be made supersymmetric by the addition of suitable terms in the Lagrangian[51]. In the case of the standard model each new field in the Lagrangian, when quantized, gives a "partner" to the known particle spectrum. A supersymmetric standard model will therefore include:

- spin -$\frac{1}{2}$ partners to the gauge bosons called *photino, zino, and wino*
- spin -0 partners to the leptons called *sleptons*, or *selectron, smuon and stau.* There is a left-handed and a right-handed partner to each normal lepton.

Additionally, there are spin-$\frac{1}{2}$ partners to the Higgs bosons. However the higgs sector itself has to be enlarged to two Higgs doublets, of which one gives mass to all of the up-like quarks, and the other gives mass to the down-like quarks[55,56]. The particle spectrum is now enlarged to two charged Higgs bosons and three neutral Higgs bosons. The supersymmetric partners to these are two charged higgsinos, and two neutral higgsinos.

The couplings of each of the above mentioned states is fixed by $\mathbf{SU(3)} \times \mathbf{SU(2)} \times \mathbf{U(1)}$ and by the requirement that that the Lagrangian be invariant

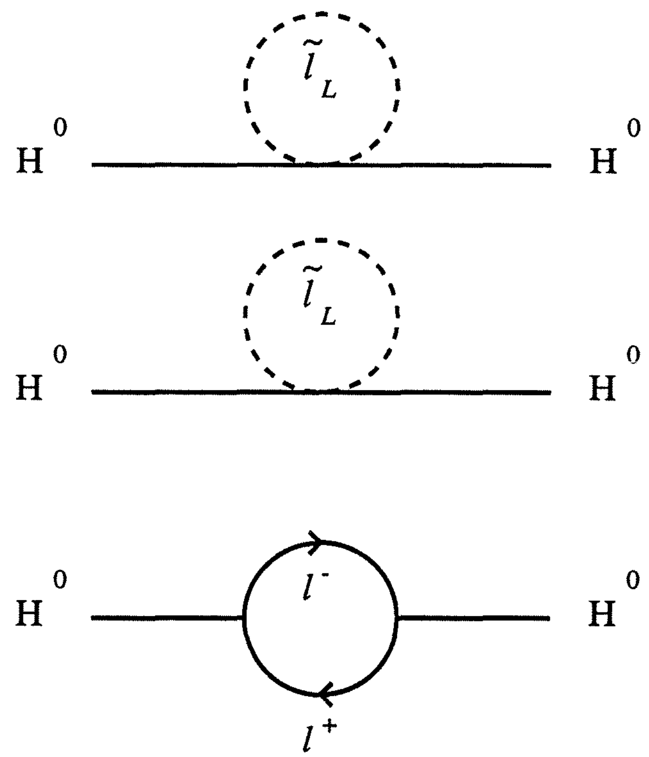

Figure 1.2: Cancelling correction terms to Higgs mass.

to supersymmetry transformations. If the supersymmetry were unbroken then we would have equal masses between all particles and their superpartners and no mixing between superpartner states. In such a case the quadratically divergent corrections to scalar masses cancel between pairs of terms such as shown in figure 1.2, and the light higgs stays light without any fine-tuning[54]. In supersymmetry, this cancellation occurs to all orders in perturbation theory[57]. In case the supersymmetry is only approximate, the two terms in figure 1.2 cancel only partially, giving a residual contribution of $\tilde{M}^2 - M^2$, where $\tilde{M}$ is the mass of the supersymmetric partner and M is the mass of the standard particle[58]. It may be that the masses of the Higgs particles, which are expected to lie somewhere in the range of 250 GeV, comes entirely from terms of this kind, i.e., that supersymmetry is responsible for setting the electroweak scale. In that case one predicts masses for these particles on the same scale[40].

Supersymmetry thus solves the "naturalness" problem described above. It is also possible that SUSY may solve the hierarchy problem as well[59,60]. Several other advantages recommend a supersymmetric theory over a non-supersymmetric one. Supersymmetry is the only way to integrate gravity (transmitted by a spin-2 intermediate boson) with $\mathbf{SU(3)} \times \mathbf{SU(2)} \times \mathbf{U(1)}$, since the the force carriers lie in different representations of the Poincare group and so can only be linked by a supersymmetry. When supersymmetry is local, local space-time transformations (gravity) emerge naturally[61]. It would explain why the known particles occur in certain representations of the Lorentz group (spin-0, spin-$\frac{1}{2}$, spin-1) and are not yet found in others, and it would abolish the distinction between "matter" and "radiation" fields. If, however, these are attractive reasons for believing in supersymmetry, they do nothing to suggest that SUSY should be observable on the electroweak scale.

1.4 Particles and Signatures

As mentioned above the couplings of sparticles amongst themselves and to the known particles are all calculable in an unbroken supersymmetric extension of the standard model. When the theory is spontaneously broken, however, the sparticles acquire mass in an unknown way and the mixing of current eigenstates become unknown as well.

In the sfermion sector there can be a mass matrix in the lagrangian relating the current eigenstates of the charged scalar leptons:

$$(\tilde{l}_L, \tilde{l}_R) \boldsymbol{M}_{LR} \begin{pmatrix} \tilde{l}_L \\ \tilde{l}_R \end{pmatrix}$$

The mass eigenstates are the linear combinations of $\tilde{l}_L, \tilde{l}_R$ which diagonalize this matrix[55,56]. For the sneutrinos only left-handed partners exist.

Similarly, there can be mixing between the charged higgsinos and the winos, and mixing among the photino, zino, and two neutral higgsinos. The resulting states are referred to as "charginos" (denoted by $\tilde{\chi}^{\pm}$) for the charged gauge fermions and "neutralinos" ($\tilde{\chi}^0$, $\tilde{\chi}^{0\prime}$, $\tilde{\chi}^{0\prime\prime}$, and $\tilde{\chi}^{0\prime\prime\prime}$) for the neutral gauge fermions. Again the mixing and the masses of the sparticles is completely unknown unless a specific model describing how the mass matrix terms arises is adopted. The phenomenological description of SUSY is then highly dependent on the mass hierarchy of the sparticles and also somewhat on the mixing angles.

Several phenomenological facts however can be deduced even in the absence of an exact knowledge of what the physical eigenstates actually are or what the masses are. The most important facts are

1. Nearly all models of supersymmetry predict a conserved multiplicative quantum number called R-parity which is +1 for conventional particles and -1 for supersymmetric partners. Supersymmetric particles can only be

produced in pairs, and they can only decay into odd numbers of supersymmetric particles. It follows that the lightest supersymmetric particle is stable[62,63].

2. Charged or strongly-interacting supersymmetric particles would condense into normal matter, and thus would be detected in searches for anomalous heavy isotopes. The negative results of such searches imply that the lightest supersymmetric particles are neutral. They then interact only by exchanging heavy supersymmetric intermediate states with nuclei, which suppresses their cross section with matter [64].

A neutralino is a favored candidate for the lightest supersymmetric particle. Henceforth we will denote the lightest of the neutralino states as the *photino* ($\tilde{\gamma}$). It need not be a pure partner of the photon for the purposes of the search that we will describe herein. Another possibility is the sneutrino (scalar partner of the neutrino), but this is not considered in our search.

In reference [55], reference [56], as well as later treatments of the topics, explicit forms of the mass mixing matrices have been exhibited. They are derived from a variety of assumptions on how the exact supersymmetry of the theory becomes spontaneously broken, and the resulting theory has come to be known as the minimal supersymmetric standard model or MSSM. Within this model, the fermion mass matrix, the chargino mass matrix, and the neutralino mass matrix are expressed in terms of only three parameters usually called M, m, and $\tan(\beta)$. This model allows very detailed predictions of collider phenomenology to be made over a wide range of energies. In addition a number of interesting propositions emerge from it:

- One of the chargino states has a mass lighter than M_W
- There exists a neutral Higgs lighter than the M_Z

It also predicts that a number of particles will be heavier than the gauge bosons.

We will here describe a search for the supersymmetric processes:

$$e^+e^- \rightarrow \tilde{e}^+\tilde{e}^- \rightarrow e^+\tilde{\gamma}e^-\tilde{\gamma}$$

$$e^+e^- \rightarrow \tilde{\mu}^+\tilde{\mu}^- \rightarrow \mu^+\tilde{\gamma}\mu^-\tilde{\gamma}$$

$$e^+e^- \rightarrow \tilde{\tau}^+\tilde{\tau}^- \rightarrow \tau^+\tilde{\gamma}\tau^-\tilde{\gamma}$$

$$e^+e^- \rightarrow \tilde{\chi}^+\tilde{\chi}^- \rightarrow l^+\tilde{\gamma}\nu l^-\tilde{\gamma}\nu$$

at center-of-mass energies near the Z^0 peak. Because the Z^0-decay to supersymmetric particles is the dominant production mechanism, and because the signatures look the same regardless of *which* neutralino is present in the final state, the search we will describe is independent of mixing in the neutralino sector. The parameters which do affect the search are the mass of the charged sparticle, the mass of the photino, and, in the case of the chargino, the chargino mixing angle. We therefore prefer to discuss our limits in the space of these parameters instead of parameters of the MSSM so that we avoid unnecessary dependence on the symmetry breaking mechanism of this model.

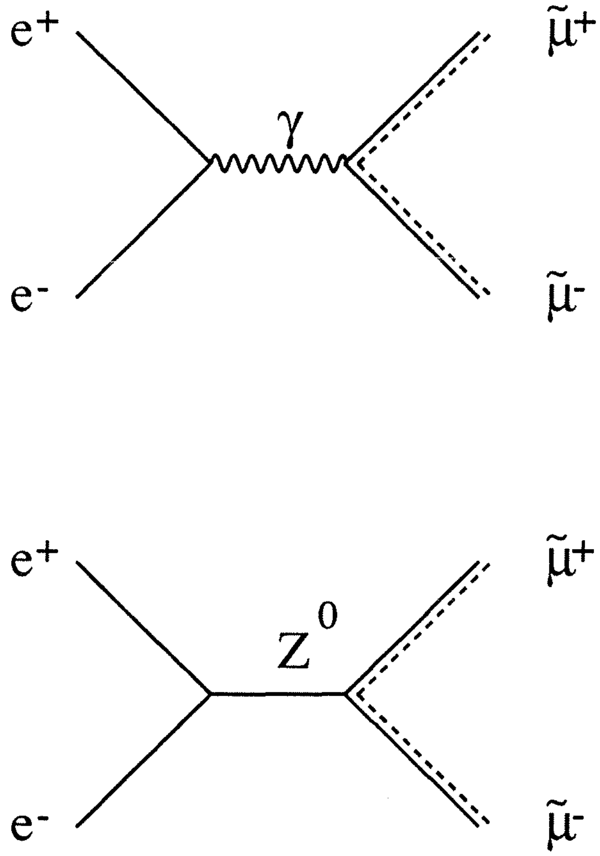

Figure 1.3: Feynman diagrams for smuon production. The cross section is dominated by the Z^0 diagram at the energies we discuss.

1.4.1 Scalar Leptons

The pair production of $\tilde{\mu}$ and $\tilde{\tau}$ takes place through the diagrams of figure 1.3. At the Z^0 peak the upper graph in the figure would be negligible in comparison with the lower. At the Born level the differential cross section from the Z^0 term alone is [65]

$$\begin{aligned}\frac{d\sigma}{d\cos\theta} &= \frac{\beta^3}{256\pi}(1-\cos^2\theta)\cdot \\ &\quad \frac{e^2A^2(C_V^2+C_A^2)s}{(s-m_Z^2)^2+m_Z^2\Gamma_Z^2}\end{aligned}$$

where

$$\begin{aligned}C_V &= \frac{1}{4}(\cot\theta_W - 3\tan\theta_W) \\ C_A &= -\frac{1}{4}(\cot\theta_W + \tan\theta_W)\end{aligned} \tag{1.2}$$

come from the coupling of the initial state to the Z^0 and

$$\begin{aligned}A_L &= -e(\tan\theta_W - \cot\theta_W) \\ A_R &= -2e\tan\theta_W\end{aligned}$$

governs the final states couplings. In this thesis we will consider the cases of

- mass degenerate left and right handed states, any mixing
- only the right-handed state at less than the beam energy, no mixing

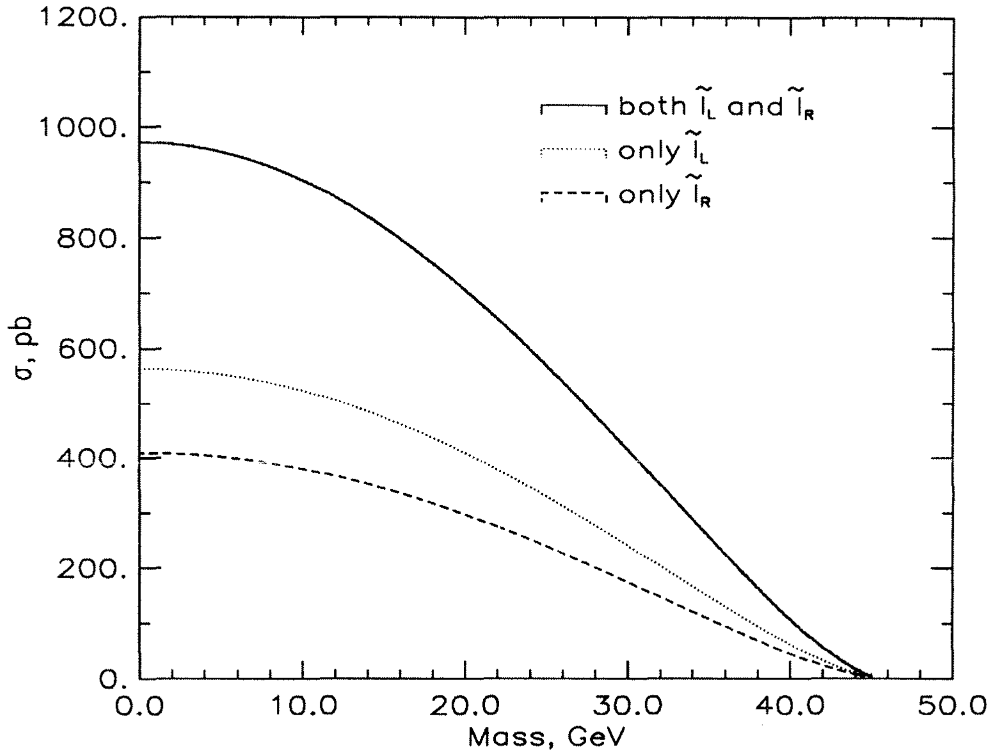

Figure 1.4: Slepton cross section vs. slepton mass, at the Z^0 peak.

The cross section varies as β^3 and an angular distribution as $\sin^2\theta$, both typical for the pair production of scalars through vector intermediates. Figure 1.4 shows the dependence of the total cross section on the slepton mass (Born term Z^0 exchange only). QED radiative corrections reduce the peak cross section to about 2/3 of the Born cross section.

Now we consider scalar electron production. In addition to the terms in figure 1.3, the t-channel terms of figure 1.5 contribute. A great number of unknown parameters such as the masses and mixings of the exchanged sparticles

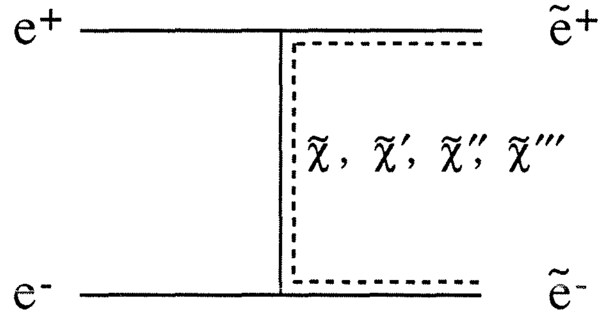

Figure 1.5: Additional t-channel graphs for selectron production.

come into the calculation. However in general these contributions will all be small compared to the dominant one which is still that of 1.2. If one assumes that the neutralino mixing occurs as in the MSSM one can extrapolate the cross-section calculation to center-of-mass energies different from M_Z [65], however the formulae thus obtained are to lengthy to reproduce here, and not of great interest to this search which is carried out on the Z^0 peak.

The decay of the scalar lepton via the channel

$$\tilde{l} \rightarrow \tilde{\gamma} l$$

takes place promptly with 100% branching ratio, through the diagram of figure 1.6. The photino does not interact and it is assumed not to decay. The

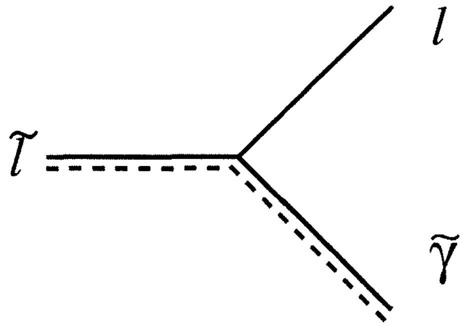

Figure 1.6: Diagram for the decay of scalar leptons into the associated lepton and the photino.

photino need not be pure, but we make the assumption there of no cascade decays from to one neutralino to a lighter one with other visible decay products.

The signature for slepton pair production followed by decay is two charged particle tracks with missing energy and transverse momentum. If the slepton happens to be a stau, then there will be fewer events with the two-track topology but more missing energy due to additional neutrinos which escape the detector.

The production of each signal is simulated using programs SELGEN, and SMUGEN, [66,67], modified to take into account the reduction of the cross section due to initial state radiation in a first-order approximation[68]. The next order correction would increase the cross section so this is pessimistic. We have also incorporated LUND decays of the tau. The program generates according to the MSSM, however from the above discussion it is clear that in the energy range of the data sample, 88 – 94 GeV, the results do not depend on the MSSM but only on the assumptions stated above.

1.4.2 Charginos

The pair production of charginos in e^+e^- collisions occurs through the diagrams of figure 1.7. The mass of the charginos are not known, nor is the mass of the exchanged sneutrino. The gauge content of the chargino in terms of "current eigenstates" of charged Higgsino and wino affect its couplings to both the Z^0 and to the sneutrino. However, as in the discussion of the scalar leptons, the dependence on some of these parameters disappears when the center-of-mass energy is near the Z^0 peak, for there only the Z^0 exchange term contributes significantly. Then the differential cross section (Z^0 annihilation Born term) may be derived from a general expression given in reference [69], and is:

$$\begin{aligned} \frac{d\sigma}{d\cos\theta} &= G_F^2 M_Z^4 \frac{\beta s}{64\pi} \frac{1}{(s-M_Z^2)^2 + M_Z^2\Gamma_Z^2} \cdot \\ & \Big\{(1+\beta\cos\theta)^2(\tilde{g}_L^2 g_L^2 + \tilde{g}_R^2 g_R^2) + \\ & (1-\beta\cos\theta)^2(\tilde{g}_L^2 g_R^2 + \tilde{g}_R^2 g_L^2) + \\ & 2(1-\beta^2)(\tilde{g}_L^2 g_L g_R + \tilde{g}_R^2 g_L g_R)\Big\}. \end{aligned} \tag{1.3}$$

and the total cross section is:

$$\begin{aligned} \sigma &= G_F^2 M_Z^4 \frac{\beta s}{32\pi} \frac{1}{(s-M_Z^2)^2 + M_Z^2\Gamma_Z^2} (\tilde{g}_L^2 + \tilde{g}_L^2) \cdot \\ & \left\{(1+\frac{\beta^2}{3})(g_L^2 + g_R^2) + 2(1-\beta^2) g_L g_R\right\}, \end{aligned} \tag{1.4}$$

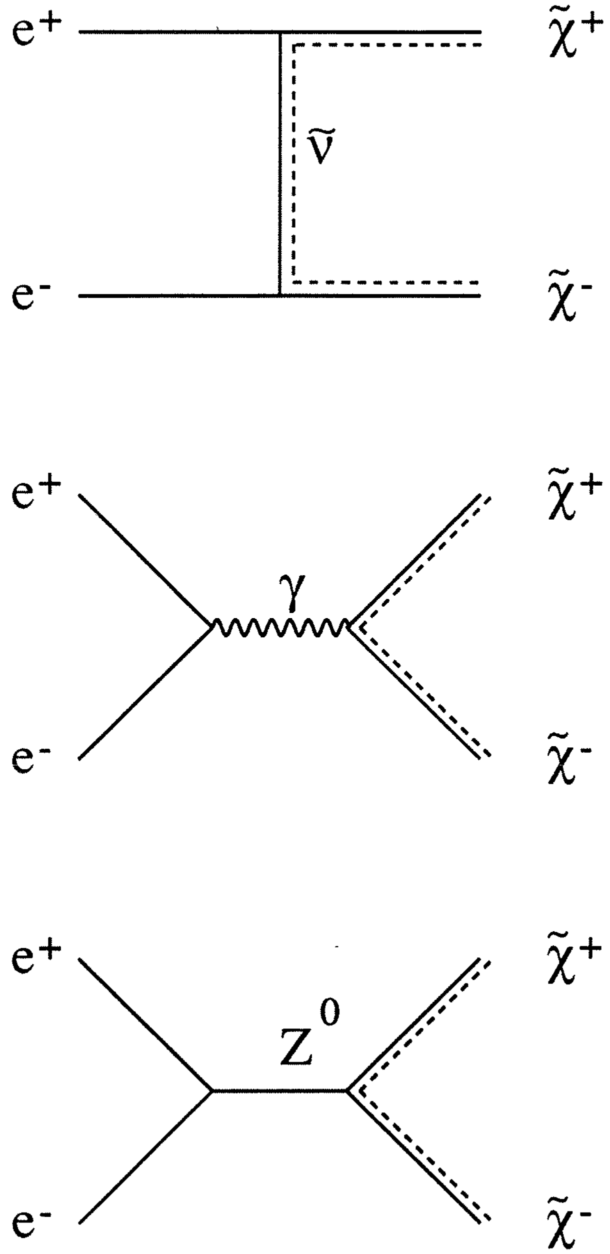

Figure 1.7: Feynman diagrams for chargino production.

State	g_L	g_R	$g_L^2 + g_L^2$
Normal lepton	$2\sin^2\theta_W$	$1 - 2\sin^2\theta_W$	0.5
Pure Wino	$-2 + 2\sin^2\theta_W$	$-2 + 2\sin^2\theta_W$	4.7
Pure Higgsino	$-1 + 2\sin^2\theta_W$	$-1 + 2\sin^2\theta_W$	0.6
Ideal mixture	$-2 + 2\sin^2\theta_W$	$-1 + 2\sin^2\theta_W$	2.7

Table 1.2: Coupling to the Z^0 for various charged fermion states.

where $\tilde{g}_L$ and $\tilde{g}_R$ are the couplings of the Z^0 to the electron and g_L and g_R are its coupling strengths to the $\tilde{\chi}^{\pm}$. The total cross section, angular distribution, and threshhold behavior depend on the mass of the chargino and also on g_L and g_R. Table 1.2 shows these couplings (given in reference [70]) for several different chargino states, namely pure wino, pure charged Higgsino, and the so-called "ideal mixtures" containing equal amounts of both. For comparison the couplings for a normal lepton are given. Figure 1.8 shows how the total cross section depends on the chargino mass. The different behaviours come from the different contributions of P- and S-wave to the total cross section, as one can see in equation 1.4.

Equations 1.3 and 1.4 exhibit the most important contributions to the pair-productions of charginos at the Z^0 pole. More complete expressions based on the MSSM may be found in reference [71]

Charginos decay by the reaction

$$\tilde{\chi}^{\pm} \rightarrow \tilde{\gamma} l^{\pm} \nu$$

proceeding through the diagrams of figure 1.9. The branching ratio into leptons depends on the relative amplitudes of the three graphs in 1.9, but we will assume a branching ratio of 1/9, which is what one would obtain by ignoring the second

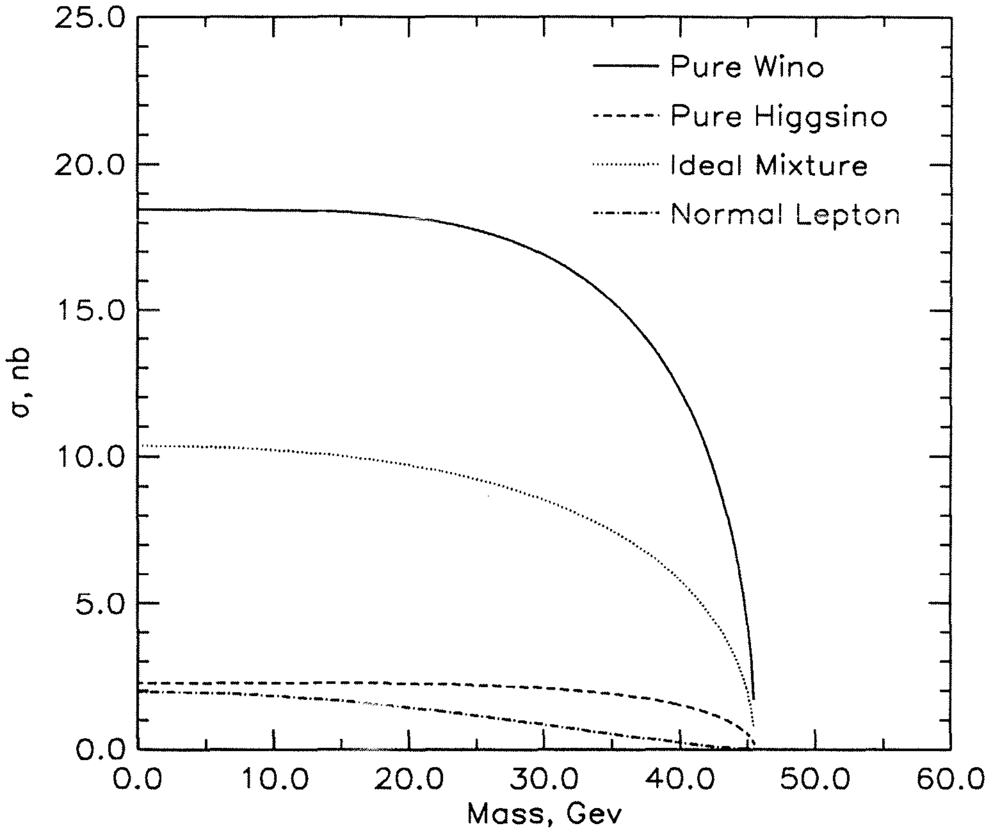

Figure 1.8: Chargino cross section vs. chargino mass.

two graphs, for example if the charged scalars were very heavy. This branching ratio could only be reduced if the squark-exchange diagrams were larger than the slepton-exchange diagrams. The range predicted by most models is 1/9 - 1/7 [66]

The spin 1/2 nature of the charginos means that in general there will be a correlation between their production and the decay, i.e., polarization of the charginos. The polarization, like the tau polarization from Z^0 decay, would depend on the relative strengths of the left- and right-handed chargino coupling to the Z^0, and this depends on only one parameter, which is the mixing between charged Higgsino and wino. In fact, some authors have considered the possibility of measuring this parameter by measuring the decay lepton distributions[72]; however this requires a different decay mode,

$$\tilde{\chi}^+ \rightarrow \tilde{\nu} l^+$$

than the one we consider here. The dynamics of this decay mode are similar to that of the tau decay into the mode $\tau \rightarrow \pi\nu$. A large chargino mass diminishes the polarization, however.

For the three body decay mode the effect is much smaller; the dynamics being similar to the tau decay $\tau \rightarrow \nu\bar{\nu}l$. This makes the search for charginos in the three body nearly independent on the mixing. Explicit calculations of the lepton energies from chargino decay have been carried out[73].

The program WINGEN [66,67], which incorporates correlations in production and decay, is used to simulate the signal. Modifications we made to this program include the incorporation of initial state radiation through the method

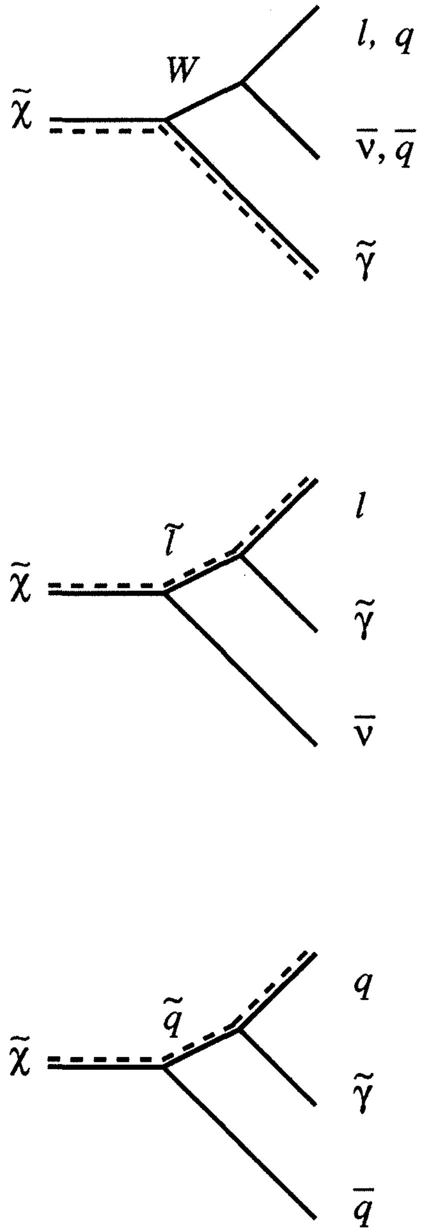

Figure 1.9: Feynman diagrams for chargino decay.

of Behrends and Kleiss[68]. As in the case of the charged sleptons, all calculations are performed within the context of the MSSM, however the results do not depend on the MSSM but only on the assumptions stated above.

1.5 Existing Experimental Limits

Previous experiments have already constrained the masses of charged scalar leptons and charginos, gluinos and squarks.

The best limits on unstable charginos and charged scalar leptons come from e^+e^- collisions, similar to the one described herein. The previous highest energies, and therefore the best limits, come from experiments at TRISTAN, where they are ruled out the beam energy of about 30 GeV[74].

The ASP experiment at PEP obtains limits on selectrons by studying the process:

$$e^+e^- \rightarrow \gamma\tilde{\gamma}\tilde{\gamma},$$

which proceeds through the t-channel exchange of a $\tilde{e}$, at a center of mass energy of 29 GeV[75]. A limit on the selectron mass of 60 GeV is obtained in the case of a zero-mass pure photino. The limit on selectron mass becomes worse with increasing photino mass and is nonexistent for photino masses above 15 GeV.

Proton colliders are also able to set limits on charged noncolored superpartners[76]. However the most important limits on supersymmetric partners from proton colliders are limits on squarks and gluinos, the partners of quarks and gluons [77,78,79]. The best limits on these particles are $M_{\tilde{g}} > 79$ Gev and $M_{\tilde{q}} > 74$ GeV.

Limits on neutralinos and sneutrinos from experiments prior to LEP and SLC are practically nonexistent[40]. Since the turn-on of LEP, several papers have appeared which constrain the neutralino sector; however, given the complexity of the mixing in this sector, these limits have so far always been stated in terms of the parameters of the minimal supersymmetric standard model[80,81].

Other LEP experiments have published limits on sleptons and charginos which are comparable to those published here [82,83,84]

The ALEPH collaboration has published an analysis of acoplanar events with missing energy similar to the one performed here, however using only 0.5 pb^{-1} of LEP data[85].

1.6 Limits from the Width of the Z^0

Before describing the search for pairs of acoplanar charged particles in the absence of photons, we will briefly say what can be learned about our signal from the width of the Z^0.

In a recent conference [86], the average of the Z^0 width from the four LEP experiments of 2498 $\pm$ 20 MeV was given, and compared to a standard model prediction of 2500 $\pm$ 42 MeV, where the error is mainly due to the uncertainty in the top quark mass. To 95% confidence, the measured width is less than 2530.8 MeV. If we reduce the standard model width by the theoretical uncertainty then the maximum additional width from non standard model sources is 73 MeV at 95% confidence.

The partial width of Z^0 decay into either charged sleptons or sneutrinos is given by the formula

$$\frac{\Gamma(Z^0 \to \tilde{l}\bar{\tilde{l}})}{\Gamma(Z^0 \to l\bar{l})} = \frac{1}{2}(1 - \frac{4m_{\tilde{l}}^2}{m_Z^2})^{3/2} \tag{1.5}$$

(l=e, μ, τ, ν) assuming mass degeneracy for the charged sleptons. No mass limit on charged sleptons can currently be inferred, since the equation 1.5 implies that even a zero mass charged slepton will contribute only about 42 MeV to the width.

For a single additional sneutrino we use the upper limit of the width and invert equation 1.5 to obtain a limit of 13.2 GeV as the lower limit for the mass of the sneutrino. If one assumes that there are three degenerate sneutrinos, one for each generation, then the lower limit is 34.1 GeV.

The partial width of the Z^0 into charginos is

$$\Gamma_{\tilde{\chi}^+\tilde{\chi}^-} = \frac{\sqrt{2}}{32\pi} G_F M_Z^3 \beta \left\{(1 + \beta^2/3)(g_l^2 + g_r^2) + 2(1 - \beta^2)(g_l g_r)\right\}. \tag{1.6}$$

with g_l and g_r as in table 1.2. The limits are 45.5 GeV for a pure wino and 38.5 GeV for a pure higgsino. This limit for pure wino is nearly identical to that coming from the direct search which we are about to describe; it is especially interesting because it does not depend on any assumptions about the decay mode of the wino. However the limit from the direct search for a pure Higgsino improves by about 7 GeV the limit from the width.

Chapter 2

The LEP Accelerator and the ALEPH detector

The LEP accelerator is a circular electron-positron storage ring measuring 27 kilometers in circumference, located on the French-Swiss border near Geneva, Switzerland. The accelerator is designed to operate in an initial phase (LEP I) at a center-of-mass energy of about 90 GeV with a maximum of about 110 GeV. In a second stage, LEP II, the energy may be upgraded to a maximum of about 200 GeV, by replacing some copper RF cavities with superconducting cavities and increasing their number. Four counterrotating bunches of electrons and positrons circulate in the tunnel and collide at four interaction points, each of which is also the site of a large general-purpose particle detector.

Electrons and positrons in LEP are produced and accelerated in several steps (figure 2.1) . First a 200 MeV high-intensity electron linac produces positrons by colliding the beam into a converter. Then a second linac accelerates both positrons and electrons (from a separate source) to 600 MeV, and transfers them to an Electron-Positron Accumulator (EPA). From there they are transferred to the PS, first two proton bunches then two electron bunches, during the approximately 5 second long dead time in the SPS proton cycle. In the PS the energy of both beams is raised to 3.5 GeV, and then transferred to the SPS where it is further increased to 20 GeV and injected into LEP. LEP operates simultaneously with the SPS fixed target program, however it is not compatible with the use of the SPS as a proton-antiproton collider.

LEP was commissioned during the summer of 1989, and ran initially at energies close to the peak of the Z^0. The first hadronic decays of the Z^0 at LEP were seen in August of 1989. Several physics runs were completed before a shutdown from the end of December until March of 1990. The highest priority for the LEP experiments was to measure the electroweak parameters to high precision, and to that end the run strategy was to scan above, below, and on the Z^0 resonance with about 50% of the luminosity on-peak and 50% of the luminosity divided equally above and below the peak. The lowest center-of-mass energy was 88.3 GeV, and the highest was 94.3 GeV.

The luminosity increased steadily during 1989 and 1990, attaining a peak value of $4.9 \times 10^{30}\mathrm{cm}^{-2}\mathrm{s}^{-1}$. The design luminosity is $1.7 \times 10^{31}\mathrm{cm}^{-2}\mathrm{s}^{-1}$. Currents were typically from 1-1.5 mA, and beam lifetimes of longer than ten hours were usual. By the middle of May, 1990, an integrated luminosity of 2.4 pb^{-1} was accumulated, corresponding to about 55,000 hadronic decays of the Z^0.

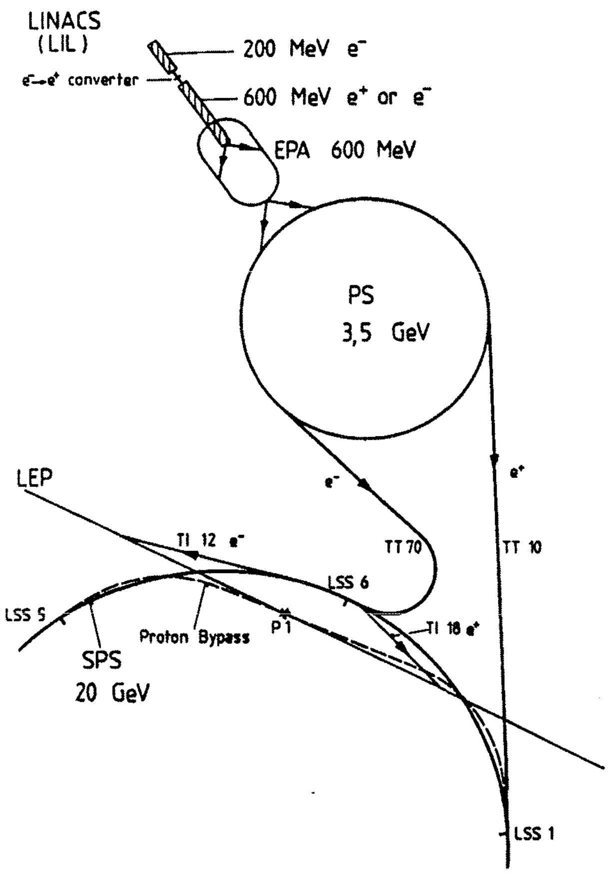

Figure 2.1: LEP and its injector chain, consisting of the LIL, EPA, PS, and SPS.

2.1 The ALEPH detector

The ALEPH (Apparatus for LEP physics) detector is shown in diagram 2.2. It is a large, multipurpose detector with nearly 4π solid angle coverage. Nearest to the beam pipe is a silicon strip microvertex detector. In 1989 only 1/6 of the microvertex detector was installed and it was not used for physics studies, and in 1990 the rest of the detector was installed and operational. Surrounding this is a multilayer axial-wire drift chamber, the Inner Tracking Chamber (ITC), which gives eight accurate $r\phi$ coordinates for tracking is also a triggering device. Next is a large Time Projection Chamber (TPC), which constitutes the primary tracking device of ALEPH and performs particle identification through the measurement of ionization loss. A finely segmented electromagnetic calorimeter (ECAL), consisting of alternating layers of lead and proportional tubes, lies outside the TPC but within the superconducting coil. This liquid helium cooled coil provides a 1.5 Tesla uniform magnetic field for momentum measurement by the TPC. Its field is returned in a large iron structure that supports the experiment and is itself a fully instrumented hadronic calorimeter (HCAL). Limited-streamer tubes fill hollow slots in the HCAL and produce a digital pattern for tracking, as well as an analog signal from projective towers for an energy measurement. Finally, over 92% of the solid angle is surrounded by muon chambers which measure a three-dimensional coordinate for penetrating charged particles. One layer was installed in 1989 and a second is forseen.

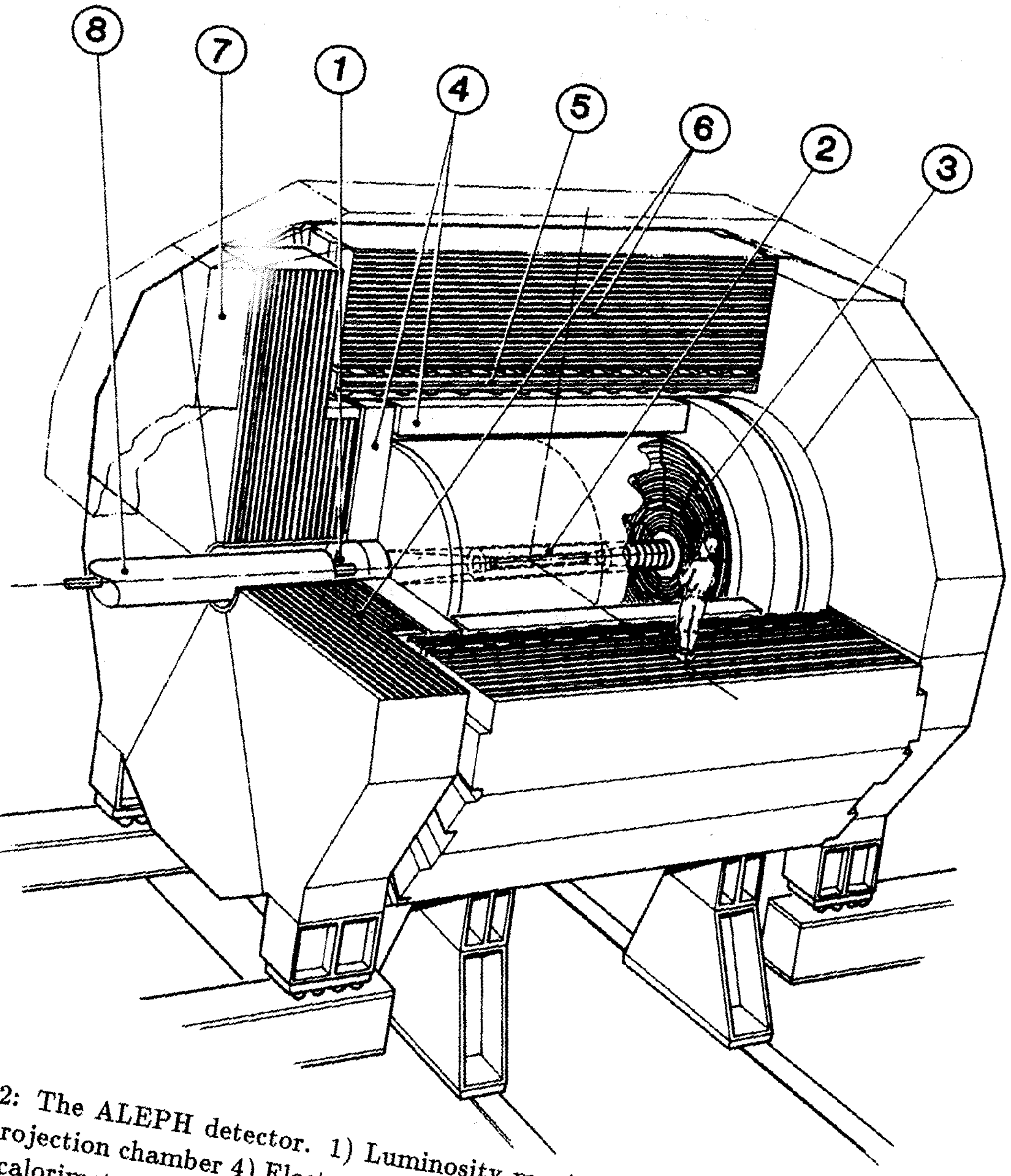

Figure 2.2: The ALEPH detector. 1) Luminosity monitor 2) Inner tracking chamber. 3) Time projection chamber 4) Electromagnetic calorimeter. 5) Superconducting coil 6) Hadronic calorimeter. 7) Muon chamber. 8) Low-beta superconducting quadrupoles.

Luminosity is measured by a luminosity calorimeter (LCAL) of nearly the same construction as the ECAL but located at a small angle to the beam direction. A small angle tracker, SATR, performs tracking in the same region.

The analysis described in the following chapter uses the ITC and the TPC for tracking and momentum measurement, the ECAL for triggering and for the veto of photons, the HCAL as a triggering device, the LCAL for the measurement of luminosity and also as a veto on low-angle energy deposits. We will next discuss each of these detectors, and the ALEPH trigger, in some detail. More details on the experimental apparatus can be obtained in reference [87].

2.2 The Time Projection Chamber

The main tracking device of ALEPH is the Time Projection Chamber, or TPC. The TPC determines, at large radii, 21 space-coordinates whose resolution is about 160 μm in $r\phi$ and about 1 mm in z. In addition it samples the ionization energy loss up to about 300 times for typical tracks, which is useful in particle identification. The TPC provides also some information to the trigger by updating ITC tracking information with TPC tracking information.

The TPC, shown in figure 2.3, is unlike conventional drift chambers in many different ways. The most striking difference is the absence of sense and field wires thoughout the active drift volume. Instead ionization electrons are drifted from their point of production towards either end of the cylinder, where multiplication and readout takes place. The second important difference is the crucial role played by the strong magnetic field in a TPC. The magnetic field is aligned with the electric field, and at high field the drifting electrons follow the magnetic field lines to first order and not the electric field lines. Also the magnetic field limits diffusion in the plane perpendicular to the magnetic field lines, which in ALEPH is the $r-\phi$ plane. The accurate position measurement in $r\phi$ is derived from the sharing of charge induced on adjacent cathode pads, not from wires. The sense wires are also read out, but their signals are used only as dE/dx samplings. Finally the TPC requires "gating", a way of keeping the zone surrounding the sense wires transparent to drifting electrons while trapping the ions which drift towards the main TPC volume.

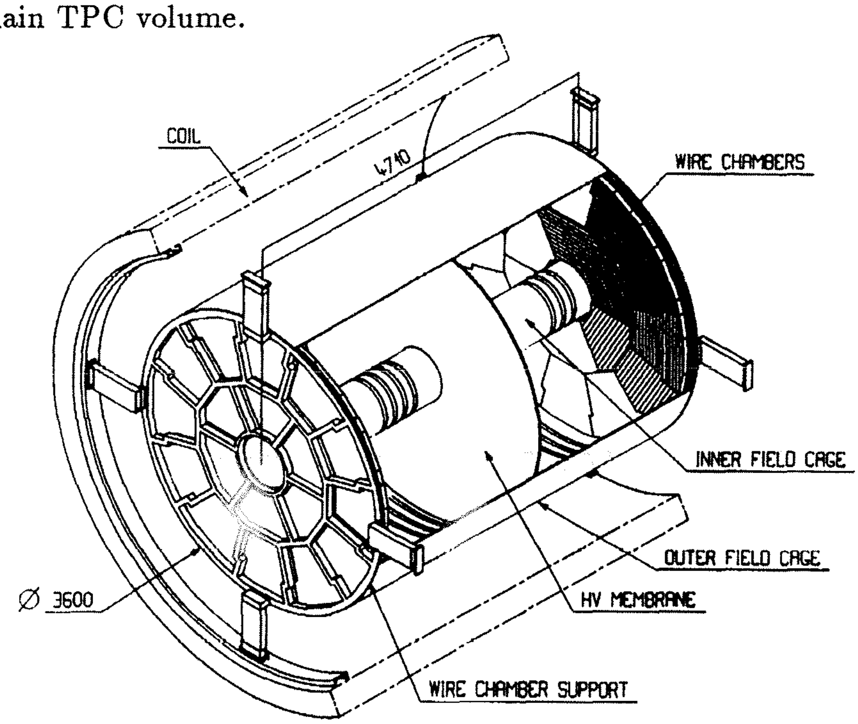

Figure 2.3: The ALEPH TPC

The TPC has an inner radius of 0.3 m and an outer radius of 1.8 m, and is 4.7 m in length. Either end of the cylinder is at a potential of near ground. At the center of the chamber is a central membrane made of a sheet of Mylar coated with graphite and held in place at its periphery. The normal operating voltage of the membrane is -26 kV, so the electrons move in a field of approximately 115 V/cm towards the closest end. On the inner and outer cylindrical walls of the TPC, built of Mylar and aluminium, are copper strips printed on kapton and a resistor chain which smooths the electric field inside the TPC.

The active end of the TPC is the endcaps, where the wire chambers, electronics, and cooling circuits reside. The pad rows lie in 21 concentric rows (figure 2.4), and a plane of alternating sense and field wires lie above the pad rows and tangent to them. The rectangular pads measure 6.202 mm in the the azimuthal dimension and 30 mm in the radial dimension. Sense wires are spaced every 4 mm (and are interleaved with field wires), so roughly 7-8 sense wires lie above every pad. For convenience the endcap is divided up into 18 sectors of three different shapes. This enables easy replacement of a damaged part of the TPC, for example, should a wire break. One also finds on the sectors a plane of cathode wires to control the electric field, and a plane of gating wires about which more will be said later. See figure 2.5 for a detailed view of the three wire planes.

Signals on the cathode pads are developed through the capacitive coupling of the pads to the sense wires. For an avalanche on a single wire, the signal developed on each pad will depend on the distance between the avalanche and the pad's center. The exact dependence is known as the pad response function, and it has been measured to have a nearly gaussian shape [88]. Of course the signal on a pad is the superposition of signals from several sense wires. Once

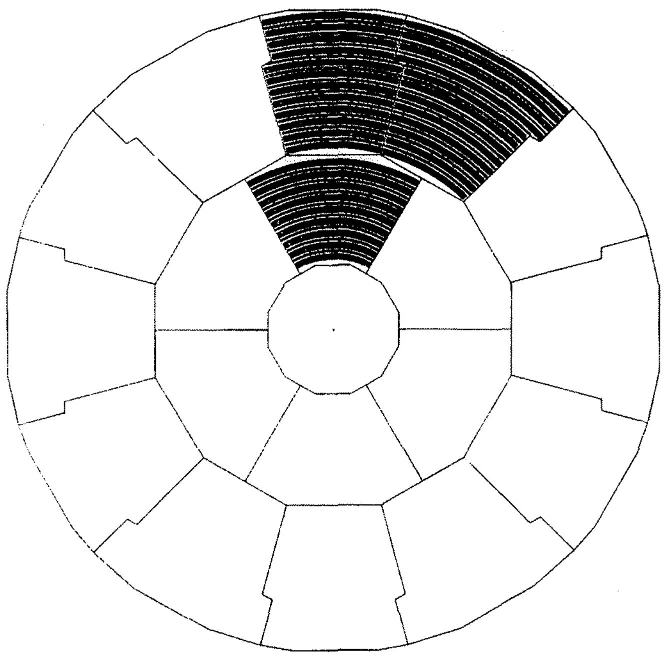

Figure 2.4: Configuration of TPC sectors on an endcap. Concentric padrows are shown for three of the sectors.

the σ of the pad response function is measured, one can obtain the position along the wire of the avalanche by using the relative charges on neighboring pads. The coordinate in ϕ may thus be obtained with a precision much smaller than the actual dimensions of the pad. The radial position is known from the position of the pad row, and the z-position can be obtained from the drift time. Each measured coordinate is three-dimensional, which eases the reconstruction of charged tracks. This method of coordinate-finding imposes tight requirements on the uniformity of gain from channel to channel, so electronic calibration system [89] has been designed to calibrate the 50,000 channels of the TPC by injecting pulses at various points along the electronics chain.

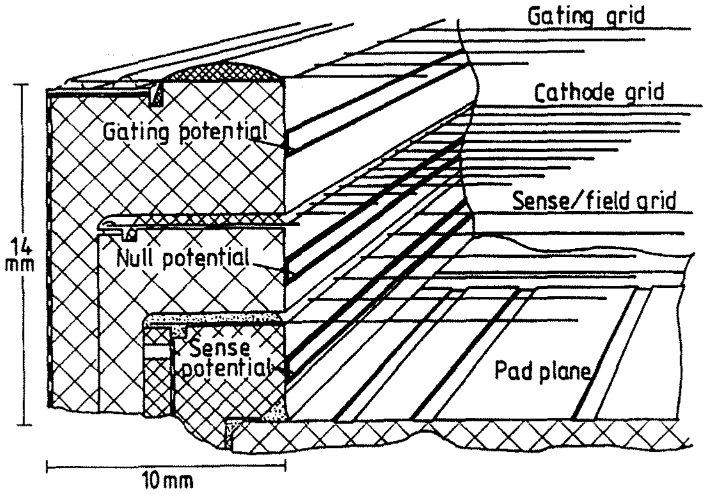

Figure 2.5: A close-up view of a single TPC sector showing the pad plane and the three wire grids.

The resolution of the TPC is affected by several things. Diffusion in the gas is one source of reduced resolution. Normally the diffusion of electrons would be about 6 mm after one meter of drift in the TPC's mixture of argon-ethane (91%-9%) at atmospheric pressure. However this is modified in the presence of a magnetic field. The diffusion then is determined by the quantity $\omega\tau$, where ω is the cylclotron frequency of electrons in the magnetic field and τ is the mean free time between collisions of the electron with gas molecules; then the diffusion is reduced by a factor $(1+\omega^2\tau^2)^{-1}$ [90]. The gas mixture in ALEPH was partially chosen for the high values of $\omega\tau$, which are about 7-8.

In addition to diffusion, distortions can occur in the TPC owing to irregularities of the electric and magnetic field within the drift volume. At high values of $\omega\tau$ the magnetic field mainly determines the drift direction; however, there is also a component along the direction of $\mathbf{E} \times \mathbf{B}$. For the TPC, the most dangerous kind of distortions are the azimuthal distortions, since these can lead to errors in measuring the sagitta of curved tracks, which translate into mismeasurements in the track momentum. To constrain such distortions imposes limits on the radial component of the electric field (from $\mathbf{E} \times \mathbf{B}$), the radial component of the magnetic field (from $\mathbf{E} \times \mathbf{B}$), and the azimuthal component of the magnetic field (from first order effects). The magnetic field has been mapped using hall plates and NMR probes, with radial and azimuthal field components of several tens of gauss being discovered. Such components are undesirable and can lead to distortions up to 1.5 mm in the worst case [87].

Track distortions coming from field nonuniformity or alignment error can be detected, measured, and corrected with a laser calibration system. Two Nd-YAG ultraviolet lasers are located on top of the aparatus. Their beams are steered through two conduits to the TPC endcap where a splitter ring divides each into three beams, which then are conducted to distribution elements close to the central membrane, where they are further divided five times and sent through the main TPC volume, for a total of 30 tracks. By measuring the apparent sagitta of the straight tracks one can correct for sagitta errors in charged particle tracks. In addition, since the angles between the tracks are well known, the drift velocity can be measured from the drift time difference. Laser tracks are shown in figure 2.6.

The need for gating a TPC was discovered in previous attempts to operate them [91]. The multiplication of electrons on the sense wires creates positive ions which drift at low velocities back through the drift volume. The space charge

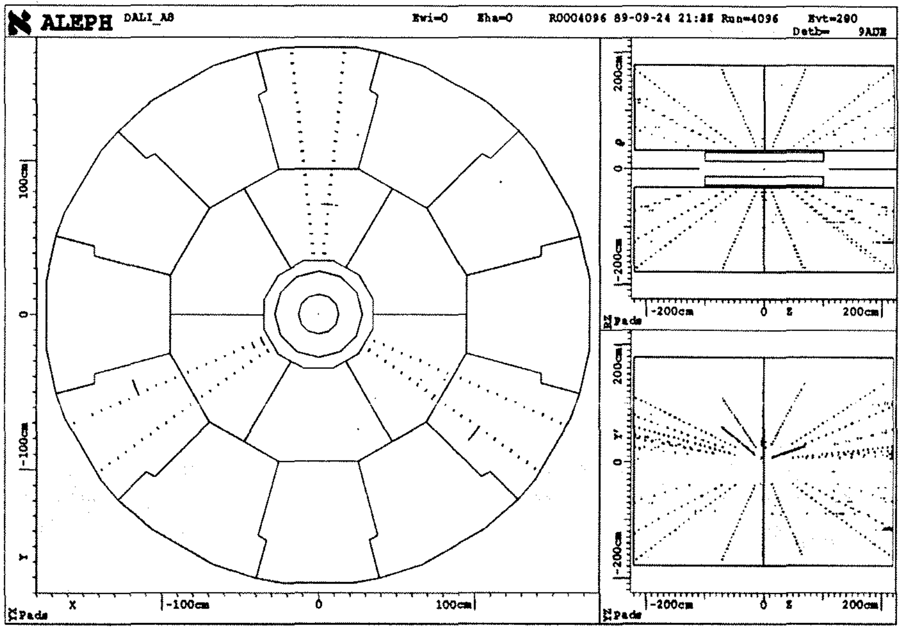

Figure 2.6: Laser tracks in the ALEPH TPC.

so accumulated can cause large distortions in the tracks. ALEPH has observed distortions of several centimeters in laser tracks when the gating is turned off.

Gating assures that the drift region remains free of positive ions. A gating grid separates the sense wires from the drift region. The gate may be held "open" by placing a potential of nominally -67 volts on all wires. To "close" the gate it suffices to add and subtract a difference potential of about 40 volts to alternate wires. Electric field line maps in the case of open and closed gating grids can be seen in figure 2.7

The grid is opened and closed synchronously with the beam crossing. About 3 μsec prior to the crossing of a bunch, the gate is opened making the gate transparent to both ions and electrons. After the crossing it is closed *unless*

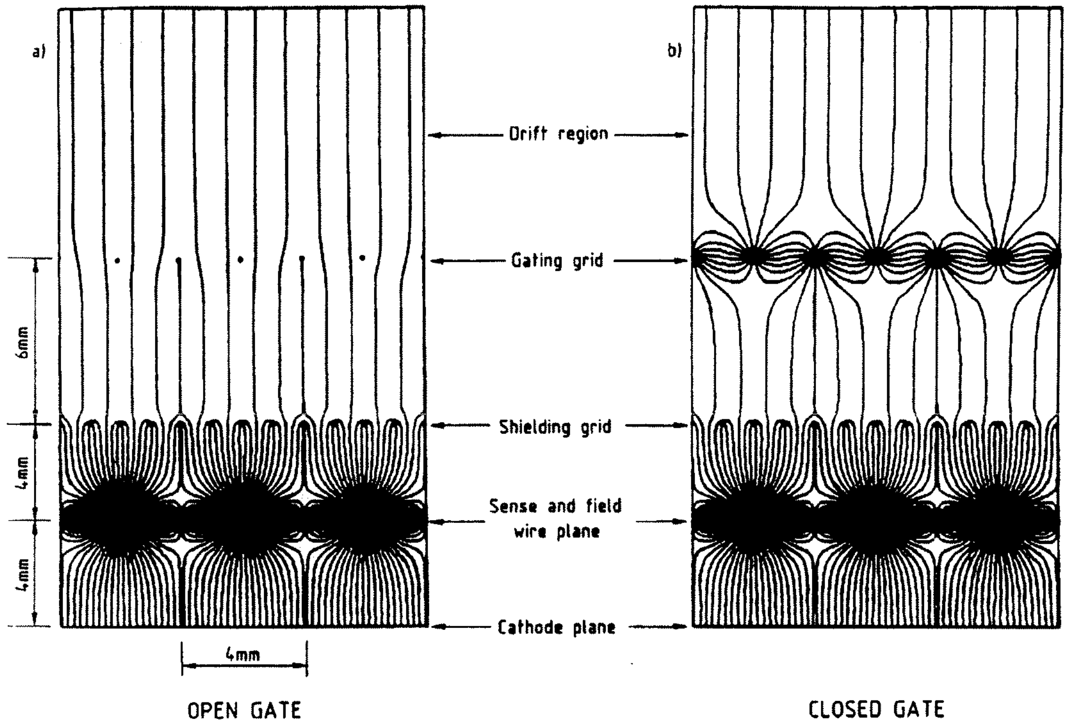

Figure 2.7: Electric field lines on the gating grid for open and closed states

a level-1 trigger YES is received by the TPC. In this case it waits until the 45 μsec drift time has elapsed before closing the gate. Because the ions move slowly though the gas, they see many cycles of gating before they reach the grid, and the net effect of their zigzag motion in the alternating magnetic field is that they are trapped on the negative gating wires.

2.2.1 TPC electronics

50,000 pad and wire signals are read out from the TPC. A large array of electronics amplifies, digitizes, buffers, reduces, and formats this enormous amount of information before transferring it to the online VAX. The system is connected by a Fastbus network broken into 36 clusters (one for each sector) of three crates each. Each contains a TPP, which is a processor built around the Motorola 68020 chip. The TPP usually acts as a slave during data acquisition or calibration activities.

Charge-sensitive preamplifiers on the sectors amplify the signals, then send them over twisted-pair cable to shaping amplifier and eight-bit flash ADC's in Fastbus modules known as TPD's. The flash ADC's digitize 512 "time buckets" at a 11.4 MHz clock rate, then perform zero-suppression to keep only the pulses which rise above a programmable threshold. Four events at a time can be buffered in the TPD. During a run the digitizations from a sector are read from the TPDs into the TPPs. Following this all TPPs are read into one of two Event Builder (also a 68020-based microprocessor). Finally the two events builders are read into a main event builder and sent to the Main Online VAX together with formatted output from other subdetectors.

The gain of the ADCs is set by the voltages of four tap points along the resistor chain, and this in turn is set by four DAC's which are also found in the TPD. To calibrate a single channel, pulses of different amplitude are injected into the field wires, inducing a signal on the neighboring sense wires and on the pads. The tap point voltages are adjusted until the gain curve is linear and uniform from channel to channel. Sectors are calibrated every few weeks when data acquisition activities are stopped. Normally, all thirty-six sectors calibrate in parallel under the control of a TPP; the results are then sent to a VAX computer.

The pulses are generated by 36 Sector Controllers (SC) which reside in the sectors. They are under the control of a Sector Test Pulse Controller (STPC) in the Fastbus crate, which can talk to the TPP's. In addition to the field wires, the SC and STPC can pulse at the input of the preamplifiers and of the shapers. One uses this as a troubleshooting tool.

2.2.2 Trigger signals from the TPC

Signals originate from special trigger pads in the TPC covering an angular region of 15° and lying between rows of normal pads. These signals are used only in the trigger to detect ionizing particles in θ and ϕ segments of the detector. They are processed through the same electronics as regular TPC signals. Twenty-four dedicated processors search for tracks originating at the origin. These signals are not used in the level-one decision because the TPC drift takes a full 40 μsec, whereas the beams cross every 23 μsec.

2.3 The Inner Tracking Chamber

The Inner Tracking Chamber (ITC) is a conventional drift chamber sitting inside the TPC, and having an inner radius of 12.8 cm, an outer radius of 28.8 cm, and an overall length of 2 m. It serves two purposes in ALEPH. The first is to provide the only tracking information to the first-level trigger, and the second is to provide an additional eight accurate coordinates in $r\phi$ at smaller radii to the TPC. Eventually ITC tracks may be used to link TPC tracks to microvertex detector tracks.

The ITC consists of 960 sense wires strung between two aluminum end-plates. Surrounding each sense wire in a hexagonal lattice are field wires; thus the basic unit of the ITC is the hexagonal "cell" with the sense wire at the center, as shown in figure 2.8. Cells are organized into eight concentric layers; in the four inner layers there are 96 cells, and in the four outer layers, 144 cells. The cells in neighboring layers are "staggered", that is, the center of the cells from layer to layer are offset by half a cell width. This helps to resolve the left-right ambiguity

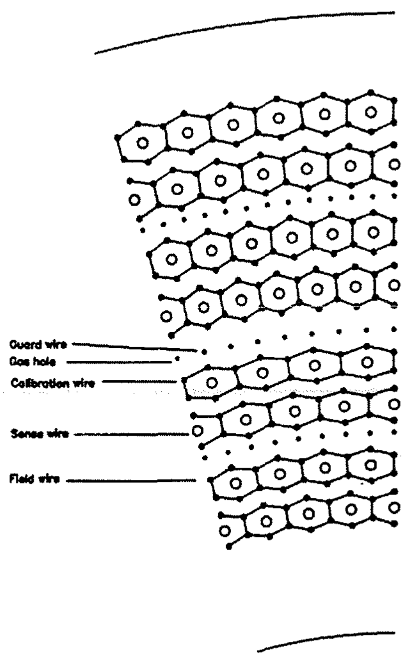

Figure 2.8: Configuration of wires in the ITC endcap. Calibration wires are similar to field wires except they may be pulsed to induce equal-time signals in the amplifiers at both ends.

of tracks. Every two layers are separated from the neighboring two layers by guard wires also strung in the z-direction. Circular rings of 100 μm aluminum wire are glued to the guard wires, thus forming a cage. The purpose of the cage is to contain broken wires to a limited volume of the ITC so that the rest of the ITC can remain operational. Since the ITC is used in making trigger decisions, the ALEPH detector would become seriously limited by the loss of the ITC.

The r coordinate of the ITC is known from the position of the struck wire, and the $r\phi$ coordinate is obtained from the drift time. In addition to the r and $r\phi$ coordinates, a z-coordinate is found with a resolution of about 3 cm, by comparing the arrival time of pulses at either end of the wires, which run along z. The gas mixture used in the ITC is a 50-50 mixture of argon and ethane at atmospheric pressure.

The cell size must be kept small so that the drift time is low, and the values chosen permit trigger signals from the ITC to be ready in 2-3 μsec, which is small compared to the 23 μsec beam crossing time. This results in a large number of cells and a high stress on the aluminum endplates. This stress is borne by a carbon fiber tube which forms the outer wall of the detector. It supports the stress of the wires while adding only 1% of a radiation length between the ITC and the TPC. The inner wall consists of a polystyrene "low-mass" tube with 2% of a radiation length.

The active part of the ITC is extended by cylindrical aluminum structures which house preamplifiers, high-voltage distribution boxes, and cables, the whole of which is carefully held near the outside of the structure so as not to overlap the luminosity calorimeter acceptance (figure 2.9). These structures also enclose the active volume of the ITC in a gas-tight zone. They extend the ITC to the the edge of the TPC with which it is aligned and fastened.

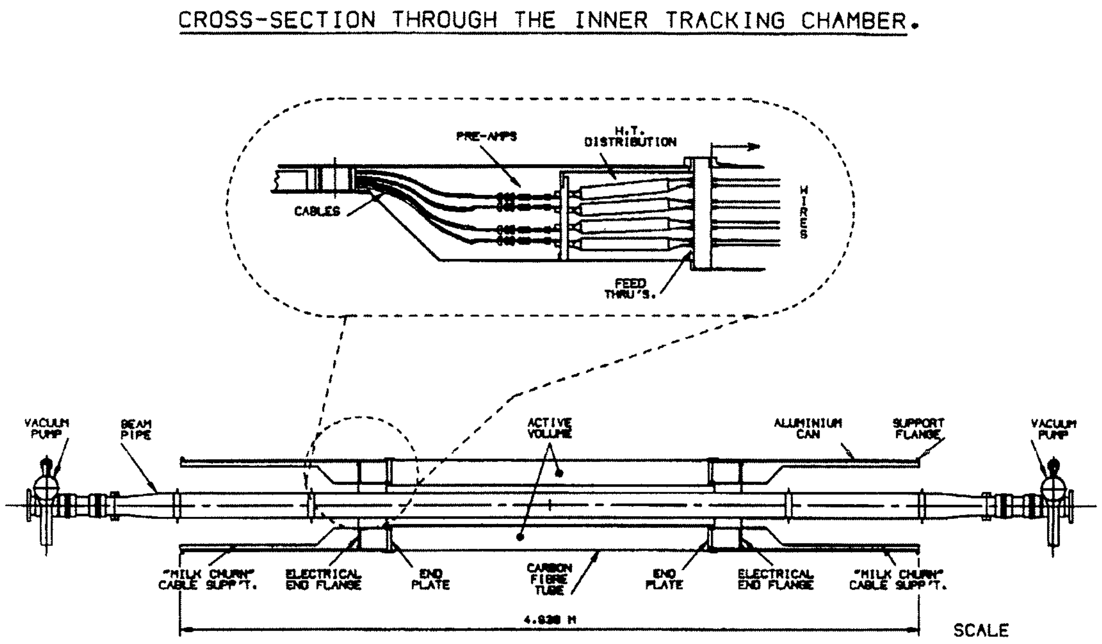

Figure 2.9: Mechanical structure of the ITC

2.3.1 Readout of the ITC

The 960 preamplified signals are transmitted along a length of 50 Ω coaxial cable to a counting room where the rest or the ITC electronics are located. Eventually three signals are derived:

- Z-timing signals sent to the Z-digitizer for measurement of z-coordinate
- Latched TTL signals sent to the $r\phi$ trigger processor and used to set a trigger mask
- Discriminated drift-time signals sent to CAMAC TDCs for $r\phi$ coordinate determination.

The Z-timing signals are generated by comparing the arrival time at one end of the wire with that from the the other end, and are used to obtain a z position along the struck wire. This measurement however was not operational in part of 1989 and is not used in the event reconstruction. We will not discuss it any further.

The latched TTL signals hold the pattern of hit wires. They are sent to a special trigger processor called the $r-\phi$ processor to generate a trigger mask from the ITC. Within a unit consisting of eight outer cells and four inner cells, the processor looks at the pattern of wires hit and determines if that pattern is valid. The list of valid patterns is flexible and programmed into the processor at the start of run by a microprocessor (the event builder), which can account for dead wires when generating the list. The latched TTL signals are static, remaining high until they are reset. 60 trigger bits are set according to whether the valid mask was detected in the angular region of one of the 72 trigger segments. Additional bits are set for special purposes, for example to tag back-to-back tracks. This method of deriving trigger masks introduces a lower track energy trigger threshold of approximately 1.0 GeV.

Finally, the drift time for each hit is measured in CAMAC TDCs. This measurement gives a coordinate measurement with a resolution of about two hundred microns. Single-hit electronics are used, the small cell size helping to achieve two-track resolution.

2.4 Performance of the Tracking Detectors

Both the TPC and the ITC performed at the desired level. Nonetheless, it was not until after much work had been done towards understanding alignment, magnetic field distortions, and drift behaviour that the systematic errors affecting the performance were understood and corrected for. Matters were complicated by the fact that, in the ITC, a leak was detected which required that the flammable argon-ethane mixture be replaced by a nonflammable mixture of argon and CO_2 (80%-20%), while in the TPC, small superconducting coils to compensate the main coil could not be powered for part of the run. Several iterations of reprocessing (the reconstruction) were performed to correct for these problems.

Dimuon events with $|\cos\theta| < 0.8$ are used to measure the efficiency, coordinate resolution, and momentum resolution of the ITC and the TPC.

Coordinate resolution for the TPC is on the order of 160 μm in $r\phi$ and 1.2 mm in z. Distributions in residuals are shown in figure 2.10 for both $r\phi$ and z (both ITC and TPC were used to in the track fit). One sees that the distributions are well described by a gaussian. For the ITC the resolution varied depending on gas mixture and on operating voltage but was generally on the order of 250 μm.

Momentum resolution for high p_t tracks reached the goal of $\frac{\Delta p}{p} = .0015p$ for the TPC alone. When the ITC is added to the fit the resolution improves to roughly $\frac{\Delta p}{p} = .0010p$. In figure 2.11 one can see the gaussian behavior of $\frac{E_{beam}}{p}$ and the width of 4.3%, corresponding to 4.3% momentum resolution.

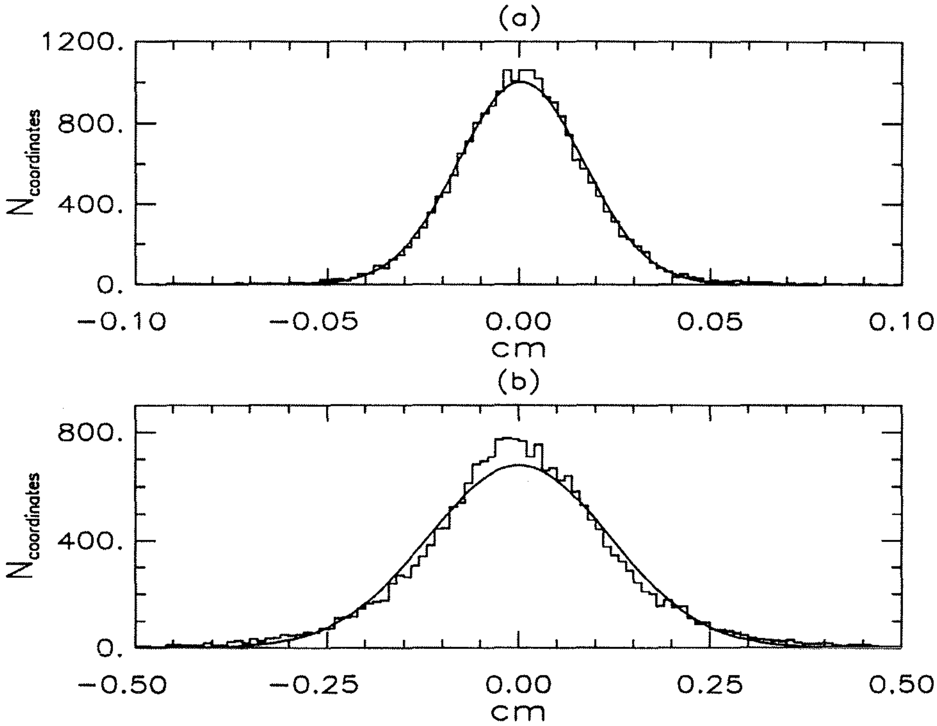

Figure 2.10: Distance from coordinates in the TPC to fitted tracks, for dimuon events. a) in $r\phi$ b) in z

Finally, in two-prong events, one can measure the trigger efficiency for segmented triggers directly from the data in a procedure to be discussed in a later section. Neither the ITC nor the TPC was found to be the source of any trigger inefficiency.

2.5 The Electromagnetic Calorimeter

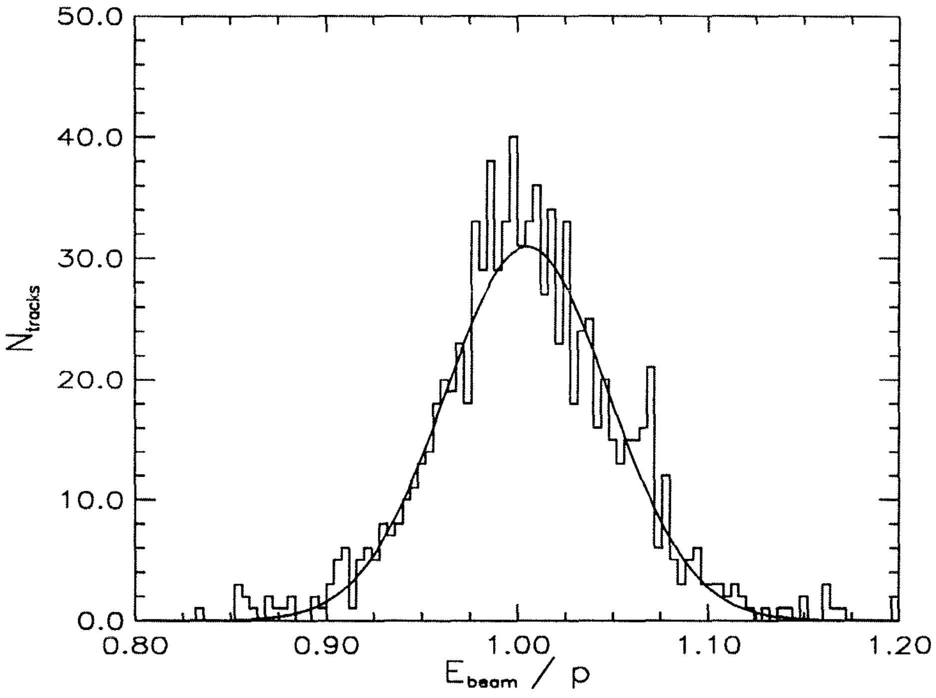

Figure 2.11: Distribution of E/p for dimuon event tracks fit to TPC and ITC coordinates, showing a 4.3% resolution at near 45 GeV

The electromagnetic calorimeter in ALEPH was designed for both good energy resolution and angular resolution. It is built in 36 modules, twelve barrel and twelve in either endcap, and covers 3.9π in solid angle (figure 2.12). It is placed within the superconducting coil to keep the amount of material in front of the ECAL small. Each module contains 45 layers of lead interleaved with proportional wire chambers. Cathode pads are present on each layer of wire chambers, and their signals are summed into so-called "towers" oriented towards the inter-

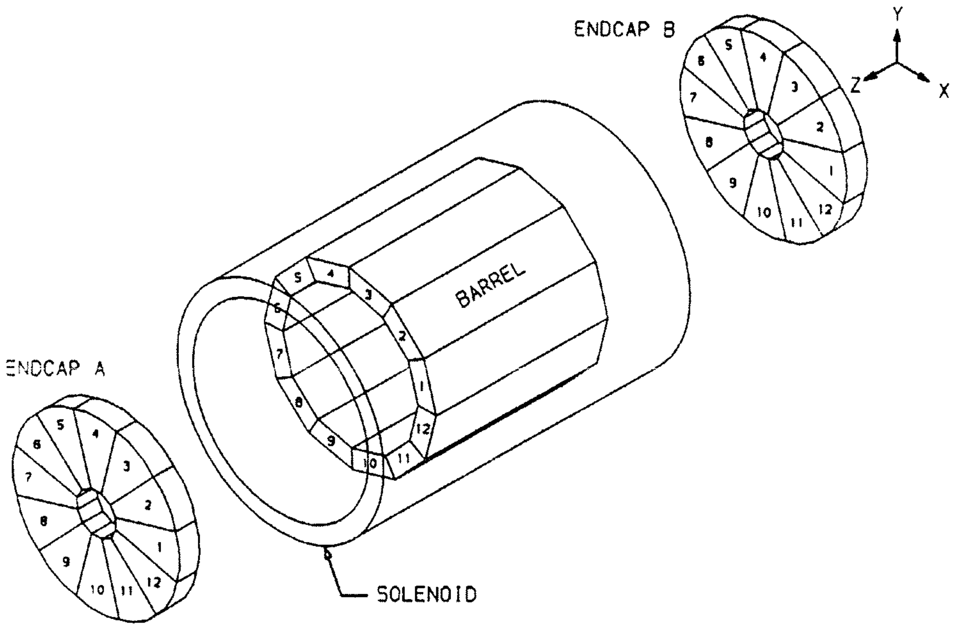

Figure 2.12: The Electromagnetic Calorimeter, barrel and endcaps

action point. There are 77,728 towers in all, read out in three separate "stories". Each has an angular width of about $1^\circ \times 1^\circ$. In addition, each wire plane is read out separately in every module. The wire signals are very low-noise and provide, in addition, an excellent energy trigger which has been proven to work at a threshold as low as 200 MeV. The pad signals are useful in providing information on spatial location and profiles of showers and can identify electrons and photons within jets.

Both the endcap and barrel modules have similar construction. In depth they are divided into three stacks. The first stack is about four radiation lengths (10 layers of 2 mm lead sheets); in the second about nine radiation lengths (23

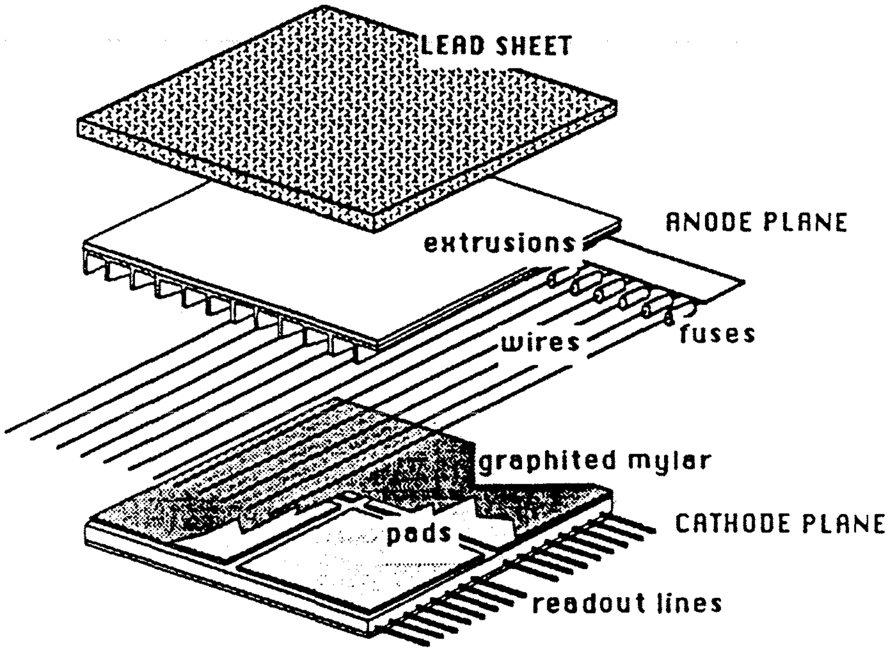

Figure 2.13: Construction of the wire planes in the ECAL

layers of 2 mm lead sheets), and in the third there are 12 layers of 4 mm lead sheets for about nine more radiation lengths. The wire chambers between these sheets (see figure 2.13) are constructed from aluminum sheets with extrusions. 25 μm gold-plated tungsten wires lie between the extrusions; in the barrel these wires run along z and also along the magnetic field. The open end is insulated from the pads by a sheet of highly resistive graphite-coated Mylar. The pads themselves are copper plated on a sheet of PVC. The whole module is contained in a gas-tight aluminium box. The gas mixture is $Xe - CO_2$, chosen for its low $\omega\tau$ so that ionization electrons do not spiral along magnetic field lines parallel to the wires, introducing large path-length fluctuations.

ECAL pad signals are amplified and integrated on the modules, pass into sample-and-hold circuits, are then multiplexed in groups of 32 before being sent through cables to Fastbus modules in an electronics barrack. Two cable drivers are used, one with a gain of unity and the other with a gain of 8, in order to obtain an effective dynamic range of 2^{16} from the 12-bit ADCs. Within the Fastbus module 8 channels are further multiplexed together, so that each ADC digitizes 256 pad channels. The entire operation of sampling, multiplexing, and digitizing takes about 3.7 msec and is controlled by a microprocessor in a Fastbus module. The digitizations are then read out by Fastbus read out controllers (ROCs) which perform pedestal subtraction and gain correction before sending them to the online VAX via an event builder.

The electronics chain is similar for wire planes except that, owing to their small number, they are integrated and multiplexed in Fastbus modules, instead of directly on the module.

The energy calibration of the ECAL is a complicated procedure relying on ^{55}Fe test chambers, wire pulsing, cosmic ray muons, the injection of radioactive ^{83}Kr into the gas system, test beam, and Bhabha events. The reader is referred to [87] for the details of the calibration procedure

2.5.1 Performance of the ECAL

The biggest problem with the ECAL in is a drift in the pedestals. This was related to a problem in the mulitplexer boxes and affected 32 channels at a time. The result is that a certain number of towers are "live", and the apparent energy can be quite large. This problem is corrected in two ways. First, a cleaning procedure is performed to supress live towers by looking at ten Bhabha events preceeding a given event. If a single tower has fired more than 20% of the time, then that tower is flagged as "live" for that event and suppressed from the production output tape. Fewer than 1% of the towers require suppression. Secondly, no tower energy is written to the production output tape unless a signal is simultaneously seen in the wire planes of that module. In addition, ECAL tower pedestals are measured every two hours or so.

With this treatment of the ECAL raw data, the performance of this subdetector was nearly at its design level. The energy resolution after a final calibration with Bhabha events is consistent with $1.6\% + 17\%\sqrt{E}$ for wires and $1.7\% + 19\%\sqrt{E}$ for towers. Electrons above 2 GeV are identified in the calorimeter from the TPC momentum-ECAL energy balance and from the longitudinal development of the shower. In addition the longitudinal development of an electromagnetic showers may be observed in finer segmentation on the 45 wire layers, provided other hadronic showers are not present in the same module.

2.6 The Hadronic Calorimeter

The hadronic calorimeter is similar in geometry to the ECAL. The absorber however is iron rather than lead, since this calorimeter is also the return yoke for the magnet. Cracks in the HCAL are anti-aligned with cracks in the ECAL. The tubes are constructed from graphite-coated plastic and operated in streamer mode rather than proportional mode; they are arranged in 23 layers throughout the iron. The HCAL has a readout of towers similar to that of the ECAL, except that the pads are larger, their angular diameter being close to $3^\circ \times 3^\circ$, and the

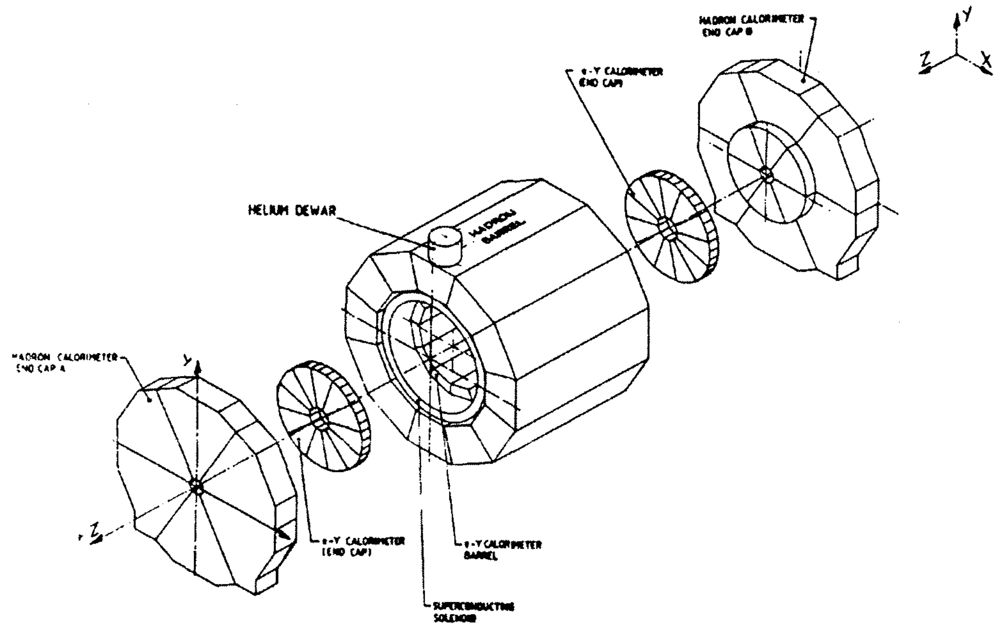

Figure 2.14: The Hadronic Calorimeter, barrel and endcaps

the projective towers are not read out in separate stacks. The energy resolution of this calorimeter is about $80\%/\sqrt{E}$ for hadronic showers.

Two other signals originate from the HCAL. "Strips" are long pads plated on one side of the plastic streamer tubes over the wires and running the wires' full length. A signal from the wire capacitively couples to the strip, is discriminated by electronics at the end of an HCAL module, and gives a digital signal representing whether or not the tube was hit. The pattern of tubes gives a two-dimensional track through the HCAL and can be used to identify muons.

Neither of these two signals is used at all in the analysis described here. However, a third one is used in the muon trigger. This signal starts as a pulse on the high voltage supply whenever a streamer occurs in one of the tubes that

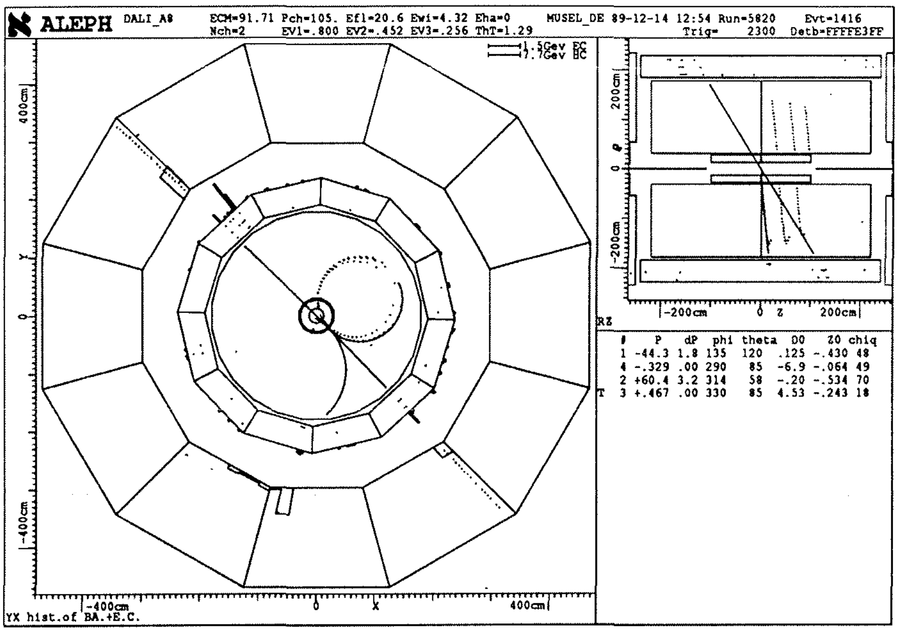

Figure 2.15: An atypical dimuon event in which a radiated photon has converted in the beampipe. Note the pattern of fired strips in the HCAL.

the supply feeds. In the HCAL one high voltage supply feeds all tubes in two adjacent planes of each half-module (barrel or endcap). The signals are coupled capacitively to circuits that combine double-plane signals from each half-module to form full-module double-plane signals. These are then discriminated and for each double-plane firing, a DC level of 200 MV is added to a so called "quasi-analog" output. The voltage level on this output then represents the penetration of particles in the HCAL. More will be said about this signal in the following sections.

2.7 The Luminosity calorimeter

The luminosity in ALEPH is determined by counting the rate of low-angle Bhabha events, The cross section for this process is mainly QED and other electroweak effects, such as $Z^0 - \gamma$ interference, are small. The theoretical uncertainty in the Bhabha cross section 0.7%. The luminosity calorimeter is designed to measure the rate with a systematic uncertainty of less than 2%, so that the measurement of the total visible cross section of the Z^0 is not dominated by the luminosity error. The calorimeter reconstructs shower position and shower energy for Bhabha events. A further use of the luminosity calorimeter in this analysis is the additional hermeticity it provides by extending the electromagnetic calorimeter down to smaller angles to the beam line.

In construction the luminosity calorimeter is very similar to the ECAL. It is a lead-proportional chamber sandwich with projective towers plus wire plane readout and an electronic system identical to the ECAL's, and the gas mixture

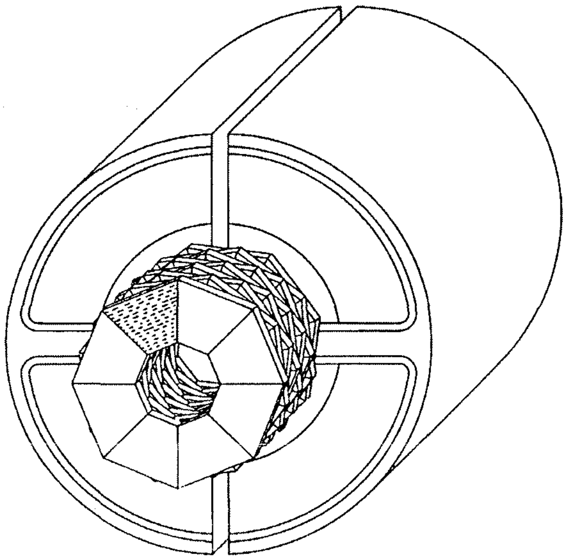

Figure 2.16: The luminosity calorimeter.

is the same. There are 24.6 radiation lengths in the LCAL (the ECAL has only 22), and the energy resolution is comparable, at $20\%/\sqrt{E}$.

The luminosity calorimeter is built in two cylindrical halves (figure 2.16), with each half consisting of two semicircular modules. The angular acceptance is from 45 and 155 mrad, within which the counting rate for Bhabha events is roughly equal to that for Z^0 events. Since the Bhabha cross section is a sensitive function of acceptance, the positions of each tower must be accurately known. In ALEPH the position of each pad relative to other pads in the same layer is known to about 100 μm, and the overall alignment of the subdetector is known to about a millimeter. The precise construction together with the projectivity of the towers permits a reconstruction of the shower position with a resolution $\sigma = 150$ μm.

Using this device one can keep the systematic error on luminosity to 1.7%. The method for determining the luminosity, including the nature of cuts used to separate low-angle Bhabha events from background, is described in reference [17].

A small angle tracking device was installed in front of the luminosity calorimeter; it is shown with the luminosity calorimeter in figure 2.16. It was not used in determining the luminosity, but rather to get an improved understanding of the calorimeter and its alignment. It will not be described here in detail.

2.8 The Trigger

The trigger for ALEPH must distinguish, with high efficiency, "good" physics events from among all the possible backgrounds. The backgrounds include detector noise, cosmic rays, collisions with molecules of beam-gas, a spray of synchrotron radiation, as well as many other possibilities. The trigger does not try to separate out one physics process from another; all Z^0 events are considered worth writing to tape (and the rate is compatible with this), and even the two-photon processes are kept if possible. The trigger is organized into three levels. Level one decides whether or not to read out all detector elements. The level two trigger simply seeks to verify the level one trigger by replacing the ITC tracking information with the more accurate TPC tracking information which is available at 50 μsec after the beam crossing. It was implemented towards the end of the 1989 data set and was used in most of the data analyzed in this report. A level-three software trigger now runs in ALEPH and is used to reject beam-gas and other undesirable events.

The level one trigger relies on special signals from the ITC, ECAL, and HCAL. Each of these detectors is divided into 76 regions in ϕ and in θ, with the segmentation in each subdetector matching that of the other subdetectors. A number of different conditions will result in a level-one YES. These conditions will be a coincidence of different signals on trigger segments of the three subdetectors mentioned above. The trigger is very flexible, and allows for not only programmable thresholds, but also quick reconfiguration of the trigger logic.

Many different triggering conditions were sufficient for a readout of the ALEPH detector. Luminosity triggers required energy deposit in the luminosity calorimeter, and total energy triggers, the main trigger for hadronic decays of the Z^0, depended on energy summed in all modules of the ECAL in barrel or endcaps to exceed a threshold. In order to be sensitive to supersymmetry over the largest range of parameter values we must be sensitive to single particles of low energy. We rely on two triggers in particular, one for single tracks in coincidence with an energy deposit in the wires of a single ECAL module, and a second for single tracks in coincidence with penetration in the HCAL.

2.8.1 The Single Charged Electromagnetic Trigger

The single charged electromagnetic trigger is designed to be sensitive to a single ionizing track that showers in the ECAL. To form this trigger, first the signal is summed separately for even and odd wire planes in each module. These are separately discriminated, then the AND of the two discriminated signals is taken. The resulting logic signal is fanned out to each trigger segment covered by the ECAL module. Finally a coincidence is taken between this signal and the trigger mask delivered from the ITC. In level two, a coincidence is again taken with the TPC mask instead is if the result of the level one decision was YES. Later, one can determine the trigger mask in each segment.

The ECAL threshold corresponds to a 1.3 GeV energy deposit in the wires, which was determined in the following way. For $q\bar{q}$ events (all of which fire the total energy trigger), the energy in the wires of each ECAL module was read out, and then the efficiency with which the discriminator fired for that module was plotted as a function of energy deposit. The energy at which the efficiency is exactly 0.5 is defined as the threshold; and the turn-on is very rapid.

2.8.2 The Single Muon Trigger

The single muon trigger is similar to the single charged electromagnetic trigger except that the ITC trigger mask is taken in coincidence with the "quasi-analog" signal, representing penetration length, from the HCAL. It is possible to determine in which segment the trigger occurred.

For the muon trigger some problems were observed. From Monte Carlo simulation of dimuon events, one expects a single track to fire the trigger in its HCAL segment about 94% of the time, with the inefficiencies coming completely from acceptance. A dimuon event should fire the trigger 100% of the time since one muon falling into a crack is anti-correlated with the opposite muon falling into a crack. Indeed, the magnetic field of ALEPH guarantees that the two muons cannot simultaneously fall into opposite cracks.

On the other hand, the muon trigger efficiency can be measured from the data itself. In a selected sample of dimuon events, one extrapolates each track to the inner boundary of the HCAL to determine which module was hit. Then one looks at the trigger discriminator for that segment. If that track alone was sufficient to fire the trigger, then one includes the other track in the accepted sample. The efficiency for this sample is the single-arm trigger efficiency of the muon trigger for dimuon events. It is shown in figure 2.17 as a function of the number of muons collected (roughly speaking, this is equal to integrated luminosity).

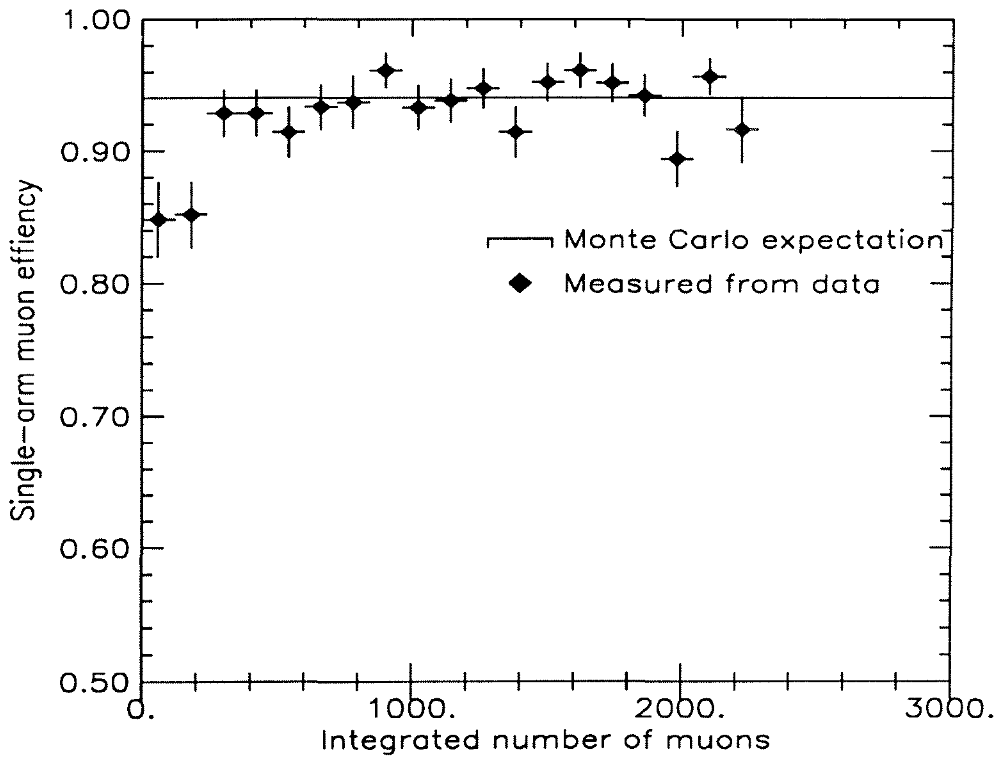

Figure 2.17: Single-arm muon trigger efficiency as measured from the data. Horizontal line is the expected value from Monte Carlo.

The single-arm efficiency was low in the first set of data from LEP, especially in the endcap (only the average of endcap and barrel is shown in figure 2.17). This can be seen by noticing that the first few bins in 2.17 are lower than the value predicted by the Monte Carlo by about 10%. The main source of the inefficiency was that thresholds for discriminating the individual double-planes were too high. The improvement was rapid and soon the efficiency was above 90% for both endcap and barrel, as in Monte Carlo. From these data we estimate that the effect of lower efficiencies on dimuon events is less than .5%. For the supersymmetric signal we will conservatively estimate the effect at 1%.

This same method reveals that the ITC and TPC are 100% efficient on such events.

Chapter 3

Background Processes

3.1 Standard Model Backgrounds

This section describes the in detail the expected background to each signal process, and how they differ from the signal. By far the highest cross section process that occurs in the detector is the decay of Z^0 into multihadron final states, which has been measured at 30 nb at the peak of the Z^0 resonance. The track multiplicity for this is too high for it to be confused with our signals. Other processes which do lead to background are those which leave smaller numbers of charged tracks in the final state. Among these are the processes

- $e^+e^- \longrightarrow e^+e^- (\gamma)$
- $e^+e^- \longrightarrow \mu^+\mu^- (\gamma)$
- $e^+e^- \longrightarrow \tau^+\tau^- (\gamma)$
- $e^+e^- \longrightarrow e^+e^-e^+e^-$
- $e^+e^- \longrightarrow e^+e^-\mu^+\mu^-$
- $e^+e^- \longrightarrow e^+e^-\tau^+\tau^-$

The first process is called Bhabha scattering; the second is called muon pair production, and the third is called tau pair production. In case a gamma ray is present in the final state, these processes are called radiative, for example, radiative muon pair production. The last three processes are known as "two photon" processes, for reasons we will explain. In the following paragraphs we will consider these processes separately.

3.1.1 Radiative Lepton Pair Production

Radiative Bhabha scattering and radiative muon pair production both leave two tracks in the detector. They constitute a background to supersymmetry. In most events the photon energy is small , the momentum of the two tracks balances, and the event topology is two tracks which are very nearly back to back. However in some events the photon energy may be large. When possible one will veto this event by detecting that photon in the electromagnetic calorimeter. Inevitably some of the photons will fall into cracks and escape detection, leaving only two tracks in the final state which are very acolinear, and are "missing" the momentum of the undetected photon. Such events can resemble very closely the supersymmetric processes considered here.

In addition to photons involved in the production process, in Bhabha events an electron can radiate a photon as it passes through the beam pipe, ITC-TPC wall or other matter. The electron track curves away from the photon and its measured momentum is lower than the true momentum.

Radiative tau pair production is a background to our signal whenever two tracks are observed in the final state, that is, when each tau decay leads to one track observable in the final state. The branching ratio for the one-track decays of the tau 86%, so two track final states occur about 70% of the time.

The taus, at LEP energies, are highly relativistic and their decay products, being highly boosted, travel in essentially the same direction as the taus. An energetic photon must accompany the taus if this is not the case, and normally is observed in the detector, as in the above paragraph.

3.1.2 Two-photon processes

These processes probably represent the most severe background, due to their large cross section. Thirty-six diagrams contribute to the $e^+e^-e^+e^-$ final state and twelve contribute to the $e^+e^-\mu^+\mu^-$ and $e^+e^-\tau^+\tau^-$ final states; these may be broken into four classes called multiperipheral, conversion, annihilation, and bremsstrahlung as illustrated in figure 3.1. All graphs contain two virtual photon lines, hence one calls these reactions the "two-photon" or "two-gamma" processes. The most commonly observed topology from events like these is two tracks in the detector, with the additional two tracks escaping though the beam pipe. The largest contribution comes from class a of figure 3.1, the multiperipheral. The cross section depends sensitively on how one defines the acceptance but is roughly .5 nb for electron and muon final states if one requires that at least two tracks be visible inside the detector and have an invariant mass over 2 GeV. For the tau final state it is an order of magnitude less.

To remove this background the first strategy is to look for the low-angle beam particles which are scattered slightly (they are scattered more if the two visible tracks are more energetic) and may be detected either in the electromagnetic or

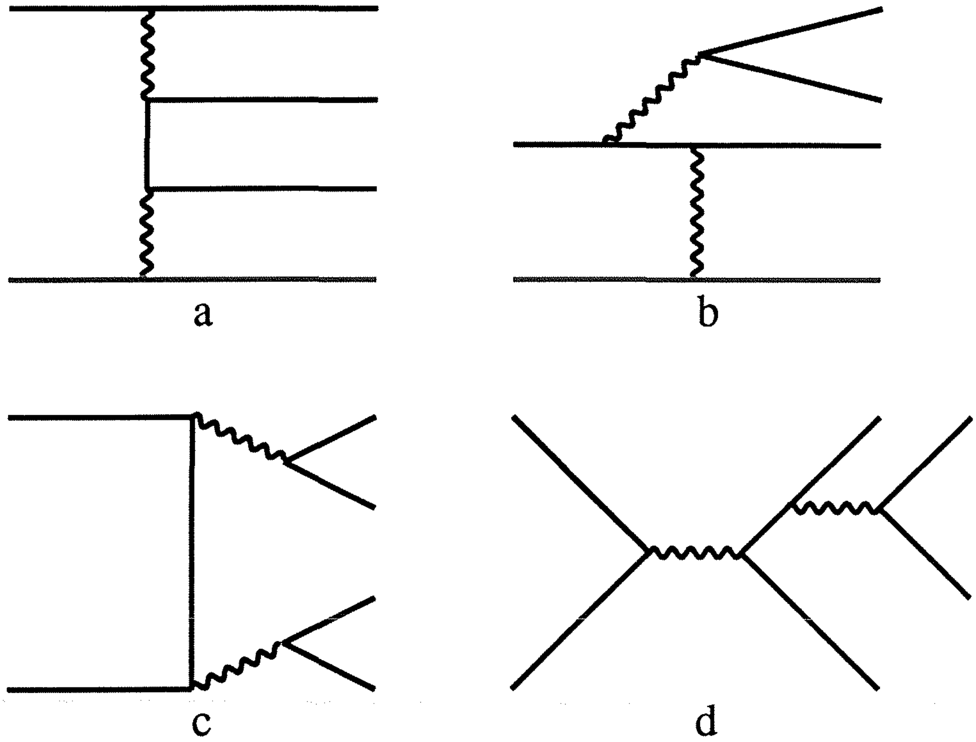

Figure 3.1: Four classes of diagrams contributing to the two-photon process cross sections. a) multiperipheral. b) bremsstrahlung c) conversion d) annihilation

the luminosity calorimeter. The second strategy takes advantage of the fact that when momentum escapes in events such as these, it most commonly escapes in the direction of the beam particles, along the z-axis. This is shown in figure 3.2 which displays an event of the type $e^+e^- \rightarrow e^+e^-e^+e^-$. Viewed in a plane parallel to the beam axis, the two tracks are very acolinear. In the plane perpendicular to the beam axis however momentum appears to balance because the component of lost momentum in this plane is small. We define the *acoplanarity* as the difference between the angle made by the two tracks and 180° when projected into the $x - y$ plane. For two-photon events the acoplanarity peaks at values near 0. In fact for the $Z^0 \rightarrow$ lepton-pairs the acoplanarity is also peaked near 0. Acoplanarity is a useful variable to separate these backgrounds from the supersymmetric signal, as we shall see.

3.1.3 Simulation of the Background

Monte Carlo event generators are used to simulate background from all the above-named sources. For Bhabha scattering the program used is BHAB01 [92,93]. For mu-pair and tau-pair production we use the program KORALZ [94], while for all the two-photon processes we used the program DIAG36 [95] for the generation of the leptonic final states,

The KORALZ program written by Jadach, Ward, and Was, with contributions from Hollik and Stuart is generally considered to be the most complete Monte Carlo for simulating electroweak processes at the Z^0 pole [96]. It includes the effects of multiple hard bremsstrahlung from the initial state and

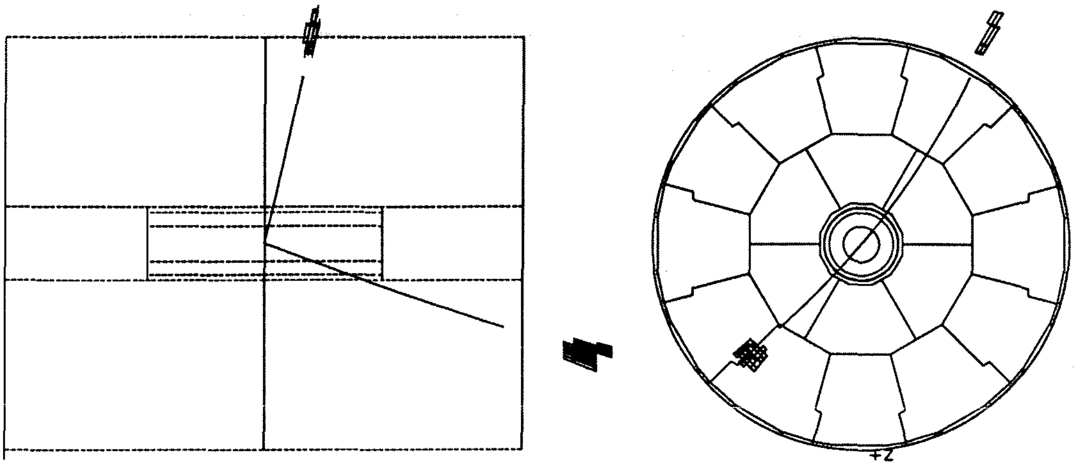

Figure 3.2: A typical $e^+e^- \rightarrow e^+e^-e^+e^-$ event as seen in the ALEPH detector in both side and end views. Charged particle tracks as measured in the TPC and ITC are indicated as lines coming from the center of the detector. The clusters at the end of each track are energy deposits in the ECAL.

single photon bremsstrahlung in the final state, electroweak radiative corrections, spin-polarization effects in the decay of the tau, as well as single photon bremsstrahlung. The systematic uncertainty in cross section and A_{FB} from this program is less than 1%.

For Bhabha scattering at large angles, no existing generator available today approaches the accuracy of KORALZ. The generator BABAMC includes s- and t- channel photon and Z^0 exchange, and all first-order QED corrections. It's main limitations are the lack of multiple photons or QCD corrections to the Z^0 width. In the absence of correct calculations including these effects, it is difficult to estimate the accuracy of this generator. It is felt to be accurate to a few percent.

The electroweak generators KORALZ and BHAB01 are provided with the measured resonant parameters of the Z^0, namely, a Z^0 mass of 91.170 GeV. A standard model electroweak library calculates the width and the Weinberg angle and gives values close to the measured value of 2.50 GeV and .229. We do not consider a change in the background characteristics due the the presence of a supersymmetric partner, which could, for example, broaden the width of the Z^0.

The two-photon event generator DIAG36 written by Behrends, Daverveldt, and Kleiss is a complete QED calculation of the four-lepton final states to order α^2. For the four electron final states, thirty-six diagrams contribute to the cross section, but the dominant diagrams for the no-tag configuration are in the subset of twelve leading to the $ee\mu\mu$ final state. We therefore simulate only these diagrams.

The contribution to the cross section from the multiperipheral diagrams becomes very large as the invariant mass of the multiperipheral pair becomes small. Therefore we have put a cut on the minimum value that this mass can have, at the generator level, of 4 GeV^2 In addition, the visible pair must have $E_1, E_2 \geq 1.0$ GeV. In the data analysis described subsequently we impose slightly more severe cuts than those imposed at the generator level to avoid the region in which this background was not simulated. In addition for efficiency we do not generate events unless at least two tracks make a sufficiently large angle with the beam direction to be detected in the TPC.

The two-photon events containing hadrons in the final state were also simulated at an early stage using the event generator PHOT01 [97,98,99], and it was found that they contributed less than 1% to the selected events (for the exact nature of the selection, see the next chapter). Therefore we do not simulate these events since this is a very time-consuming process.

Each process was simulated at each of the LEP scan energies, in an amount roughly proportional to the luminosity that LEP collected at that point. Each Monte Carlo event is then weighted by the ratio of collected luminosity to generated luminosity. A total of 15 pb^{-1} of background is generated, which compares favorably to the LEP integrated luminosity of 2.45 pb^{-1}.

The importance of generating at each of the different LEP energies is due to several facts. First and most obvious is the rapid change in cross section across the Z^0 resonance. As the beam energy is changed, the number of mu and tau pair events follows one resonance curve, the high-angle bhabha scattering follows a very different one, and the two-photon processes change only logarithmically with energy. Moreover, the angular distributions change. For mu and tau this is because of the energy dependence of the A_{FB}, while for Bhabhas it arises because the interference term between t-channel γ exchange and s-channel Z^0 exchange depends sensitively on energy, changing sign above and below resonance. The rate of hard photon radiation changes with energy as well (it is higher above the resonance). Finally the energies of the dileptons vary with beam energy.

The response of the detector is simulated using the most complete simulation of the ALEPH detector (GALEPH). We will mention here only the most important features of the simulation. A detailed description of the ALEPH geometry is included. Electron ionization, drift, and multiplication in the TPC are simulated in detail. GEANT3 is used for particle tracking, and the GEISHA package is used to simulate hadronic showers. For electromagnetic showers a parametrization is used, based on the both the Monte Carlo EGS IV and test-beam results. Trigger thresholds used in the Monte Carlo are those measured from the data.

The simulation produces output in the same form as the ALEPH online data acquisition system. One then uses the identical reconstruction program (JULIA) on the Monte Carlo as is applied to the data.

Chapter 4

Analysis of Two-track Events and Search for Supersymmetry

This chapter is organized in two sections. In the first section we shall discuss the cuts used to isolate a supersymmetric signal, described in chapter 1, from the background, described in chapter 3. We also discuss the result of applying these cuts to a sample of data in ALEPH collected during fall of 1989 and the spring of 1990, representing 2.45 pb^{-1} of integrated luminosity distributed on and around the Z^0 peak. In the second section we discuss the interpretation of the result in terms of limits on selectron, smuon, stau, and chargino.

4.1 Selection of Two-track events and Separation of the Signal from Background

Using a series of cuts on kinematic variables (to be described) it is possible to make a clean separation between the background processes and a hypothetical signal from the supersymmetric processes for which we are searching. However tails on the distributions from the background make it difficult to reject the background to the 100% level if one is to remain sensitive to the signal over the interesting part of the parameter space. The final limit obtained will be depend on the number of events expected to pass the cuts from background processes alone. Thus an accurate estimation of this number is crucial for a correct limit. We therefore generate a very large amount of Monte Carlo simulated events (roughly six times as many as data events and distributed in energy in the same way).

In this section we first describe a preliminary set of cuts which selects all two-track events from the sample of Z^0 decays and other QED processes. The resulting sample is then used to compare with Monte Carlo simulated events and verify that the detector and that background is well simulated. After this we show a final set of cuts which can be used to separate the signal from the background.

4.1.1 Selection Criteria

A good track is defined as a track reconstructed from at least five TPC coordinates and lying within a fiducial region defined by $|\cos\theta| < 0.95$, where θ is the angle between the track and the beam axis at the interaction point. In addition the track must be consistent with the vertex position (to eliminate cosmic rays and beam-gas interactions). The criteria is as follows: let d_0 be the distance of closest approach to the beam line and let z_0 be the distance along z from the vertex at d_0. We require $|d_0| < 3.0$cm and $|z_0| < 7.0$cm.

The basic selection criteria are:

1. Two and only two tracks in the final state, both must be "good".

2. $E_{ECAL} < 5.0$ GeV.

3. $E_{LCAL} < 5.0$ GeV.

where E_{ECAL} is the energy of each electromagnetic calorimeter cluster unassociated with charged tracks and E_{LCAL} is the total energy on the wire planes of each luminosity calorimeter. Cut 1 is the basic selection criteria for the inclusive two-track sample. Cut 2 excludes radiative Bhabha, μ-pair, and τ-pair events in which an energetic photon has been detected in the calorimeter. Cut 3 also serves this purpose, but in addition excludes the two-photon events in which the beam particle has scattered into the luminosity calorimeter and deposited some energy there.

Noise in the electromagnetic calorimeter present in our data sample causes a random loss of events due to cut 2. We can estimate this loss by studying the energies of clusters in randomly-triggered readout of the ALEPH detector. The distribution of the highest energy ECAL object in each event is shown in figure 4.1. This noise would be superimposed over any other activity in the detector; if the highest energy cluster were above 5 GeV the event would be killed. We find that 1% of the random triggers have clusters above 5 GeV. We reduce the Monte Carlo simulation of the background by this 1% (by changing the weight of each event) and we also reduce the rate of our supersymmetric signal by the same amount.

We place two other cuts on the data to insure that the comparison with Monte Carlo simulation is justified. First, we require each good track to have an energy of at least 2 GeV. This is so that our muons penetrate the HCAL sufficiently so that the checks of the single muon trigger simulation performed

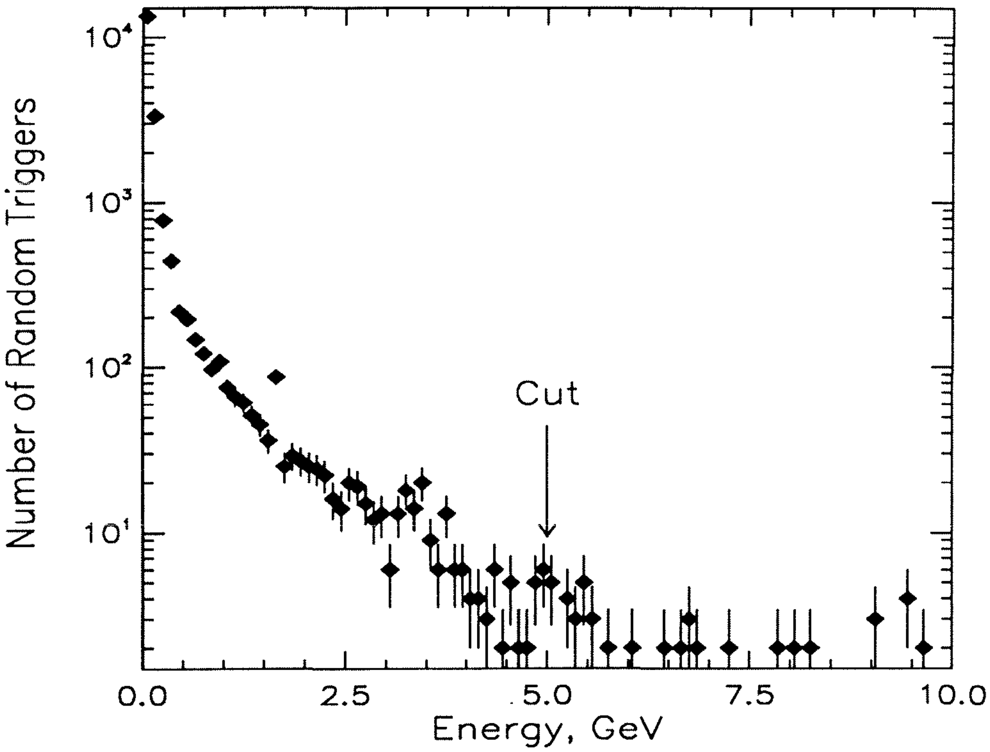

Figure 4.1: Most Energetic ECAL cluster in a sample of random triggers. From this distribution we derive the rate at which random noise in ECAL may veto SUSY events

with dimuons (section 2.8.2) apply as well to muons tracks at our energies. For electrons the 2 GeV cut is well above the calorimetric threshhold of 1.3 GeV, and also well above the track momentum of 1 GeV at which the ITC loses efficiency for triggering due to track curvature. Finally, we avoid the region below 1.0 GeV where the two-photon events were not generated.

We further require the invariant m^2 of the two visible tracks to be greater than 5 GeV. This is because in the simulation the two-photon events were not generated below $m^2 = 4$ GeV^2.

The data passing these preliminary selection criteria can be compared with our sample of Monte Carlo simulated events. Figures 4.2 and 4.3 show the energy and angular distributions of the simulated standard model backgrounds with the observed data overlaid. The TPC momentum distribution shows a low energy peak from the two-gamma events and a high energy peak from Bhabha and μ-pair production. Between these two peaks lie mostly τ-pair events. The agreement is very good, except for a small difference of resolution of the Bhabha and μ-pair peak.

The $\cos\theta$ distribution also agrees very well with the simulation both in shape and normalization. The peak in the forward direction is due to the Bhabha events with mainly the t-channel photon exchange graph and the $Z^0 - \gamma$ interference term contributing there.

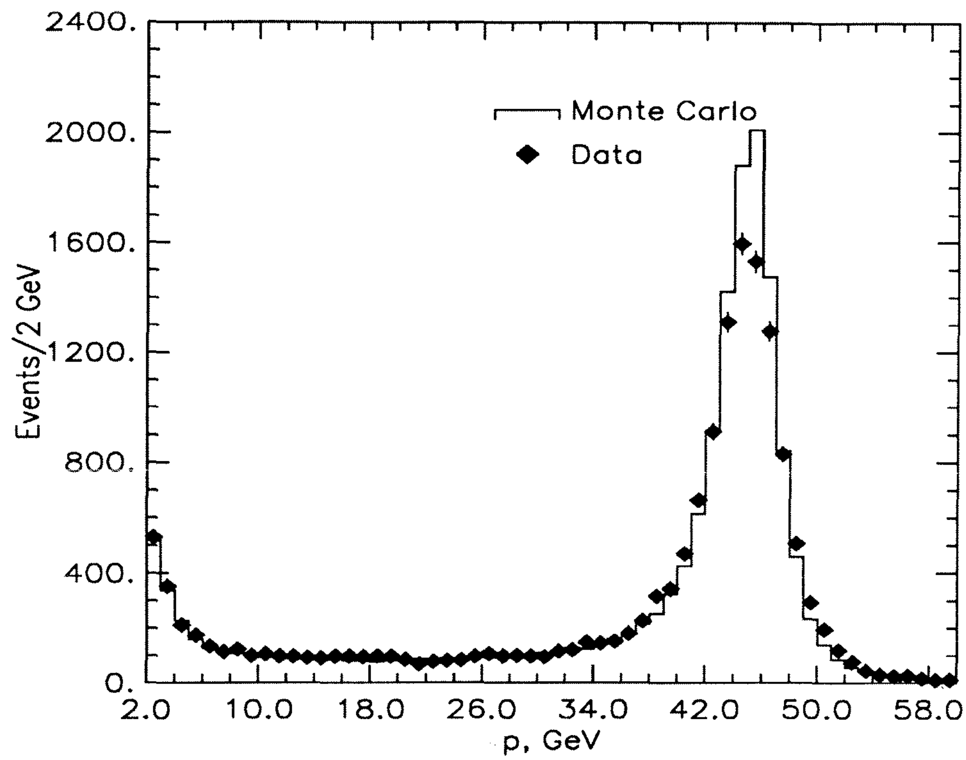

Figure 4.2: Measured track momentum for all tracks in the sample of two-track events. Monte Carlo simulation compared to data (dots).

4.1.2 Further Cuts to Separate the SUSY Signal from the Standard Model Backgrounds

The acoplanarity has already been defined as the difference in angle between the two tracks as seen in the $r - \phi$ plane, and 180°. We define the "missing energy" as $E_{CMS} - p_1 - p_2$ where E_{CMS} is the centre-of-mass energy of the e^+e^- initial state and p_1 and p_2 are the track momenta as measured in the TPC and ITC. These two variables are effective in separating our hypothetical signal from the

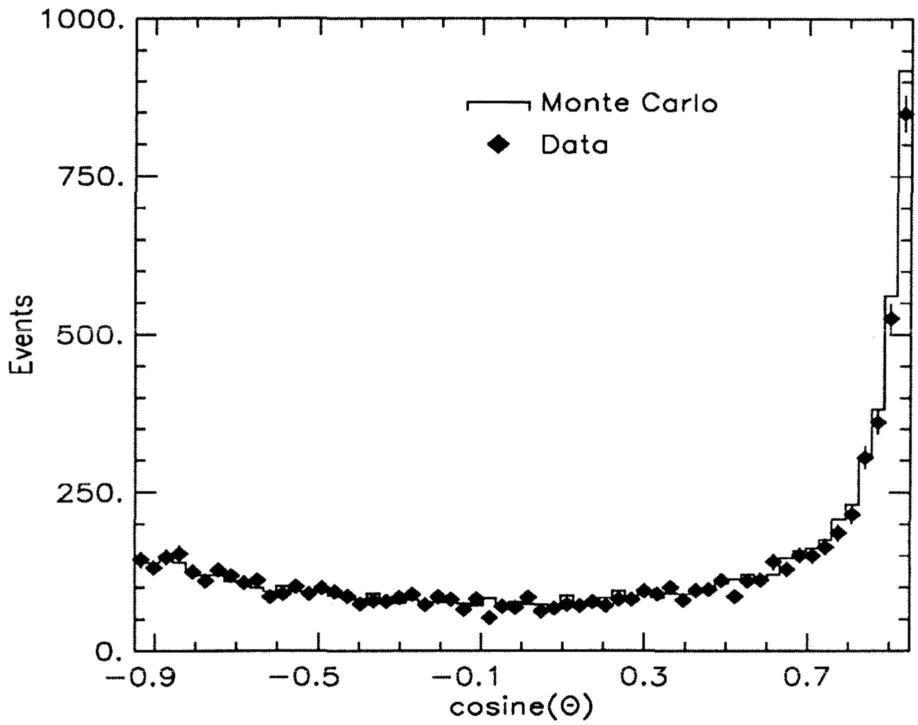

Figure 4.3: $\cos\theta$ for the sample of two-track events as described in the text. Monte Carlo simulation is compared to data (dots).

background. We have plotted the distribution in these two variables for the data in figure 4.4a and for a simulated selectron signal with a selectron mass of 32.0 GeV and photino mass of 15.0 GeV in figure 4.4b. Most of the data cluster at acoplanarity values near 0; the exception is a handful of events in which nearly the entire event energy is missing (mainly two photon events in which the beam electrons have hardly scattered). We choose our cuts as

- Missing Energy < 80.0 GeV

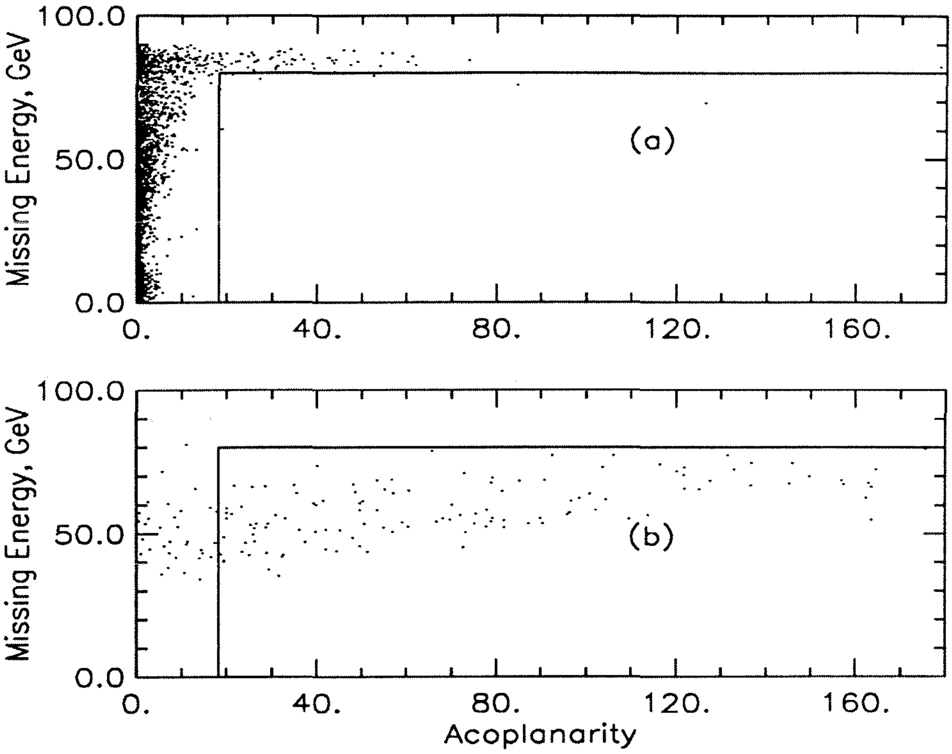

Figure 4.4: Missing energy vs. acoplanarity a) from the data sample, and b) from simulation of a 32.0 GeV selectron with a 15.0 GeV photino. The lines indicate cuts used to separate signal from standard model background.

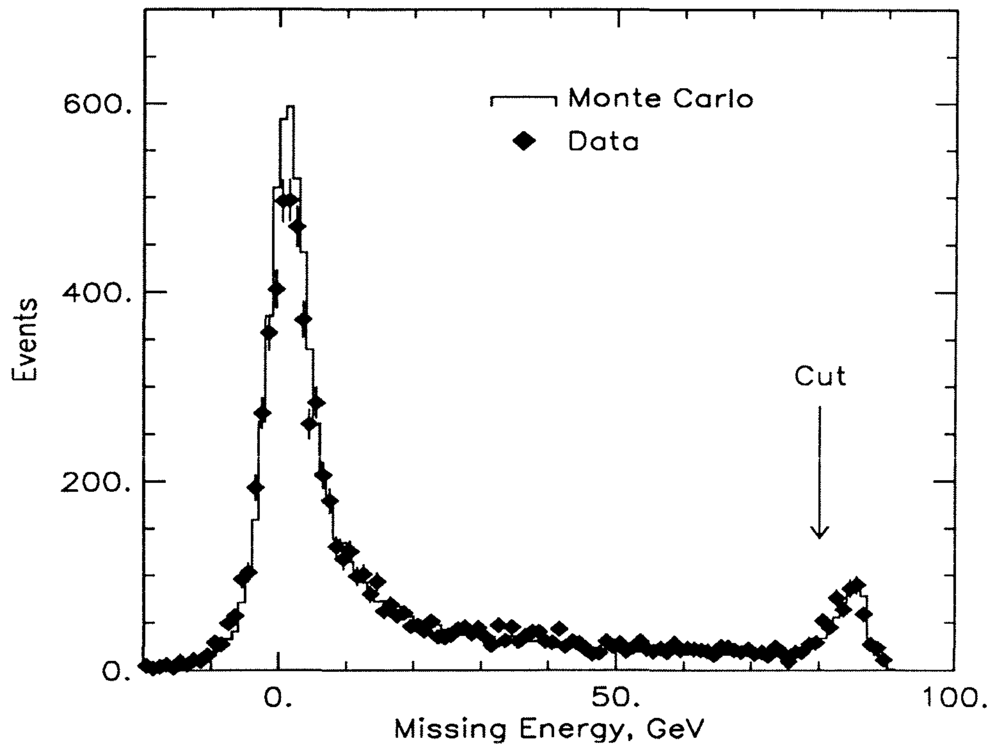

Figure 4.5: Missing energy distribution for data and Monte Carlo simulation.

- cos (Acoplanarity) $<$ .95 (Acoplanarity $< 18.2^\circ$)

The data agrees very well with the Monte Carlo simulation as can be seen by projecting the distribution of figure 4.4a onto either axis and comparing. Figure 4.5 shows the missing energy distribution. Here one can clearly see two peaks, one due to the Bhabha and μ-pair events, the other from the two-photon events. The distributions agree in shape and normalization. The acoplanarity distribution is shown in figure 4.6. One observes good agreement over many orders of magnitude.

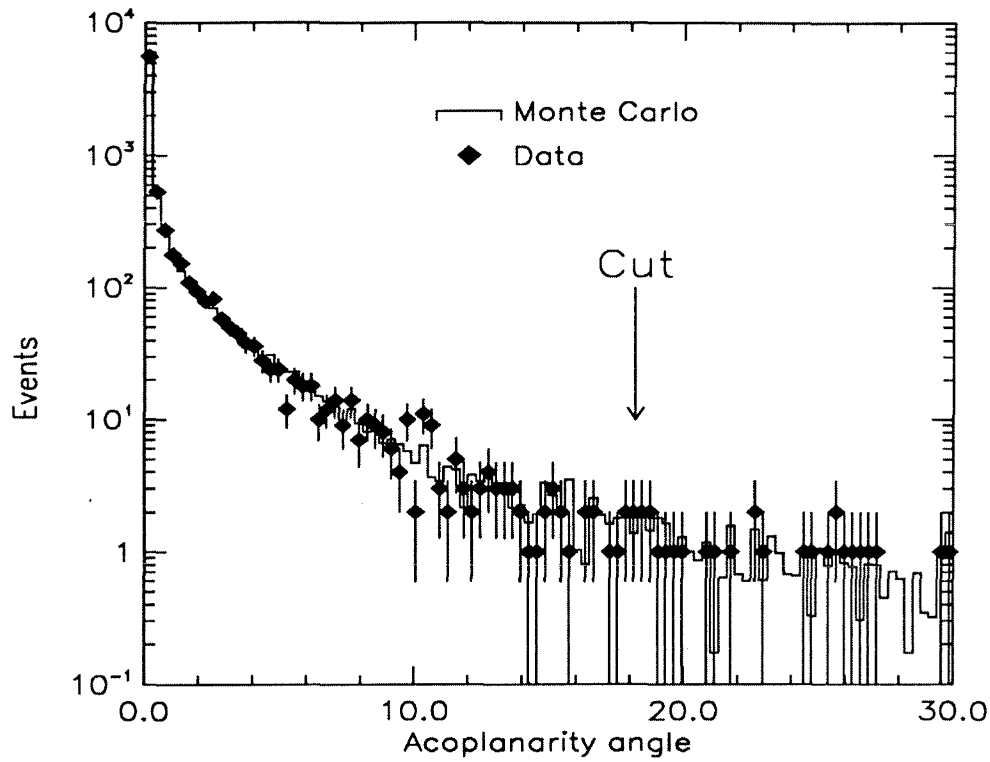

Figure 4.6: Acoplanarity distribution for data and Monte Carlo simulation.

E_{cms} (GeV)	$\int \mathcal{L}$ (pb)
88.3	.211
89.3	.163
90.3	.191
91.3	1.40
92.3	.175
93.3	.167
94.3	.128
95.3	.016

Table 4.1: Data was collected at eight different center of mass energies at LEP. This table gives the amount of integrated luminosity was collected over each data point.

4.1.3 Signal Rate and Efficiencies

The cross sections and efficiencies through the cuts described above vary with the nature of the signal–selectron, smuon, stau, or chargino – and with the mass of the charged state as well as the photino mass. The total luminosity, measured from low-angle Bhabha events as described in reference [100], of 2.45 pb^{-1} is used to obtain the total expected number of events for each process; this luminosity is taken at several center-of-mass energies as shown in table 4.1.3. The efficiency and expected number of events is exhibited in the tables 4.2 - 4.5. In each of these tables the cross section given is not the peak cross section, but a weighted average of the cross section at each energy point at which data was collected.

For selectrons(table 4.2) and smuons (table 4.3) the 100% branching ratio of the final state into two electrons or two muons leads to generally high detection efficiencies; the smuon efficiency is slightly higher that of the electron since bremsstrahlung in the detector material is lower.

$M_{\tilde{e}}$ (GeV)	$M_{\tilde{\gamma}}$ (GeV)	$<\sigma>$ (pb)	Efficiency	# Events
40.0	30.0	61	.66	99
40.0	20.0	62	.67	100
40.0	10.0	61	.65	98
30.0	20.0	240	.61	400
30.0	10.0	250	.64	390
20.0	10.0	430	.52	550

Table 4.2: Selectron cross section and detection efficiency

$M_{\tilde{\mu}}$ (GeV)	$M_{\tilde{\gamma}}$ (GeV)	$<\sigma>$ (pb)	Efficiency	# Events
40.0	30.0	54	.74	98
40.0	20.0	54	.77	100
40.0	10.0	54	.78	100
30.0	20.0	210	.68	350
30.0	10.0	210	.73	380
20.0	10.0	360	.59	530

Table 4.3: Smuon cross section and detection efficiency

For both selectron and smuon, the efficiency through the cuts decreases, as the photino mass approaches the slepton mass. This is both due to more back-to-back decay topologies and due to less energetic tracks. As the slepton mass approaches the beam energy, the rate falls off due to the decreased cross section (shown here are for a degenerate pair of left- and right- handed sleptons). Cross sections for selectrons are higher than those for for smuons because of the contribution of t-channel diagrams as discussed in chapter 1.

The efficiency for stau final states (4.3) is lower than that of smuon final states for three reasons. First, a pair of taus decays leaving two tracks in the final state about 70% of the time. Secondly, additional photons sometimes accompany the stau decays, and can cause a veto of the event. And third, the average energy

$M_{\tilde{\tau}}$ (GeV)	$M_{\tilde{\gamma}}$ (GeV)	$<\sigma>$ (pb)	Efficiency	# Events
40.0	30.0	54	.035	4.7
40.0	20.0	54	.15	20
40.0	10.0	54	.18	24
30.0	20.0	210	.071	37
30.0	10.0	210	.120	63
20.0	10.0	360	.085	76

Table 4.4: Stau cross section and detection efficiency

$M_{\tilde{W}}$ (GeV)	$M_{\tilde{\gamma}}(GeV)$	$<\sigma>$ (pb)	Efficiency	# Events
40.0	30.0	8000	.013	260
40.0	20.0	8000	.047	920
40.0	10.0	8000	.055	1100
30.0	20.0	12000	.023	660
30.0	10.0	12000	.041	1200
20.0	10.0	13000	.026	830

Table 4.5: Chargino cross section and detection efficiency

of stau events is smaller than that of selectron or smuon events because there at least two additional neutrinos present in the decay. The detection efficiency for several masses is tabulated in Table 4.3.

The detection efficiency of the chargino is low because we are sensitive only to the leptonic decay modes (muon or electron or taus which decay into a single prong). However, the enormous cross section for chargino pair production allows us to tolerate low efficiency while still obtaining good limits. The cross sections shown in table 4.1.3 are calculated for a pure Wino; for a pure Higgsino they are lower by about an order of magnitude.

One sees from these tables that number of expected events through the cuts depends on the mass of the charged supersymmetric partner mainly through the cross section, while it depends on the photino mass mainly through the detection efficiency.

4.1.4 Effect of the Cuts on the Data and Background Monte Carlo Simulation

Before cuts, one observes 7573 events in the data sample and one expects 7808.4 events from Monte Carlo simulation. After the acoplanarity cut, 67 events survive in the data, whereas one expects 66.3 events from the simulation. The cut on missing energy reduces the number of surviving events to 8, and reduces the expectation to 11.7 ± 1.2 events. The near equivalence of the observed number of events with the expected observed number of events after each cut gives us confidence that the physics is well modelled by standard physics, even on the tails of our distributions.

No event is rejected on the basis of any additional requirement, for example, by visually scanning the events.

We interpret this result as a negative result on new additional signal which would provide us with perhaps hundreds more additional events satisfying our cuts. Well-known methods [101] allow us to interpret this in terms of a 95% confidence level limit on additional signal; the exact meaning, formula, and derivation is given in Appendix A. Before calculating the 95% Poisson confidence level limit, however, we reduce the expected background by one standard deviation before applying it in the formula, to derive a more conservative limit. In addition we reduce the expected background by 10% to allow for possible systematic errors in the simulation of the standard model backgrounds. Finally we calculate the 95% confidence level limit of 6.79 events obtained from observing 8 events in the data when 9.3 are expected from standard model backgrounds.

What do the background events come from? The Monte Carlo simulation leads us to expect that about 1/2 of the surviving events should be from radiative Bhabhas, mu-pair and tau-pair events, with the remaining 1/2 coming from two-photon processes.

4.2 Mass Limits

As discussed earlier, the cross section and efficiency for each signal process depend on the mass of the charged superpartner and on the photino mass. Our goal is to determine the region in the space of these two parameters which is excluded to 95% confidence by the previous result. One way of doing this is to fully simulate the the signal at many points in the two-dimensional parameter space until the efficiency for detecting the signal is known as a function of both masses.

One is tempted, because of the simplicity of the final states considered here, to take a different approach. In this approach, the physics of production and decay is fully simulated using the Monte Carlo programs described in the first chapter. The response of the detector to the two tracks in the event and to a possible initial state photon is determined by fully simulating its response to individual particles (electrons, muons, pions, and photons). Then the probability for fully reconstructing a given event is found by "factorizing" the event into two tracks, and finding the probability that each track is recognized as a single charged track containing no extra photons. The trigger efficiency can also be accomodated, since the event will trigger the apparatus if either track triggers fires the single muon or the single charged electromagnetic trigger conditions. This approach is justified on the basis that reconstruction efficiencies ought to be uncorrelated, while correlation in trigger efficiencies–for example, if two tracks strike the same trigger segment–can only increase the trigger efficiency.

Finally, the effect of cuts applied to the data can be simulated by applying them directly to variables at the generator level. This approximation ignores smearing in both the missing energy and the acoplanarity distribution. Smearing in the acoplanarity distribution is very small and can be ignored. Smearing in the missing energy distribution causes us to underestimate the efficiency and is conservative. Figure 4.7 shows why, using selectron pairs as an example. For slepton pairs, the missing energy distribution has a triangular shape (this is because it is related to the sum of two variables with flat distributions, namely p_1 and p_2, as discussed in Appendix B). Near the edge of the excluded region only the lower part of the missing energy extends down to the cut at 80.0 GeV. The effect of detector smearing is to broaden this distribution so that more events pass the cuts. Thus, to ignore the smearing is slightly to underestimate the detection efficiency.

For electrons, a further effect which needs to be accounted for is a slight degradation in energy as the electron traverses the detector material. This degradation, due to the emission of low energy photons, varies little with electron energy and is about 6%. We take it into account by decreasing the energy of electrons by the same amount prior to calculating the missing energy.

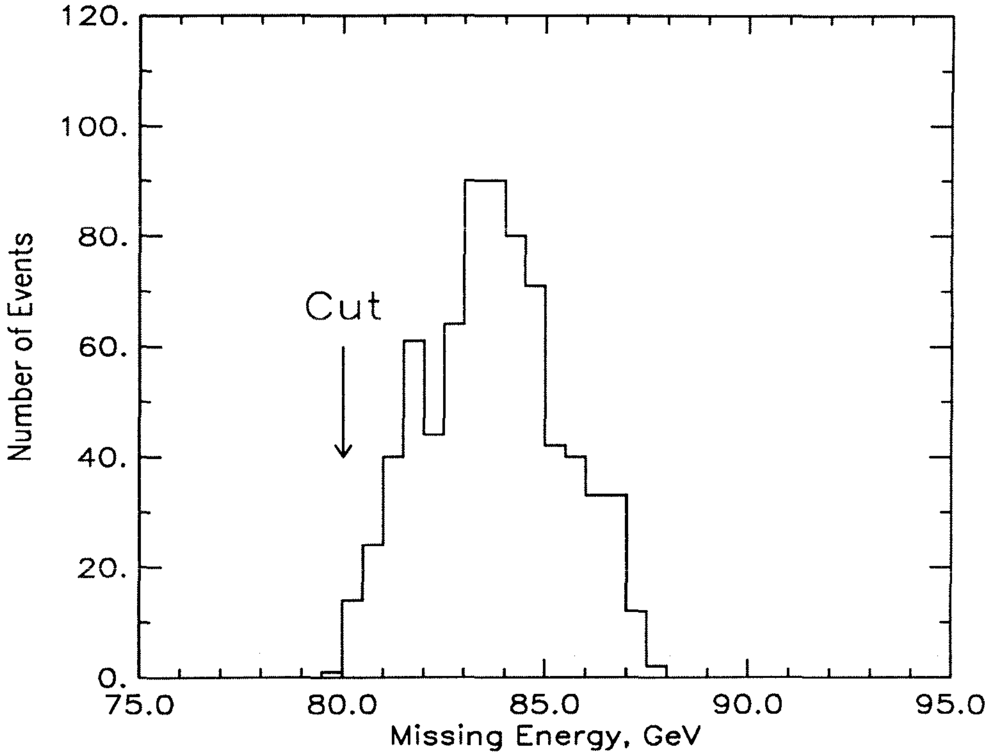

Figure 4.7: Missing energy distribution from a simulated selectron signal near the border of the region to be excluded. Detector smearing broadens this distribution causes more events to pass the cuts.

Trigger and reconstruction efficiencies are calculated separately for each species of particle that we consider–pion, muon, electron, and photon. 10,000 of each species are generated uniformly in θ and in $\log(E)$ where θ is the angle that the particles' momentum makes with the beam axis and E is the the particle's energy. This distribution emphasizes lower energies and angles, where reconstruction and trigger efficiencies change most rapidly. The results are tabulated as a look-up table in which reconstruction efficiencies and trigger efficiencies can be found as a function of E and θ.

Plot 4.8 shows for example the the efficiency with which electrons are reconstructed as a function of energy and of angle with respect to the beam axis. Similar plots obtain for muon, pion, and photon. Trigger efficiencies are tabulated in the same way.

From these maps we compute the efficiency to detect a simulated event from the efficiency for triggering and recognizing the two tracks. The event efficiency is equal to the probability of triggering on track #1 OR track #2 AND the probability of recognizing track #1 AND track #2.

We have checked this by comparing this method of simulating the data with the full detector simulation. On 1000 selectron events, 786 were estimated to satisfy the basic selection criteria using the full detector simulation, versus 788 when the fast simulation was used. 679 of these were estimated to pass the cuts using the full simulation, while 672 were estimated to pass the cuts using the fast simulation. Thus the two methods agree rather within about a percent.

The boundary of the excluded region is found by choosing different mass points within the parameter space, fully simulating the the pair production and

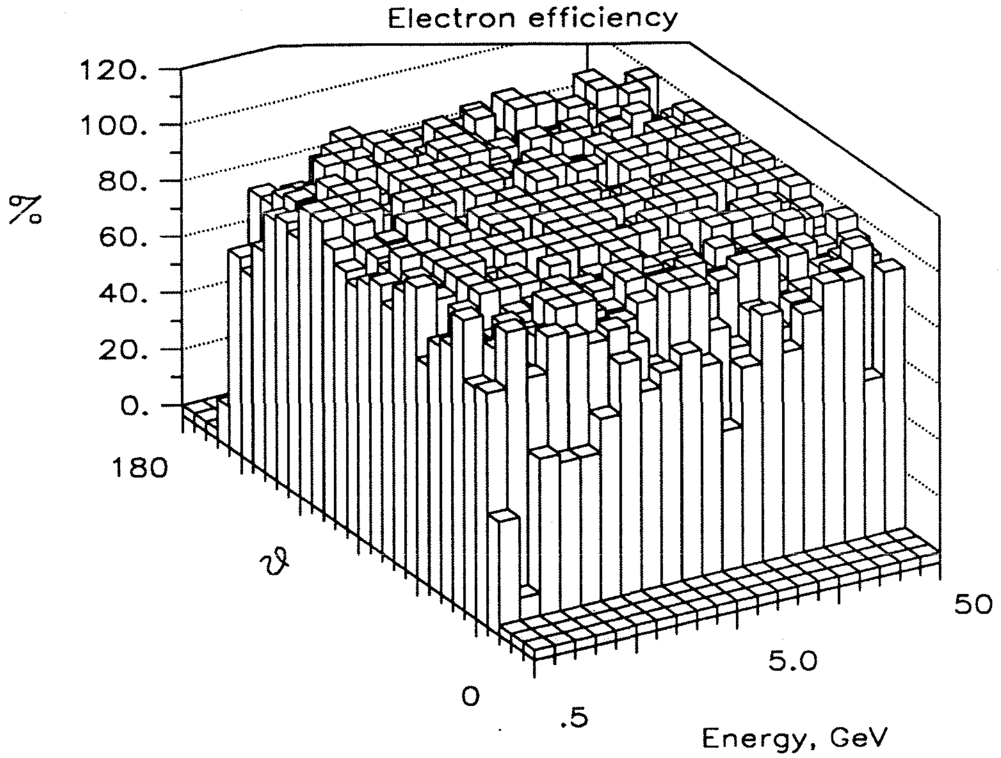

Figure 4.8: Efficiency map for detection of electrons. The vertical scale shows the efficiency to be recognized as a single track, as a function of energy and angle with respect to the beam pipe.

decay of the signal at each point, and using the fast method of estimating the surviving number of events at each point by the above method. One can thus decide rather rapidly whether or not a point in the mass space is excluded without performing vast amounts of calculation. At the same time, the simulation of the detector has not been altogether dispensed with, as it enters in the prior step of calculating the single-particle efficiencies.

4.2.1 Systematic Errors on Expected Signal Rate

We now turn to the question of systematic errors. Namely, what sources of error could reduce our signal or our ability to observe it from its expected value? We consider separately the following sources of systematic error: luminosity error, error in the production cross section, error from the trigger, and error due to the fast method of calculating the boundary. When we have accounted for all these errors, we combine them and reduce the calculated number of events by this amount.

The error in the luminosity for the included runs has been calculated at 1.3%. The interested reader is referred to reference [100] for an explanation of how the luminosity is measured and how the systematic errors are carefully controlled and estimated.

The error in the cross section can come from several sources. A large effect comes from QED radiative corrections to the Born cross section. Our approach has been to include first-order radiative corrections, but to ignore second and higher order corrections. Since second order radiative corrections are known to raise the cross section at the Z^0 peak, the neglect of these terms is already pessimistic and we do not include it in the systematic error.

On the other hand, one could imagine that other diagrams contribute to the production cross section: for example, in the case of selectron pair production, the exchange of other neutralino states. If such diagrams interfere destructively with the Z^0, they can decrease the production cross section. Since we do not know the SUSY particle spectrum, about all we can say about these particles is that they should couple with strengths typical of the electroweak interaction. In general the importance of these diagrams is far less than that of the Z^0 since only the Z^0 will be resonance-enhanced at the energies considered here.

To calculate the approximate size of contributions like this, consider the photon interfering with the Z^0. At the peak, the interference term vanishes since the s-channel Z^0 exchange diagram is purely imaginary while the photon term is purely real. Within the energy range of this analysis (88.28 GeV - 94.04 GeV), the interference term is always less than 4% and has an average absolute value of less than 1% (for sleptons). Moreover the photon diagram (more generally any diagram whose amplitude is real) to interfere with the Z^0 either destructively above the peak and constructively below the peak or vice-versa. Thus in experiments collecting equal amounts of data above and below the peak, cancellation occurs. Considering these facts, we estimate a systematic error on the production cross section of 1.5%.

Checks performed on the trigger, described in chapter 2, show a slight inefficiencies in the single muon trigger in the early period of 1989. They cause an

$M_{\tilde{e}}$	$M_{\tilde{\gamma}}$	ε, full simulation	ε, fast simulation
40.0	35.0	0.4 %	0.0 %
35.0	30.0	7.9 %	7.9 %
30.0	25.0	20.1 %	20.8 %

Table 4.6: Signal efficiencies calculated with both full and fast simulations for three mass point near the boundary of the the excluded region for selectrons.

inefficiency on events containing muons not exceeding 1%. We take 1% as the systematic error due to triggering.

Finally, we have compared the fast method of estimating the number of events (from a sample of 1000) surviving the cuts with the full Monte Carlo simulation of the ALEPH detector at three mass points near the boundary of the excluded region (this will be discussed in the next section). The results are shown in table 4.2.1, agree very closely, and are consistent within errors. This extend the checks performed on the fast method to the region of the parameter space near to the border. We therefore say that the this method overestimates the efficiencies by no more that 5%.

Combining these errors linearly, we find a total systematic error on the number of events expected to survive cuts of 1.3%(Luminosity) + 1.5%(Cross section) + 1%(Trigger) + 5%(Fast simulation) = 8.8%(overall).

We now discuss the results. In each case the number of observed particles has been reduced by the systematic error of 9% as described in the last section, plus the 1% random loss of events due to the noisy ECAL has also been taken into consideration.

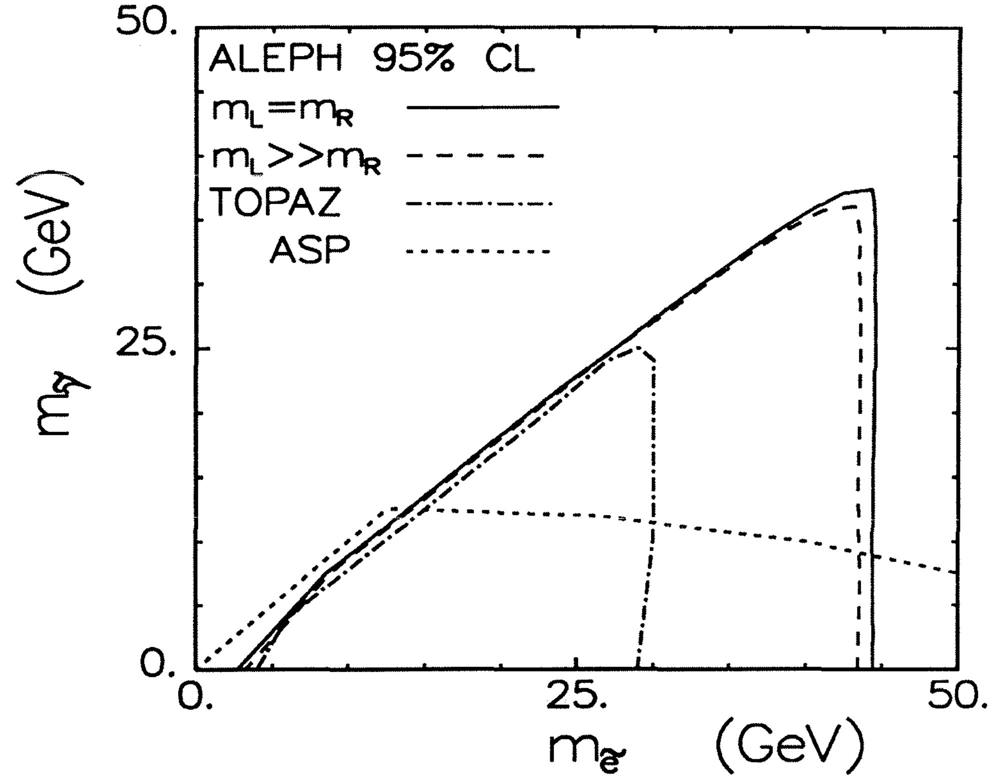

Figure 4.9: Mass limit for $\tilde{e}$.

4.2.2 Selectron, Smuon, and Stau

The result for selectrons is shown in figure 4.9, for two different cases. The best limit obtains for degenerate $\tilde{e}_R$ and $\tilde{e}_L$, for then each state makes a contribution to the cross section. We can exclude $\tilde{e}$'s up to a mass of 44.5 GeV in this case, as indicated by the solid line in the graph. If now we assume that the $\tilde{e}_L$ is much more massive than $\tilde{e}_R$ (so that only $\tilde{e}_R$, the state with the weaker coupling, is produced), then we can rule out this selectron to a mass of 43.5 GeV. Also shown in figure 4.9 are existing limits from previous experiment. TOPAZ rules out the degenerate-mass selectron to nearly 30 GeV. The ASP limit, based on the channel $e^+e^- \rightarrow \tilde{e}\tilde{\gamma}\gamma$ rules out the selectron to about 60 GeV, however the limit can be avoided for a heavier photino.

For smuons the excluded region is similar. For a light photino it extends to 44.2 GeV for degenerate $\tilde{\mu}$ and 43.7 GeV for only $\tilde{\mu}_R$ (see figure 4.10). This extends the TOPAZ limit of about 25 GeV for degenerate-mass $\tilde{\mu}$.

The stau limit, figure 4.11 is weaker for reasons already discussed. In obtaining this limit we estimate the efficiency using all events in which contain only leptonic or hadronic tracks and no photons above 5 GeV. For a light photino, the limit is 43.2 GeV in the degenerate case and 41.0 GeV in the non-degenerate case.

4.2.3 The Chargino

Like the sleptons, $\tilde{\chi}^{\pm}$ production depends on the mass, and the photino mass may affect detection efficiency by changing the decay distributions of the $\tilde{\chi}^{\pm}$. The other parameter which may affect the number of signal events is the relative

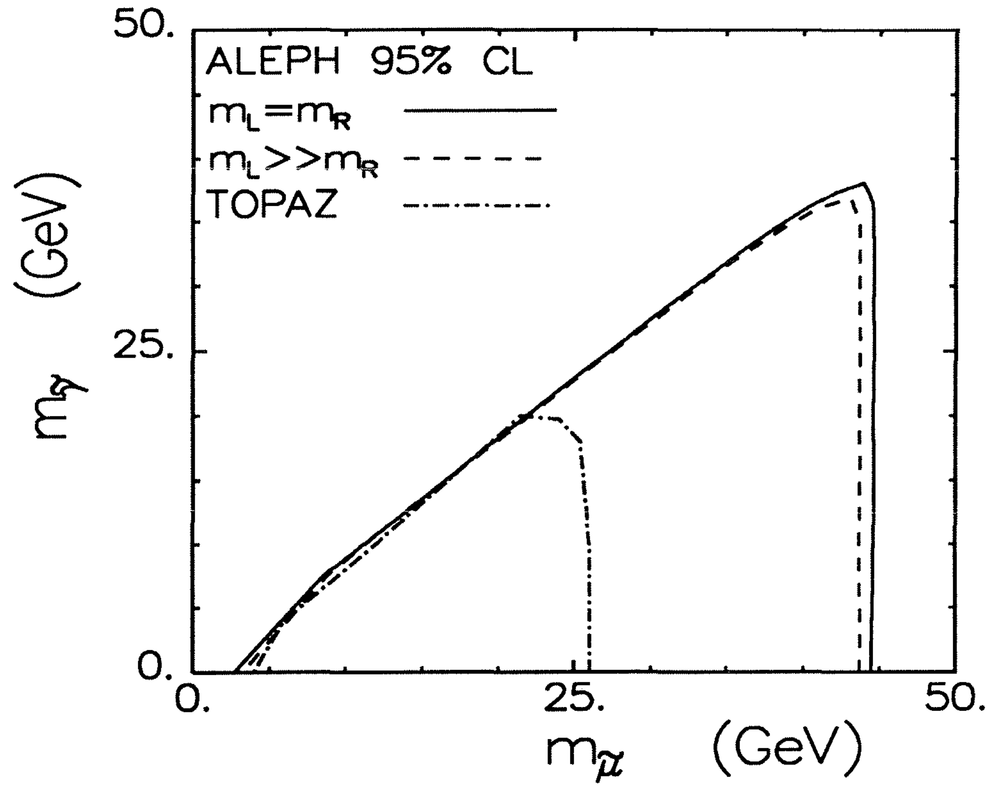

Figure 4.10: Mass limit for $\tilde{\mu}$.

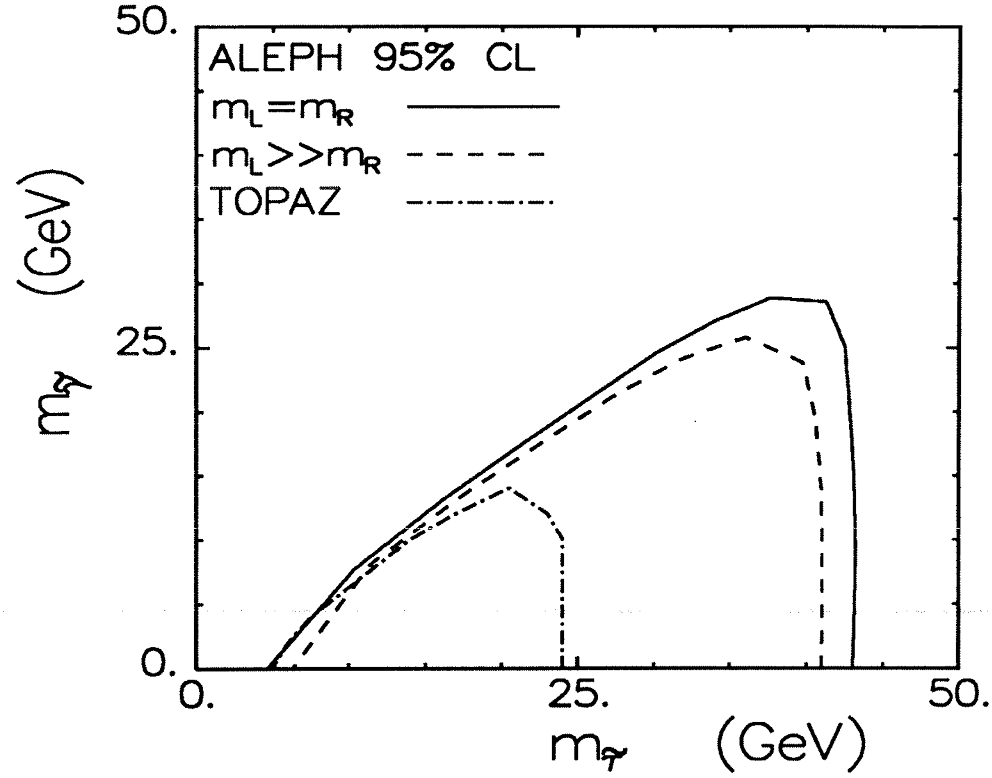

Figure 4.11: Mass limit for $\tilde{\tau}$.

mixture of $\widetilde{W}^{\pm}$ and of $\widetilde{H}^{\pm}$ in $\tilde{\chi}^{\pm}$, which can cause the cross-section to vary by about an order of magnitude. We plot the boundary for the extreme cases of pure $\widetilde{H}^{\pm}$ and pure $\widetilde{W}^{\pm}$. Any intermediate case will lie between these two extremes.

A branching ration of $\frac{1}{9}$ into each lepton flavor is assumed. This obtains if the diagrams involving squarks and sleptons are suppressed relative to the W-boson exchange diagram, which we assume when searching for the $\tilde{\chi}^{+}$.

The excluded region is shown in figure 4.12. For a light photino the limit extends to 45.0 GeV for pure $\widetilde{H}^{\pm}$ and to 45.9 for pure $\widetilde{W}^{+}$.

4.2.4 Conclusion

Three charged scalar lepton states and the chargino states are ruled out to 95% confidence level by the analysis of pairs of acoplanar charged particles described in this section. Table 4.2.4 summarizes the limits obtained for selectron, smuon, stau, and chargino, for a light photino. These limits are superior to those obtainable from a measurement of the Z^0 width alone, though marginally for the case of a pure Wino. Similar limits on these signals have been obtained by Delphi[82], Opal[84], and L3 [83].

The search for supersymmetric charged partners will begin again when the LEP accelerator increases its energy or when higher energy machines are built. Since LEP at its current energy of about 91 GeV has only begun to probe the energy scale of electroweak symmetry breaking, a supersymmetric-driven electroweak breakdown is still not excluded by this or any other analysis performed so far at LEP.

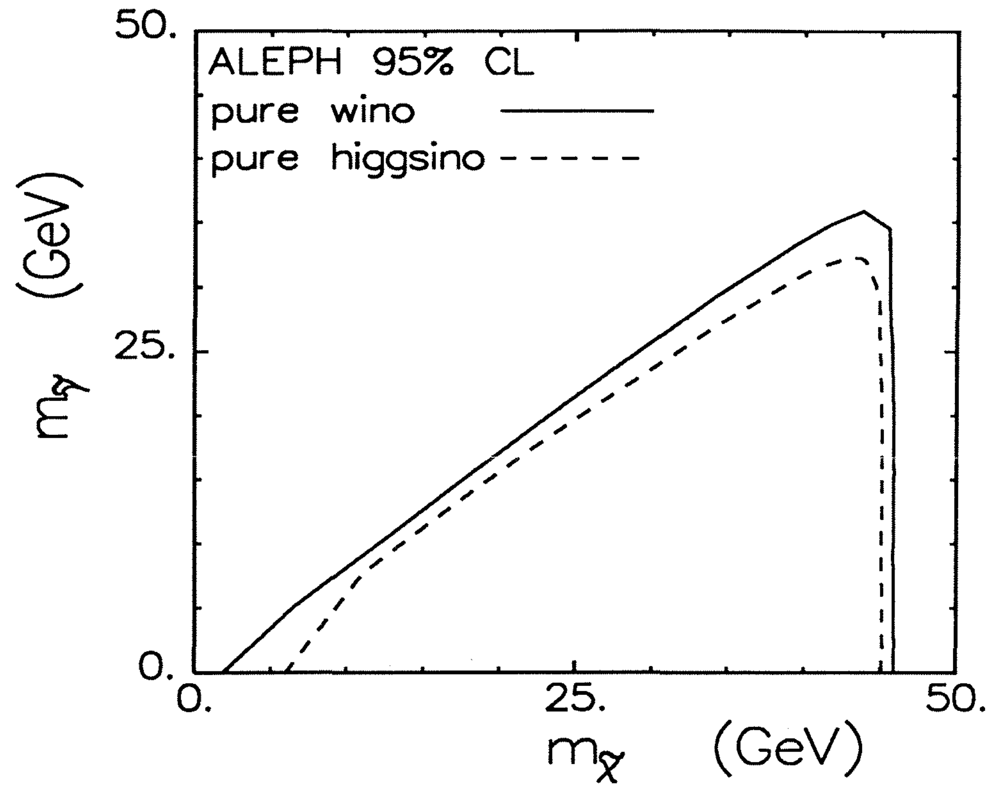

Figure 4.12: Mass limit for $\tilde{\chi}^+$.

State	95% confidence level limit, GeV
$\tilde{e}_R$	43.5
$\tilde{e}_R + \tilde{e}_L$	44.5
$\tilde{\mu}_R$	43.7
$\tilde{\mu}_R + \tilde{\mu}_L$	44.6
$\tilde{\tau}_R$	41.0
$\tilde{\tau}_R + \tilde{\tau}_L$	43.2
$\widetilde{W}^{\pm}$	45.9
$\widetilde{H}^{\pm}$	45.0

Table 4.7: Summary of limits on charged non-strongly interacting Supersymmetric particles at ALEPH

Appendix A

Poisson Confidence Level Limits

The *confidence level* may be defined as the likelihood that the (unknown) mean expected value μ_s of signal is less than l, based on an experiment in which N events are observed and μ_b background events are expected. Throughout we assume that μ_b is precisely known. The *95% confidence level limit* is that value of l for which the confidence level equals 95%. Below we shall derive the following expression for the confidence level CL:

$$CL(l) \quad = \quad 1 - \frac{e^{-(l+\mu_b)}\sum_{i=0}^{N}\frac{(l+\mu_b)^i}{i!}}{e^{-(\mu_b)}\sum_{i=0}^{N}\frac{(\mu_b)^i}{i!}}$$

For example, this would mean that if only three events were observed and 2 background events were expected, then one is 95% confident that the true value of the mean expected signal is less than 7.75 events.

The derivation of equation (1) proceeds as follows. First start with the Poisson probability $P(\mu_s)$ of observing N events in total when the expected number of total events is $\mu_s + \mu_b$,

$$P(N; \mu_b + \mu_s) = e^{-(\mu_s+\mu_b)}\frac{(\mu_s + \mu_b)^N}{N!}$$

Next, we consider this expression as an equation in μ_s for the likelihood of the *a posteriori* result. As μ_s varies, the likelihood that the above function fits the observed number of signal and background events increases or decreases. However, this function is not normalized to unity when integrated over the full range of μ_s, that is, $0 \leq \mu_s \leq \infty$. The following function is properly normalized:

$$\mathcal{L}(\mu_s) = \frac{e^{-(\mu_s+\mu_b)}\frac{(\mu_s+\mu_b)^N}{N!}}{\int_0^\infty e^{-(\mu_s+\mu_b)}\frac{(\mu_s+\mu_b)^N}{N!}d\mu_s}$$

Using this, we calculate the likelihood that the expectation μ_s is less than the limit value l, by integrating this likelihood function from $\mu_s = 0$ to $\mu_s = l$:

$$CL(l) = \frac{\int_0^l e^{-(\mu_s+\mu_b)}\frac{(\mu_s+\mu_b)^N}{N!}d\mu_s}{\int_0^\infty e^{-(\mu_s+\mu_b)}\frac{(\mu_s+\mu_b)^N}{N!}d\mu_s} \tag{A.1}$$

The indefinite integral $\int_0^l e^{-(\mu_s+\mu_b)}\frac{(\mu_s+\mu_b)^N}{N!}d\mu_s$ can be evaluated by doing N integrations by parts:

$$\begin{aligned}
&\int_0^l e^{-(\mu_s+\mu_b)}\frac{(\mu_s+\mu_b)^N}{N!}d\mu_s \\
=\;& \int_0^l -\frac{d}{d\mu_s}\left[e^{-(\mu_s+\mu_b)}\right](\mu_s+\mu_b)^N d\mu_s \\
=\;& \int_0^l e^{-(\mu_s+\mu_b)}\frac{d}{d\mu_s}(\mu_s+\mu_b)^N d\mu_s \; - \; e^{-(\mu_s+\mu_b)}(\mu_s+\mu_b)^N \,|_0^l \\
=\;& N\int_0^l e^{-(\mu_s+\mu_b)}(\mu_s+\mu_b)^{N-1}d\mu_s \; - \; e^{-(\mu_s+\mu_b)}(\mu_s+\mu_b)^N \,|_0^l \\
=\;& N(N-1)\int_0^l -\frac{d}{d\mu_s}e^{-(\mu_s+\mu_b)}(\mu_s+\mu_b)^{N-2}d\mu_s \\
&- Ne^{-(\mu_s+\mu_b)}(\mu_s+\mu_b)^{N-1}\,|_0^l \; - e^{-(\mu_s+\mu_b)}(\mu_s+\mu_b)^N \,|_0^l \\
=\;& N!\int_0^l e^{-(\mu_s+\mu_b)}d\mu_s \; - \; N!\Sigma_{i=1}^N\frac{(\mu_s+\mu_b)^i}{i!}\,|_0^l \\
=\;& -N!(e^{-(\mu_s+\mu_b)} \; + \; \Sigma_{i=1}^N\frac{(\mu_s+\mu_b)^i}{i!})\,|_0^l \\
=\;& -N!\Sigma_{i=0}^N\frac{(\mu_s+\mu_b)^i}{i!}\,|_0^l
\end{aligned}$$

Then equation (1) comes from the direct substitution of this result into equation (2), where in the denominator we take the limit as $l \to \infty$.

The terms in equation (1) are easily identified as the coming from the Poisson distributions with mean values of μ_b and $\mu_b + l$, and leads us to seek another explanation of this formula's significance. After the single measurement of signal plus background that has been performed, we know nothing about the background except that it does not exceed the measured total number of events N. Therefore we ask the following question: suppose that we ran an ensemble of experiments in which number of signal events was Poisson-distributed with a mean of l and the background Poisson distributed with a mean of μ_b. Consider the subset of experiments in which the actual number of background events is less than N. What is the probability that an experiment belonging to this subset observes a total number of events greater than N?

Let us consider the set $\mathcal{A}$ of those experiments with $n_b + n_s > N$ and $n_b \leq N$. This set is exactly the difference between the set $\mathcal{B}$ of experiments with $n_b \leq N$ and the set $\mathcal{C}$ of experiments with $n_b + n_s \leq N$. We can count the expected number of experiments in set $\mathcal{A}$ by subtracting the expected number of experiments in set $\mathcal{B}$ from the expected number in set $\mathcal{C}$, whose numbers are more readily calculated. If M is the total number of experiments, then on average

$$\begin{aligned} N(n_b \leq N) &= Me^{-(\mu_b)}\Sigma_{i=0}^{N}\frac{(\mu_b)^i}{i!} \\ N(n_b + n_s \leq N) &= Me^{-(l+\mu_b)}\Sigma_{i=0}^{N}\frac{(l+\mu_b)^i}{i!} \end{aligned} \tag{A.2}$$

So,

$$\frac{N(n_b \leq N \; and \; n_b + n_s > N)}{N(n_b \leq N)} = \frac{N(n_b \leq N) - N(n_b + n_s \leq N)}{N(n_b \leq N)} \tag{A.3}$$

and substitution of equations (3) into (4) gives again equation (1).

It is important to realize that the confidence level limit says nothing about any future repeat of the experiment which was actually performed. Rather, it makes a statement about large numbers of identically performed hypothetical experiments in which the Poisson mean of the signal is l. It predicts the rate of occurrence of certain outcomes, as in equation (4). If furthermore the Poisson mean μ_s of some experiments were above l, then this rate for these experiments would be lower, and if it were below l, then the rate would be higher.

Next we are interested in the problem of inverting equation (1) for the limit l when the confidence level $CL(l)$ is known, say 90%. This we do numerically, by adjusting l until the confidence level CL is equal to 90%. The result is shown in figure A.1, for different numbers of observed events at different levels of expected background.

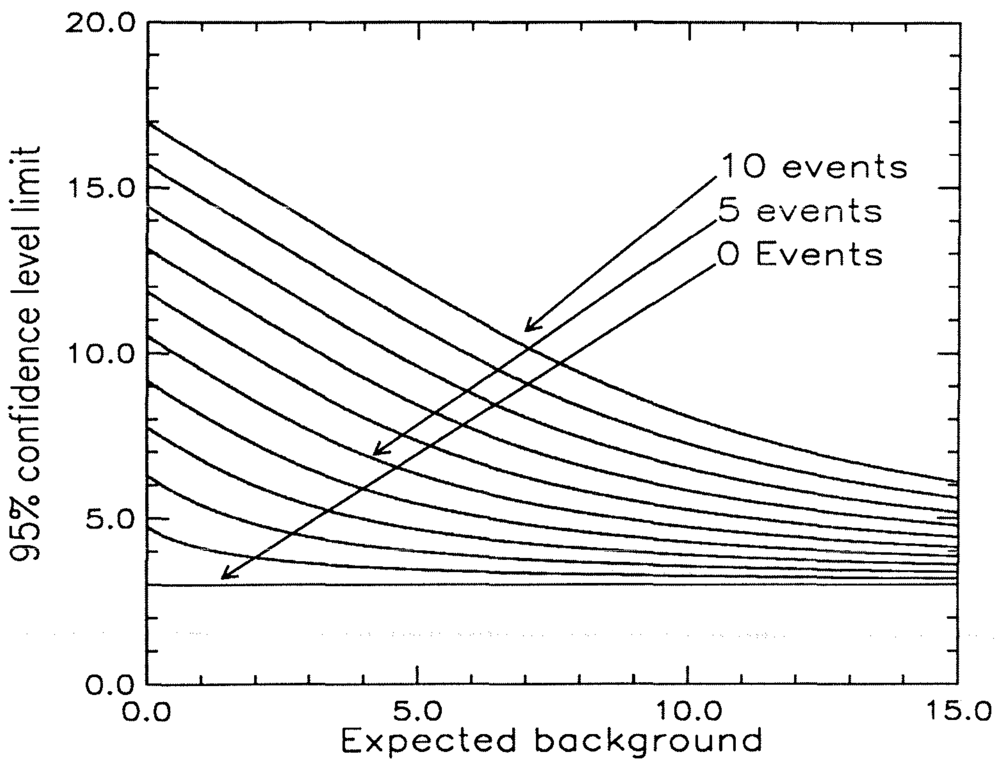

Figure A.1: 95% confidence level upper limit on signal vs. expected mean background. Each curve is for a different number of observed events

Appendix B

Features of the Lepton Energy Spectrum in the Decays of Heavy Particles

Supersymmetric charged particles, though excluded by this study up to the LEP1 beam energy, may one day be detected at higher masses in e^+e^- accelerators. LEP II for example will present an opportunity for discovering them if they exist. During the period prior to LEP running, a number of techniques were developed to study a potential signal. These techniques are gathered in this appendix in the event that they may be useful or relevant at higher centre-of-mass energies.

In the next section, we shall discuss the two-body decay of pair-produced charged scalars into a single charged lepton and a single neutral particle. We shall derive a procedure for obtaining the mass of both particles from the energy spectrum of the charged lepton. Such processes may be, for example,

$$e^+e^- \rightarrow \tilde{e}^+\tilde{e}^- \rightarrow e^+\tilde{\gamma}e^-\tilde{\gamma}$$

In the following section, we will discuss how the masses may be obtained in case the decay is a three-body decay into a single massless neutrino, a charged lepton, and another possibly massive neutral particle. Examples of such processes are, for example,

$$e^+e^- \to \tilde{\chi}^+\tilde{\chi}^- \to l^+\tilde{\gamma}\nu l^-\tilde{\gamma}\nu$$

We will derive an approximate analytic expression for the energy spectrum of the visible charged particle and which exhibits an explicit dependence on the masses of the charged and neutral daughters.

B.1 Features of the Energy Spectrum of Decay Products from the Two-body Decay of a Scalar

For scalar charged particles produced with the beam energy, the decay products are emitted isotropically in the frame of the charged scalar, according to the Wigner-Eckhardt theorem[102]. If the charged scalar decays into two daughter particles (one charged, on neutral), then the spectrum is flat and uniform between two energies which we derive next.

For concreteness we will consider the process

$$e^+e^- \to \tilde{e}^+\tilde{e}^- \to e^+\tilde{\gamma}e^-\tilde{\gamma}.$$

Let the mass of the selectron be M and the mass of the photino be m.

Consider the decay as observed from the frame of reference of the selectron. There, the energy of the daughter electron (taken massless) can be easily derived and is:

$$E' = \frac{M^2 - m^2}{2M} \tag{B.1}$$

Now, let θ represent the angle between the selectron's direction and the lepton direction in selectron rest frame, γ and β represent the boost parameters of the selectron in the lab frame. Take the x-axis as the selectron's direction, and take the selectron momentum to lie in the $x-y$ plane, as in figure B.1. The four-momentum of the electron in the selectron's rest frame is:

$$\begin{aligned}
p^{0\prime} &= E' \\
p^{1\prime} &= E' \cos\theta \\
p^{2\prime} &= E' \sin\theta \\
p^{3\prime} &= 0
\end{aligned}$$

Then the laboratory energy of the lepton is obtained by performing an inverse Lorentz transformation on this four-vector; the result is that:

$$E = \gamma E' + \beta\gamma \cos\theta E' \tag{B.2}$$

Since the decay occurs uniformly in $\cos\theta$, the laboratory energy is uniformly distributed between two extreme values given by:

$$E_{2,1} = \gamma E' \pm \beta\gamma E' \tag{B.3}$$

Finally, we can use the fact that $\gamma = E_{cms}/2M$ together with equation B.1 to derive the upper and lower cutoff energies in terms of the selectron mass and the photino mass:

$$E_{2,1} = E_{cms} \left\{ \frac{1-(\eta/\mu)^2}{4} \pm \frac{1-(\eta/\mu)^2}{4} \sqrt{1-(2\mu)^2} \right\} \tag{B.4}$$

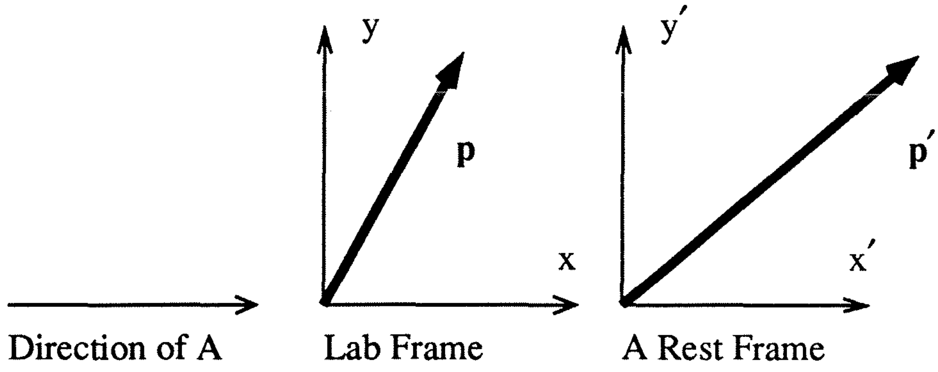

Figure B.1: This diagram shows the decay of a heavy charged particle into one or more neutral particle plus a light charged lepton (μ or e). θ represents the angle that the charged lepton makes with the direction of the heavy charged particle in that particle's center-of-mass frame.

where $\mu = \frac{M}{E_{cms}}$ and $\eta = \frac{m}{E_{cms}}$.

These equations can now be inverted to obtain the masses in terms of the upper and lower limits of the energy spectrum. The result of a straightforward calculation is:

$$\begin{aligned}
\mu &= \frac{1}{2}\sqrt{1 - \{(\xi_2 - \xi_1)/(\xi_2 + \xi_1)\}^2} \\
\eta &= \mu\sqrt{1 - 2(\xi_2 + \xi_1)}
\end{aligned} \qquad (B.5)$$

where $\xi_{1,2} = E_{1,2}/E_{cms}$.

In case of an observed signal, one would have to consider several systematic effects that shift the edges from the values calculated here. Among them are QED radiative corrections, the effect of cuts, and detector smearing. Nonetheless, the resolution of the method is quite good. For example in ALEPH, we would expect a resolution of would have been less than 0.5 GeV for the selectron, and less than about 2.5 GeV for the photino after accumulating only about 10 pb^{-1} of data. This is true for a wide range of selectron and photino masses.

B.2 General Features of the Energy Spectrum of Decay Products in Three-body Decay

Before describing our method, let us start with a example to help motivate the discussion our unusual approximation. We will begin by comparing two cases of three body decay whose matrix elements are quite different:

- Heavy fermion pair production at the peak of the Z^0 it in a maximally polarized state, that is $g_v = g_a$. This can be arranged for normal fermions if $\sin^2\theta_W = 1/2$. The decay proceeds through the normal virtual-W emmision.

- The second case is identical in production, but in the decay the couplings of the virtual-W have been altered so that it couples equally to left and right handed particles.

To generate the signals we use the generator TIPTOP [103].

Why are these cases so different? In a language familiar from the study of τ polarization, the "analyzing power" of the decay comes from its parity violation. If parity is violated then there may be preferential emmision of decay products along the axis of the spin. For right or left polarized particles the decay products will be preferentially boosted forwards along the particles motion, or backwards, leading to a harder, or softer, spectrum of the observed particles. If the fermions are maximally polarized, as in case 1, then the effect is maximal. However in case 2, the parity violation in the decay has been turned off, so the effect is washed out.

The energy spectra of the daughter leptons from the two cases are shown in figure B.2. Though there are important differences in the two distributions, the general shape, peak position, and endpoint are quite similar. This suggests that the dominant features of the distribution are controlled by the *kinematic* factors to first order, and dynamics to a lesser degree. We will here attempt to describe

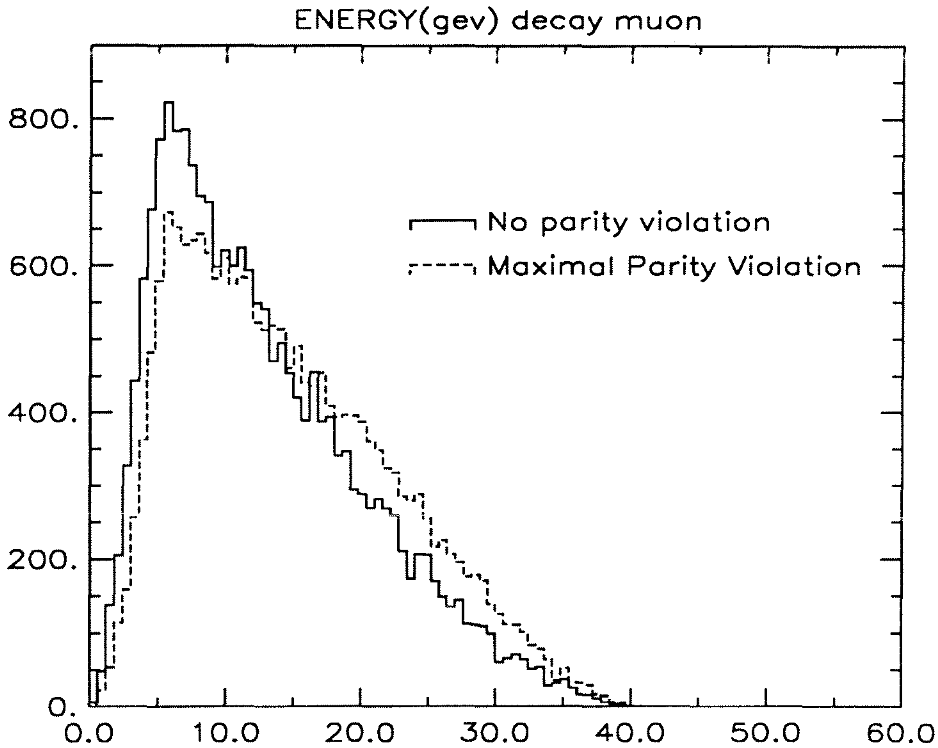

Figure B.2: Lepton energy spectrum for highly polarized fermion-pair production. The solid line represents the distribution when parity violation in the decay has been turned off.

these distributions by simple formula in the approximation that the dynamics of the decay, i.e., the matrix elements, are ignored completely.

The derivation proceeds as follows. Consider the process

$$A^- \to B^0 + l^- + \bar{\nu}_l \tag{B.6}$$

in the following we will take the masses of all particles to be zero except for A and B. Two examples of such processes are:

$$A = \tilde{\chi}^{+} \quad , \quad B = \tilde{\gamma}$$

$$A = L_{+} \quad , \quad B = \nu_L$$

where L is a fourth-generation heavy lepton. Whatever is the identity of particle A, we will assume that it is produced monoenergetically with boost parameters γ and β, as in pair production from an e^+e^- initial state.

Before any approximations are made, the differential partial width for any configuration of the momenta p_B^μ, p_l^μ, p_ν^μ is

$$d\Gamma = \frac{1}{2E_A}(2\pi)^4 \left|\mathcal{M}\right|^2 \cdot \delta^4(p_A^\mu - p_B^\mu - p_l^\mu - p_\nu^\mu) d\text{Lips}_B d\text{Lips}_l d\text{Lips}_\nu \qquad \text{(B.7)}$$

where $d\text{Lips} = d^3p/(2\pi)^3 2E$ is the Lorentz invariant phase space element [104].

At this point we approximate by ignoring the dynamics of the decay, or equivalently making the matrix element a constant factor instead of a function of the four momenta and spins. When this approximation is made we can take some of the results of [69]. First we shall introduce some variables which follow closely the treatment given in [69]. Let

$$\begin{aligned} \mu &= M_B^2/M_A^2 \\ x_B' &= 2E_B'/M_A \\ x_l' &= 2E_l'/M_A \end{aligned}$$

where the primes denote that all energies are taken, at this stage, in the center-of-mass frame of the moving particle A. In reference [69] it is proven that the phase space is restricted, in the variables x'_l and x'_B, to the kinematic region:

$$\begin{aligned} \frac{x'^2_l + 1 - 2x'_l + \mu}{1 - x'_l} \geq & \; x'_B & \leq 1 + \mu \\ 0 \geq & \; x'_l & \leq 1 - \mu \end{aligned}$$

and that

$$\frac{d\Gamma}{dx'_l dx'_B} = \frac{M_A}{256\pi^2} |\mathcal{M}|^2 \tag{B.8}$$

The distribution in the variables x'_l and x'_B is shown in figure B.3. To find the energy of the lepton in the center-of-mass frame we must project this distribution onto the x'_l axis which is accomplished by integrating over the unobserved energy x'_B.

$$\begin{aligned} \frac{d\Gamma}{dx'_l} &= \int_{\frac{x'^2_l+1-2x'_l+\mu}{1-x'_l}}^{1+\mu} \frac{d\Gamma}{dx'_l dx'_B} dx'_B \\ &= \frac{M_A}{256\pi^2} |\mathcal{M}|^2 \int_{\frac{x'^2_l+1-2x'_l+\mu}{1-x'_l}}^{1+\mu} dx'_B \\ &= \frac{M_A}{256\pi^2} |\mathcal{M}|^2 \left\{ 1 + \mu - \frac{x'^2_l + 1 - 2x'_l + \mu}{1 - x'_l} \right\} \\ &= \frac{M_A}{256\pi^2} |\mathcal{M}|^2 \frac{x'_l}{1 - x'_l} (1 - x'_l - \mu) \end{aligned} \tag{B.9}$$

The angular distribution of leptons from the decay of A is isotropic in our approximation, so we may write

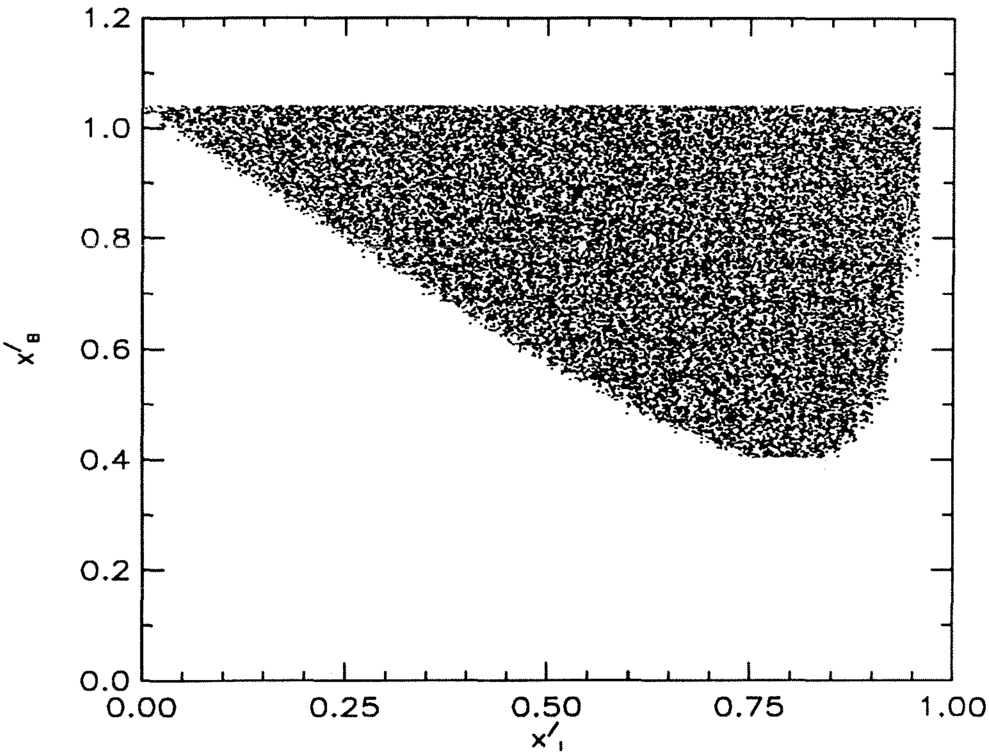

Figure B.3: Distribution of daughter lepton energy vs. energy of the neutral massive particle B, in the center-of-mass frame of particle A. The shape of the distribution is determined by the particle masses.

$$\frac{d\Gamma}{dx_l' dy} = \frac{M_A}{512\pi^2} |\mathcal{M}|^2 \frac{x_l'}{1 - x_l'} (1 - x_l' - \mu) \tag{B.10}$$

where $y = \cos\theta$ and θ is the angle at which l is emmited relative to the direction of particle A, in the lab frame of particle A, as in diagram B.1.

Now we would like to transform this distribution to the laboratory frame. This is best done by re-expressing equation B.10 in terms of the $x_l = 2E_l/M_A$ (E_l being the energy of the lepton in the laboratory frame), and $z = \beta\gamma\cos\theta$. These variables are related to the rest-frame variables via:

$$\begin{aligned} x_l &= x_l'(\gamma + \beta\gamma y) \\ z &= \beta\gamma y \end{aligned} \tag{B.11}$$

Then equation B.10 may be transformed to:

$$\frac{d\Gamma}{dx_l dz} = \frac{d\Gamma}{dx_l' dy} \frac{1}{|J|} \tag{B.12}$$

where J is the Jacobian of the transformation,

$$\begin{aligned} J &= \det \begin{vmatrix} \frac{\partial x_l}{\partial x_l'} & \frac{\partial x_l}{\partial y} \\ \frac{\partial z}{\partial x_l'} & \frac{\partial z}{\partial y} \end{vmatrix} \\ &= \det \begin{vmatrix} \beta\gamma(\gamma + z) & \frac{\beta\gamma x_l}{\gamma + z} \\ 0 & \beta\gamma \end{vmatrix} \\ &= \beta^2\gamma^2(\gamma + z) \end{aligned} \tag{B.13}$$

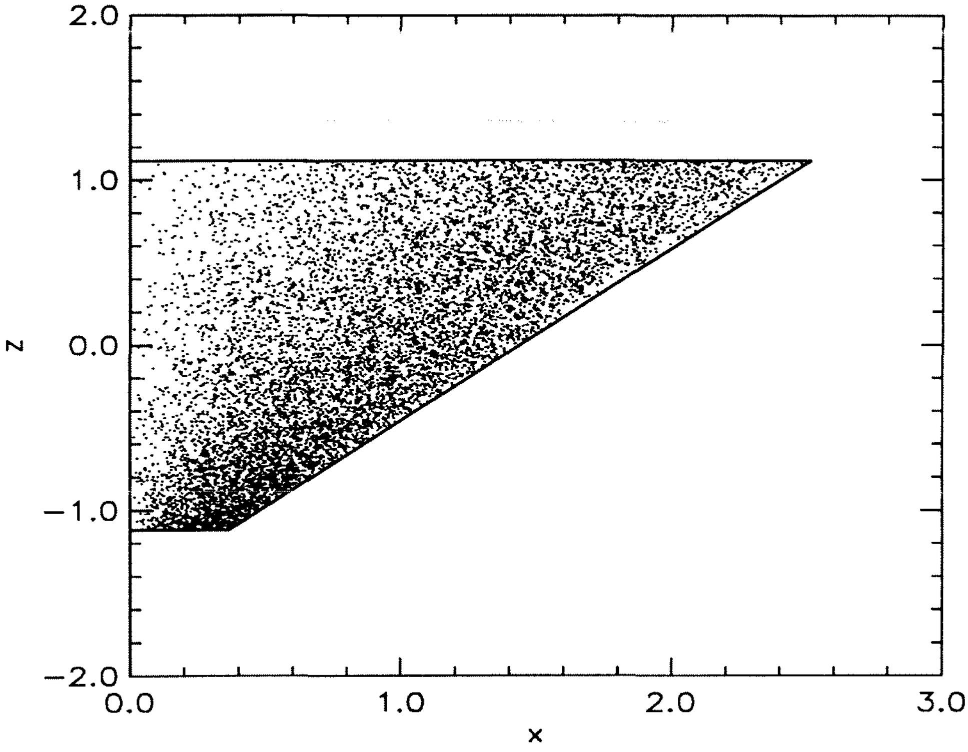

Figure B.4: Probability distribution in the variables x, and z. The variable z is not observed and we integrate over z to obtain the final result

With equations B.10,B.11,B.12 and B.13 we have:

$$\begin{aligned}\frac{d\Gamma}{dx_l dz} &= \frac{M_A}{512\pi^2\beta^2\gamma^2}|\mathcal{M}|^2\frac{1}{(\gamma+z)}\frac{\frac{x_l}{\gamma+z}}{1-\frac{x_l}{\gamma+z}}(1-\frac{x_l}{\gamma+z}-\mu)\\ &= \frac{M_A}{512\pi^2\beta^2\gamma^2}|\mathcal{M}|^2\frac{1}{(\gamma+z)}\frac{x_l}{\gamma+z-x_l}\left[1-\frac{x_l}{\gamma+z}-\mu\right]\end{aligned} \tag{B.14}$$

The probability distribution and the kinematic limits in the variables x and z are shown in figure B.4.

The variable z is not directly observed, and so we must integrate over this variable to obtain the energy distribution of the decay lepton in the laboratory frame:

$$\begin{aligned}
\frac{d\Gamma}{dx_l} &= \frac{M_A}{512\pi^2\beta^2\gamma^2}|\mathcal{M}|^2 \cdot \int_R dz \frac{1}{(\gamma+z)} \frac{x_l}{\gamma+z-x_l}\left[1-\frac{x_l}{\gamma+z}-\mu\right] \\
&= \frac{M_A}{512\pi^2\beta^2\gamma^2}|\mathcal{M}|^2 \cdot \int_R dz \left[\frac{x_l}{(\gamma+z)^2} - \frac{\mu x_l}{(\gamma+z)(\gamma+z-x_l)}\right] \\
&= \frac{M_A}{512\pi^2\beta^2\gamma^2}|\mathcal{M}|^2 \cdot \left\{\frac{-x_l}{\gamma+z} - \mu \ln\left|\frac{z+\gamma-x_l}{z+\gamma}\right|\right\}_R
\end{aligned}$$

where R is the region of integration.

We can break R into two smaller regions of integration,

$$\text{Region I}: \qquad 0 \le x_l \le \gamma(1-\beta)(1-\mu) \tag{B.15}$$

$$\text{Region II}: \quad \gamma(1-\beta)(1-\mu) \le x_l \le \gamma(1-\beta)(1+\mu) \tag{B.16}$$

which are bounded by the functions

$$\text{Region I}: \quad -\beta\gamma \le z \le \beta\gamma \tag{B.17}$$

$$\text{Region II}: \quad \tfrac{x_l}{1-\mu} - \gamma \le z \le \beta\gamma \tag{B.18}$$

This gives us for the two regions:

$$\begin{aligned}
\text{Region I}: \ \tfrac{d\Gamma}{dx_l} &= \frac{M_A}{512\pi^2\beta^2\gamma^2}|\mathcal{M}|^2 \cdot \left\{-\frac{x_l}{\gamma+z} - \mu \ln\left|\frac{z+\gamma-x_l}{z+\gamma}\right|\right\}_{-\beta\gamma}^{\beta\gamma} \\
&= \frac{M_A}{512\pi^2\beta^2\gamma^2}|\mathcal{M}|^2 \cdot \left\{2\beta\gamma x_l + \mu \ln\left[\frac{\gamma - \frac{x_l}{1-\beta}}{\gamma - \frac{x_l}{1+\beta}}\right]\right\} \qquad \text{(B.19)} \\
\text{Region II}: \ \tfrac{d\Gamma}{dx_l} &= \frac{M_A}{512\pi^2\beta^2\gamma^2}|\mathcal{M}|^2 \cdot \left\{-\frac{x_l}{\gamma+z} - \mu \ln\left|\frac{z+\gamma-x_l}{z+\gamma}\right|\right\}_{\frac{x_l}{1-\mu}}^{\beta\gamma}
\end{aligned}$$

$$
\begin{aligned}
&= \quad \frac{M_A}{512\pi^2\beta^2\gamma^2}\left|\mathcal{M}\right|^2 \cdot \left\{1-\mu-\frac{x_l}{\gamma(1+\beta)}\right. \\
&+ \quad \left.\mu\ln\left[\frac{\mu\gamma(1+\beta)}{\gamma(1+\beta)-x_l}\right]\right\} \qquad \text{(B.20)} \\
& \qquad \text{(B.21)}
\end{aligned}
$$

Letting

$$
\xi = \frac{x_l}{\gamma} = \frac{2E_l}{M_A\gamma} = \frac{2E_l}{E_{beam}} \qquad \text{(B.22)}
$$

we can re-express equations B.19 and B.20 in a simple form:

$$
\begin{aligned}
P(\xi) \propto &\quad 2\beta\gamma^2\xi + \mu\ln\tfrac{(1+\beta)(1-\beta-\xi)}{(1-\beta)(1+\beta-\xi)} \quad 0 \leq \xi \leq (1-\beta)(1-\mu) \\
P(\xi) \propto &\quad -\tfrac{\xi}{1+\beta} + 1 - \mu + \mu\ln\tfrac{\mu(1+\beta)}{(1+\beta-\xi)} \quad (1-\beta)(1-\mu) \leq \xi \leq (1+\beta)(1-\mu)
\end{aligned}
\qquad \text{(B.23)}
$$

Equation B.23 gives the unnormalized probability distribution that the the lepton from the process B.6 is observed with an energy ξ (normalized to half the energy of particle A). In e^+e^- accelerators the energy of particle A is just the beam energy. This compact formula is a function of only two parameters which can be taken as the mass of A and the mass of B. Now we must ask how well the formula fits various spectra where the effects the matrix elements, initial state radiation, and other important effects included.

We begin by comparing the energy spectrum for maximally polarized fermions with maximal parity violation, from the TIPTOP Monte Carlo, with the analytic expression B.23. This is shown in figure B.5. The approximation B.23 good enough to be considered useful for many purposes.

On the other hand, we can fit the distribution B.23 to the energy spectrum, thereby extracting the particle masses M_A and M_B. In a likelihood fit with Minuit, we obtain

$$\begin{aligned} M_A &= 37.4 \text{ GeV} \\ M_B &= 15.3 \text{ GeV} \end{aligned}$$

as opposed to the input values of 35.0 and 15.0 GeV. This is of course without detector smearing, pollution from other physics sources, and the spectral distortion due to cuts.

The same comparison is now made for polarized fermions with the parity violation turned off in the decay. The Monte Carlo is displayed along with the approximate analytic formula. In a fit to the spectrum, we obtain

$$\begin{aligned} M_A &= 33.4 \text{ GeV} \\ M_B &= 15.7 \text{ GeV} \end{aligned}$$

where again the input values were 35.0 and 15.0 GeV.

In conclusion, it seems reasonable that the approximate analytic formula B.23 could be useful in determining the mass of an unknown particle into a lepton, its neutrino, and an additional heavy neutral particle, even if little was known about the precise dynamics of the particle's production or decay.

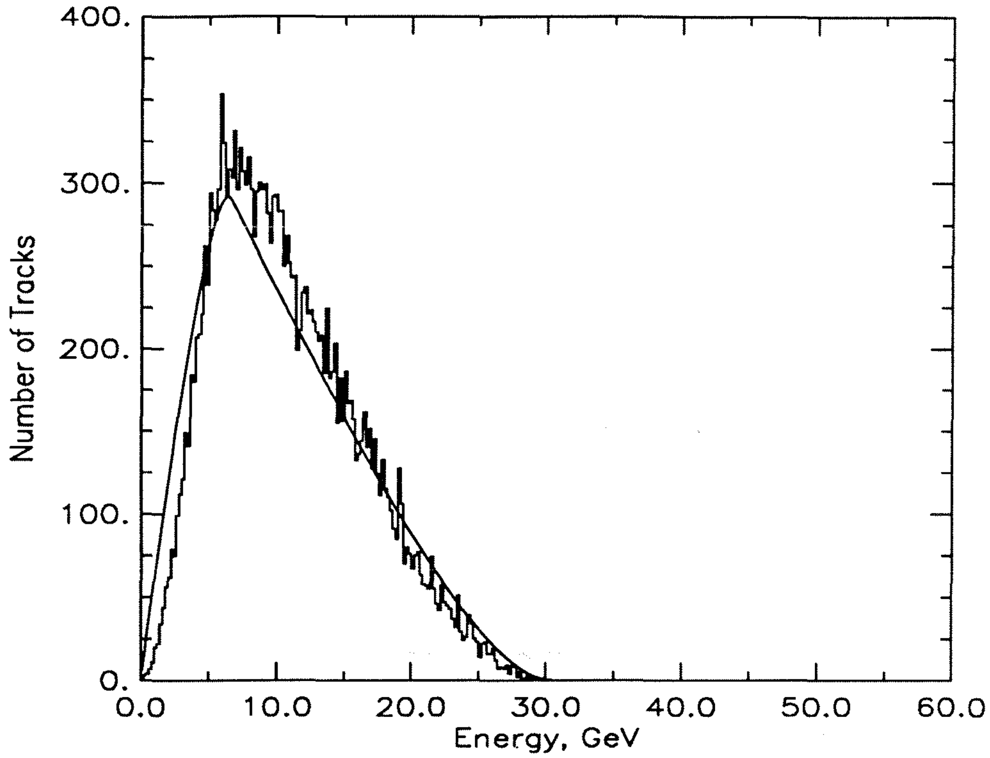

Figure B.5: Energy spectrum with maximum parity violation in the decay. The smooth line once again represents the approximate function derived in this appendix

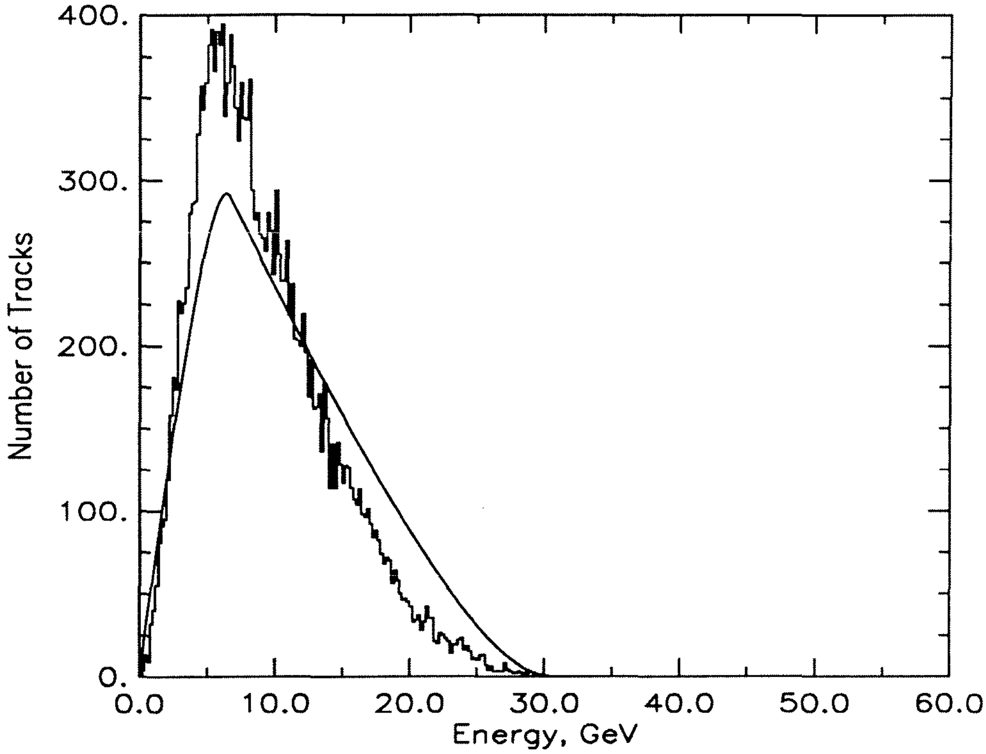

Figure B.6: Energy spectrum with parity violation in the decay turned off. The smooth line is the approximate function derived in this appendix

Bibliography

[1] A. Salam. *Elementary Particle Theory*, chapter Weak and Electromagnetic Interactions. Almquist and Wiksell, Stockholm, 1968.

[2] S. Weinberg. A model of leptons. *Physical Review Letters*, 19(21), 1967.

[3] S. Glashow. Partial-symmetries of weak interactions. *Nuclear Physics*, 8B(22), 1961.

[4] G.S. Abrams et all. Initial measurements of Z boson resonance parameters in e^+e^- annihilation. *Phys. Rev. Letters*, 63(7):724–727, 1989.

[5] G.S. Abrams et all. Measurement of Z boson resonance parameters in e^+e^- annihilation. *Phys. Rev. Letters*, 63(20):2173–2176, 1989.

[6] G.S. Abrams et all. Measurement of Z decays into lepton pairs. *Phys. Rev. Letters*, 63(26):2780–2783, 1989.

[7] G.S. Abrams et all. Measurement of the $B\bar{B}$ fraction in hadronic Z decays. *Phys. Rev. Letters*, 63(19):1211–1214, 1990.

[8] The L3 Collaboration. A determination of the properties of the neutral intermediate vector boson Z^0. *Physics Letters B*, 231(4):509–518, November 1989.

[9] The L3 collaboration. Measurement of g_A and g_V, the neutral current coupling constants to leptons. *Physics Letters B*, 236(1):109–115, February 1190.

[10] The L3 Collaboration. *A measurement of the Z^0 leptonic partial width and the vector and axial vector coupling constants.* CERN L3 Preprint 5, CERN, 1990.

[11] The L3 Collaboration. *A measurement of Electroweak Parameters from $Z^0 \rightarrow \mu^+\mu^-(\gamma)$.* CERN L3 Preprint 8, CERN, 1990.

[12] The OPAL Collaboration. Measurement of the Z^0 mass and width with the OPAL detector at LEP. *Physics Letters B*, 231(4):530–538, November 1989.

[13] The OPAL Collaboration. Measurement of the decay of the Z^0 into lepton pairs. *Physics Letters B*, 235(3,4):379–388, 1989.

[14] The OPAL Collaboration. *Analysis of Z^0 couplings to charged leptons.* CERN EP Preprint 90-81, CERN, 1990.

[15] The OPAL Collaboration. *A combined analysis of the hadronic and leptonic decays of the Z^0.* CERN EP Preprint 90-27, CERN, 1990.

[16] The ALEPH Collaboration. Determination of the number of light neutrino species. *Physics Letters B*, 231(4):519–529, November 1989.

[17] The ALEPH Collaboration. A precise determination of the number of families with light neutrinos and of the Z boson partial widths. *Physics Letters B*, 235(3):399–411, February 1989.

[18] The ALEPH Collaboration. Determination of the leptonic branching ratios of the Z. *Physics Letters B*, 234(3):399–408, January 1990.

[19] The ALEPH Collaboration. *Heavy flavour production in Z decays*. CERN EP Preprint 90-54, CERN, 1990.

[20] The DELPHI Collaboration. *A precise measurement of the Z resonance parameters through its hadronic decays*. CERN EP Preprint 90-32, CERN, 1990.

[21] The DELPHI Collaboration. *Study of the leptonic decays of the Z^0 boson.* CERN EP Preprint 90-31, CERN, 1990.

[22] The UA1 Collaboration. Search for top quark production at the CERN proton-antiproton collider. *Zeitshrift fuer Physik C*, 37, 1990.

[23] The CDF Collaboration. Search for the top quark in the reaction $\bar{p}p \rightarrow$ electron + jets at $\sqrt{s} = 1.8$ TeV. *Phys. Rev. Letters*, 64(2), 1990.

[24] The UA2 Collaboration. Search for top quark production at the CERN $\bar{p}p$ collider. *Zeitshrift fuer Physik C*, 46, 1990.

[25] The ALEPH Collaboration. A search for new quarks and leptons from Z^0 decay. *Physics Letters B*, 236, 1990.

[26] The OPAL Collaboration. A search for the top and b' quarks in hadronic Z^0 decays. *Physics Letters B*, 236, 1990.

[27] The DELPHI Collaboration. *Search for the t and b' quarks in hadronic decays of the Z^0 boson.* CERN EP Preprint, CERN, 1990.

[28] The ALEPH Collaboration. *Search for the neutral Higgs boson from Z^0 decay in the Higgs mass range between 11 and 24 GeV.* CERN EP Preprint 90-16, CERN, 1990.

[29] The L3 Collaboration. *Search for neutral Higgs boson in Z^0 decay.* CERN L3 Preprint 010, CERN, 1990.

[30] The OPAL Collaboration. Mass limits for a Standard Model Higgs boson in e+e- collisions at LEP. *Physics Letters B*, 236, 1990.

[31] M. Bander. Theories of quark confinement. *Physics Reports*, 75(4), 1981.

[32] F. E. Close. *An Introduction to Quarks and Partons.* Academic Press, 1979.

[33] C. N. Yang and R. L. Mills. Conservation of isotopic spin and local gauge invariance. *Phys. Rev.*, 96(1), 1954.

[34] R. Utiyama. Invariant theoretical interpretation of interactions. *Phys. Rev.*, 101(5), 1956.

[35] D. J. Gross and F. Wilzcek. Ultraviolet behaviour of non-Abelian gauge theories. *Phys. Rev. Letters*, 30(26), 1973.

[36] D. J. Gross and F. Wilzcek. Assymptotically free gauge theories I. *Phys. Rev.*, D8(10), 1973.

[37] H. D. Politzer. Assymptotic freedom: an approach to strong interactions. *Physics reports*, 14(4), 1974.

[38] S. L. Wu. e^+e^- physics at PETRA: the first five years. *Physics Reports*, 107(2-5), 1984.

[39] P. Langacker. Grand unified theories and proton decay. *Physics Reports*, 72(4), 1981.

[40] H. E. Haber and G. L. Kane. The search for supersymmetry: probing physics beyond the standard model. *Physics Reports*, 117(2-4), 1984.

[41] L. Susskind. Dynamics of spontaneous symmetry breaking in the Weinberg-Salam theory. *Physical Review D*, 20(10), 1979.

[42] S. Dimopoulos and H. Georgi. Softly broken supersymmetry and SU(5). *Nuclear Physics*, B193, 1981.

[43] G. t'Hooft. Naturalness, chiral symmetry, and spontaneous chiral symmetry breaking. In *Recent Developements in Gauge Theory*, NATO Advanced Summer Institute, Cargese, 1979, Plenum, New York, 1980.

[44] E. Gildner. Gauge-symmetry hierarchies. *Physical Review D*, 14(6), 1976.

[45] Y. Kazama and Y. Yao. Decoupling, effective Lagrangian and gauge hierarchy in spontaneously broken non-Abelian gauge theories. *Physical Review D*, 25(6), 1982.

[46] C. T. Sachrajda. A "renormalization group improved" study of the gauge hierarchy problem. *Physics Letters*, 98B(4), 1981.

[47] C. H. Llewellyn Smith and G. G. Ross. The real gauge hierarchy problem. *Physics Letters*, 105B(1), 1981.

[48] G. Kane J. F. Gunion, H. E. Haber and S. Dawson. *The Higgs Hunter's Guide*. Addison-Wesley, 1990.

[49] M. E. Peskin. Compositeness of quarks and leptons. In *Proceedings of the 1981 International Symposium on Lepton and Photon Interactions at High Energies, Bonn*, 1981.

[50] E. Fahri and L. Susskind. Technicolor. *Physics Reports*, 74(3), 1981.

[51] M. Sohnius. Introducing supersymmetry. *Physics Reports*, 128(2,3), 1985.

[52] S. Coleman and J. Mandula. All possible symmetries of the S-matrix. *Phys. Rev.*, 159(5), 1967.

[53] J. T. Lopuszanski R. Haag and M. E. Sohnius. All possible generators of supersymmetries of the s-matrix. *Nuclear Physics B*, 88, 1975.

[54] J. Wess and B. Zumino. A Lagrangian model invariant under supergauge transformations. *Physics Letters B*, 49(1), 1974.

[55] J. Gunion and H. Kane. Higgs bosons in supersymmetric models. *Nuclear Physics B*, 272, 1986.

[56] J. Gunion and H. Kane. Higgs bosons in supersymmetric models(II). *Nuclear Physics B*, 278, 1986.

[57] J. Iliopoulos and B. Zumino. Broken supergauge symmetry and renormalization. *Nulear Physics B*, 76, 1974.

[58] J. Ellis. Concluding theoretical remarks. *Physics Reports*, 105(1,2), 1984.

[59] E. Witten. Dynamical breaking of supersymmetry. *Nuclear Physics B*, 188, 1981.

[60] R. K. Kaul. Gauge hierarchy in a supersymmetric model. *Physics Letters B*, 109(1,2), 1982.

[61] P. van Nieuwenhuizen. Supergravity. *Physics Reports*, 68(4), 1981.

[62] P. Fayet. Supergauge extension of the Higgs mechanism and a model for the electron and its neutrino. *Nuclear Physics B*, 90, 1975.

[63] A. Salam and J. Strathdee. Supersymmetry and fermion number conservation. *Nuclear Physics B*, 87, 1975.

[64] J. Ellis et all. Supersymmetric relics from the big bang. *Nuclear Physics B*, 238, 1984. And references therein.

[65] T. Shimert and X. Tata. Lepton distributions from the decay of scalar lepton pairs at e^+e^- colliders. *Physical Review D*, 32, 1985.

[66] Ed. John Ellis and Roberto Peccei. *Physics at LEP*. CERN Report 86-02, CERN, 1986.

[67] M. Chen et. all. Signals from non-strongly interacting supersymmetric particles at LEP energies. *Physics Reports*, 159(4-5), 1988.

[68] Ed. G. Altarelli R. Kleiss and C. Verzegnassi. *Z Physics at LEP 1*. CERN Report 89-08, CERN, 1989.

[69] Vernon D. Barger and Roger J. N. Phillips. *Collider Physics*. Addison-Wesley, 1987.

[70] J.M. Frere and G. Kane. On the possibility of finding light uncolored supersymmetric partners at present and future machines. *Nuclear Physics B*, 223, 1983.

[71] D Dicus et. all. Electron-positron annihilation cross section in $\mathbf{SU(2)_L \times U(1)}$ supergravity. *Phys. Rev. Letters*, 51(12), 1983.

[72] Y. Kizukuri and N. Oshimo. *Lepton Energy distribution for two-body decay of chargino at e^+e^- colliders*. TKU-HEP preprint 88-11, Tokyo University, 1988.

[73] T. Shimert C. Burgess and X. Tata. Lepton distributions from the decay of $\tilde{W}$ pairs at e^+e^- colliders. *Physical Review D*, 32, 1985.

[74] The TOPAZ collaboration. Search for SUSY particles in e^+e^- annihilation at TRISTAN. *Physics Letters B*, 218(1), 1989.

[75] The ASP collaboration. Search for the anomalous production of single photons in e^+e^- collisions at $\sqrt{s}$ =29 gev. *Phy. Rev. D*, 39(11), 1989.

[76] The UA2 Collaboration. Search for scalar electrons and winos at the CERN $\bar{p}p$ collider. *Physics Letters B*, 238, 1990.

[77] The UA1 Collaboration. Events with large missing transverse energy at the CERN collider: III. mass limits on supersymmetric particles. *Physics Letters B*, 198(2), 1987.

[78] The UA2 Collaboration. Search for squark and gluino production at the CERN $\bar{p}p$ collider. *Physics Letters B*, 235, 1990.

[79] The CDF Collaboration. Limits on masses of supersymmetric particles from 1.8 TeV $\bar{p}p$ collisions. *Phys. Rev. Letters*, 62(16), 1989.

[80] The OPAL collaboration. *A direct search for neutralino production at LEP*. CERN EP Preprint 90-95, CERN, 1990.

[81] The ALEPH collaboration. *Search for neutralino production in Z decays*. CERN EP Preprint 90-63, CERN, 1990.

[82] The DELPHI collaboration. *A search for sleptons and gauginos in Z^0 decays*. CERN EP Preprint 90-80, CERN, 1990.

[83] The L3 collaboration. Mass limits for scalar muons, scalar electrons, and winos from e+e- collisions near $\sqrt{s} = 91$ gev. *Physics Letters B*, 233(3,4), 1989.

[84] The OPAL Collaboration. A search for acoplanar pairs of leptons or jets in Z^0 decays : mass limits on supersymmetric particles. *Physics Letters B*, 240(1,2), 1990.

[85] The ALEPH Collaboration. Search for supersymmetric particles using acoplanar charged-particle pairs from Z^0 decays. *Physics Letters B*, 236(1):86–94, February 1990.

[86] E. Fernandez. Constraints on the standard model from experimental studies of the Z-pole. Talk delivered at the Neutrino 90 Conference at CERN.

[87] The ALEPH Collaboration. *ALEPH: A Detector for Electron-Positron Annihilations at LEP.* CERN EP Preprint 90-25, CERN, 1990.

[88] S.R Amendolia *et. all.* The spatial resolution of the ALEPH TPC. *Nuclear Instruments and Methods*, 217:573–577, 1989.

[89] Makoto Takashima. *The Electronics calibration system for the ALEPH Time Projection Chamber.* Master's thesis, University of Wisconsin,Madison, 1985.

[90] Joerg Richstein. *Measurements of Electron Drift and Diffusion Properties in a Large Cylindrical Drift Chamber (TPC) with Parallel Electric and Magnetic Fields.* PhD thesis, Universitaet Dortmund, 1986.

[91] P. Nemethy *et. all.* Gated time projection chamber. *Nuclear Instruments and Methods*, 212:273–280, 1983.

[92] A. Denner M. Bohm and W. Hollik. Radiative corrections to Bhabha scattering at high energies. *Nuclear Physics B*, 304, 1988.

[93] R. Kleiss F.A. Behrens and W. Hollik. Radiative corrections to Bhabha scattering at high energies. *Nuclear Physics B*, 304, 1988.

[94] R. Kleiss et. all. *Z Physics at LEP 1.* CERN Report 89-08, CERN, 1989.

[95] F.A. Behrens et all. Complete lowest-order calculations for four-lepton final states in electron-positron collisions. *Nuclear Physics B*, 253, 1985.

[96] R. Kleiss et all. *Z Physics at LEP 1.* CERN Report 89-08, CERN, 1989.

[97] S. Kawabata. A new Monte Carlo generator for high energy physics. *Computater Physics Communications*, 41, 1986.

[98] J. A. M. Vermassen. In *International Workshop on Gamma-Gamma Interactions*, Springer-Verlag, 1986.

[99] Gourdin Bonneau and Martin. Inelastic lepton (anti-)lepton scattering and the two photon exchange approximation. *Nuclear Physics B*, 54, 1973.

[100] The ALEPH Collaboration. Measurement of electroweak parameters from Z decays into fermion pairs. *Zeitschrift fuer Physik C*, 48:365–391, 1990.

[101] O. Helene. Upper limit of peak area. *Nuclear Instruments and Methods*, 212, 1983.

[102] E. Merzbacher. *Quantum Mechanics.* John Wiley and Sons, 1961,1970.

[103] J. H. Kuhn S. Jadach. *TIPTOP, a Monte Carlo for Heavy Fermion Production and Decay.* MPI PAE Pth 86-64, Max Plank, 1986.

[104] F. Halzen and A. Martin. *Quarks and Leptons: an introductory course in modern particle physics.* John Wiley and Sons, 1984.